Indian Geotech J (March 2018) 48(1):1–51
https://doi.org/10.1007/s40098-017-0285-z

ORIGINAL PAPER

Geomechanical Challenges: Practices and Innovations

M. N. Viladkar[1]

Received: 23 September 2017 / Accepted: 23 October 2017 / Published online: 4 December 2017

Abstract After briefly reviewing the past and the current status in geotechnical engineering, an attempt has been made here to discuss three case studies related to extreme loading conditions like impact and blast loading, extreme wind loading and severe squeezing ground condition in lower Himalaya. These were really very challenging problems and some innovative solutions were provided which were implemented in the field. Subsequently, attempt has also been made to identify some of the more challenging problems which are basically coupled, multi-physics–multi-mechanics problems. To undertake such problems, however, there is a need to widen the scope of geotechnical engineering into a wider area of geo-engineering.

Keywords Impact and blast loading · Extreme wind loading · Squeezing ground condition · Geomechanical challenges

Introduction

Since the early contributions on earth pressure theories by Coulomb in 1776 and Rankine in 1857, soil mechanics and soil engineering or in general, geo-mechanics and geotechnical engineering are the areas which have come of age during the twentieth century. When one takes a wider view of geotechnical engineering, our knowledge spreads not only over geological and geotechnical engineering but also covers the fields of rock mechanics and rock engineering, partly mining engineering, and offshore engineering. Many difficult and challenging phenomena have been understood till date. Geotechnical engineers know how to analyze, design and build high earth and rock fill dams, foundations of tall structures and large span bridges, off-shore oil platforms, and large underground tunnels and caverns in difficult ground conditions. Geotechnical engineers also know how to design foundations for machines which operate at a very high frequency. The conditions responsible for liquefaction of soils and the phenomenon of landslides have also been understood to a great extent. Geotechnical engineers have also developed so many ground improvement techniques for construction of infrastructure in poor soil conditions. However, if at all there is a major problem and which is most unfortunate, it is that the state of the practice does not match so much with the state of the art already developed. Even when the knowledge exists, either economics or ignorance or lack of time leads to harmful and at times dangerous practices.

Think of a situation wherein infrastructure development in our country keeps pace with the ever growing population and large scale urbanization; imagine a situation wherein the present day development provides for municipal and industrial waste management in all cities, affordable housing, transportation systems, water supply, and electricity to all. Think of a situation where foundations and tunnel linings are built using totally new concepts which strengthen and stiffen the poor foundation soil or poor rock surrounding the tunnel. Imagine a situation where advanced electronic systems give warnings of impending earthquakes, cyclones and landslides and hence also give sufficient time to prevent loss of life and property. It is very difficult to think of such a situation because it is totally different from the condition of society we are living in. However, with adequate investment in research and development in geotechnical engineering, some although not all of these, may be within our reach.

✉ M. N. Viladkar
sumanfce@iitr.ac.in

[1] Department of Civil Engineering, Indian Institute of Technology Roorkee, Roorkee, Uttarakhand 247 667, India

With the change of times, the nature of our problems has changed. There cannot be any engineering project that has no reference to the impact of design on economics, social structures, and environment. Sustainability has become crucial and has been recognized by the engineering profession. At national level, National Green Tribunal (NGT) has been established as a watchdog. Geotechnical engineering as a discipline and practice can and should therefore change. Geotechnical engineers should look to new technologies and approaches to solve problems faster, better, and cheaper. The problems the geotechnical engineers deal with are important to the society, and the old or the conventional approaches may not be adequate to deal with the future technological challenges, rather the future challenges may have to be solved by new technological and more inter-disciplinary or multi-disciplinary approaches. Geotechnical engineers, with their focus on Earth as a resource, should be ready to widen their roles and lead to solution of more challenging problems such as wider use of underground space, more complex urban systems, discovery and recovery of new energy resources, and some of the extreme loading situations not considered so far.

In this work, initially an attempt has been made to discuss some of the present day geo-mechanical challenges in the form of case studies and some innovative solutions provided. These are the studies which involve—(1) impact, penetration, and blast loading, (2) soil–structure interaction of tall structures during extreme wind conditions, and (3) tunneling in squeezing ground conditions. Subsequently, an attempt has also been made to project some new challenging problems which today's young geotechnical engineers may have to face in the near future. The young engineers therefore have to gear up to adapt to new multi-disciplinary approaches in order to provide appropriate and viable solutions to the new challenging problems.

Investigation of an Underground Technical Facility Under Impact, Penetration and Blast Loading

The Problem

A few special structures like nuclear containment, large underground storages for strategic purposes, underground bunkers for defense purposes, etc. may experience impact and blast loads during their service life in addition to the conventional loads. Even though the probability of occurrence of this loading is very low, however, its consequences can be highly disastrous. It is therefore important to carry out a detail analysis and design of such structures under extreme events and understand their response. Under consideration is the case of design and construction of a large underground storage facility for a special purpose [1]. The facility included a network of tunnels for transportation purpose and caverns for storages. Figure 1 shows a typical section along the 890 m long tunnel between two end portals, P1 and P3, which passes through different geological formations as stated in Table 1.

The primary issue was the concern regarding the safety of tunnel portion near portals, P1 and P3. Due to low to very low depth of overburden (2.0–6.5 m), these tunnel portions were constructed by cut and cover method up to a distance of 130 m from P1 end and up to a distance of 90 m from P3 end. The rest of the tunnel was constructed by conventional drill and blast method. In an extreme event of an enemy missile directly hitting this cut and cover portion of tunnels, the entire technical facility would be left inaccessible and redundant. In view of the very low depth of overburden, the original designs were therefore modified by providing another burster tunnel which enclosed and protected the approach portion of main tunnel and the space between the two tunnels was filled with compacted sand.

Figure 2 shows the cross section of this configuration and Fig. 3 shows the configuration of the impacting missile. This case study therefore involves three dimensional dynamic finite element analysis of the tunnel configuration near the portals against any possible missile attack. The analysis includes investigation into the response of modified configuration of tunnel subjected to:

1. Impact due to direct hit of an incoming missile weighing 1020 lbs or 462 kg,
2. Penetration of missile into the overburden material and possibly further into RC burster tunnel and also the sand layer, and
3. Subsequent explosion of missile when it comes to rest.

Figure 4 shows layout of both longitudinal and hoop reinforcement in the main tunnel and Fig. 5 shows typical outer layer reinforcement layout of the curved burster slab. The complete tunnel assembly consists of a 1.2 m thick reinforced concrete main tunnel. A 3 m think sand layer is sandwiched between the main tunnel and 1.2 m thick curved burster tunnel. Rock cover above the burster slab varies from 2 m to about 6.5 m. The hoop reinforcement in the main tunnel is in the form of tor steel bars, 32 mm ϕ @125 mm c/c while the longitudinal reinforcement is 25 mm ϕ tor steel bars @250 mm c/c at both the faces. The hoop reinforcement in the curved burster slab consists of 32 mm ϕ tor steel bars @125 mm c/c whereas the longitudinal reinforcement includes 25 mm tor steel bars @125 mm c/c.

Three Dimensional Finite Element Modeling

Modelling of Tunnel Components

The components of the tunnel were modelled using ABAQUS/CAE [2]. The missile was modelled as a rigid

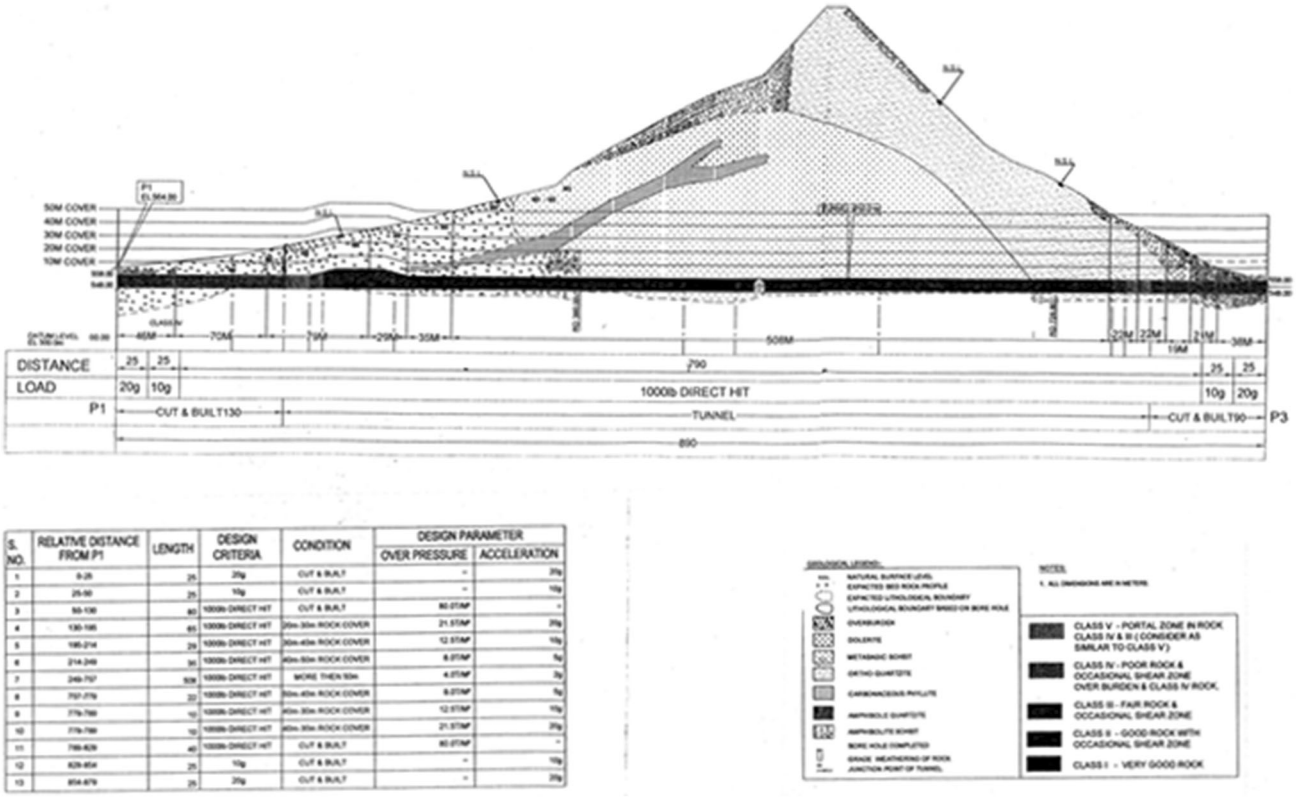

Fig. 1 Typical section along the 890 m long tunnel between two end portals, P1 and P3

Table 1 Geological formation along length of tunnel [1]

Chainage (m)	Rock type	Rock class	Range of RMR	Remarks
0–130	Amphibolite Schist	IV, poor rock	21–40	Near portal P1, overburden material
130–150	Amphibolite Schist	V, very poor rock	< 20	Overburden material
150–160	Amphibolite Schist	IV, poor rock	21–40	Overburden material
160–215	Amphibolite Schist	III, fair rock	41–60	Overburden material, occasional shear zone
215–360	Amphibolite Schist	III, fair rock	41–60	Overburden material, occasional shear zone
360–437.5	Amphibolite Schist and Dolerite	II, good rock	61–80	Dolerite only from 20 m and above, occasional shear zone
437.5–478	Dolerite	I, very good rock	81–100	–
478–707.5	Dolerite	II, good rock	61–80	Dolerite with occasional shear zone
707.5–810	Ortho-quartzite	III, fair rock	41–60	
810–890	Amphibolite Schist	IV, poor rock	21–40	Near portal P3, overburden material

body with mass and velocity assigned with the help of a reference point at the centroid of missile. Each component of the tunnel assembly was modelled as a three-dimensional deformable body. After modelling, the components were assembled using the "Assembly" module of the code in the appropriate manner as shown in Fig. 2. The

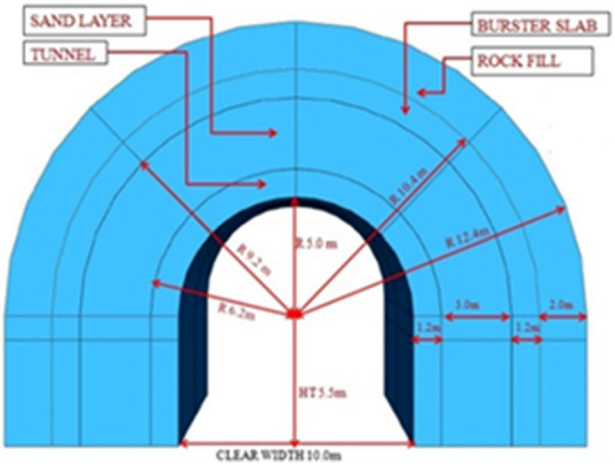

Fig. 2 Section of complete tunnel assembly

details of finite element simulation are summarized in Table 2. Figures 4, 5, 6 and 7 show respectively the meshing details of circular burster slab, sand layer and rock layer, and steel reinforcement. The total number of elements required was 308,690. The surface to surface kinematic contact algorithm was employed for assigning the contact between the surfaces of the contacting bodies.

Boundary Conditions

Each component of the tunnel assembly was considered fixed at the base with respect to all degrees of freedom. The impact velocity of missile was assigned as 200 m/s.

Impact and Blast Loading: Some Important Facts

1. There is no specific guide line (Indian Standard) for the impact and blast resistant structural design. This is due to the fact that the probability of these incidents is very low.
2. Stress–strain response of concrete, steel, soils, and rocks is significantly affected by two parameters, namely the strain rate and temperature, both of which are predominant during impact and blast loading.
3. The ballistic resistance of a target is significantly affected by the ratio of the projectile diameter to target thickness, angle of incidence of projectile, projectile mass and the shape of its nose.
4. The objective of a missile is to penetrate the target up to a maximum depth before undergoing explosion. 'Hard' missile causes both local damage and global damage to the target. At a very high velocity of missile, spalling associated with crater formation, perforation and scabbing of concrete, all occur at the same time.
5. During impact, a portion of the total kinetic energy of impacting missile is converted into strain energy associated with the missile deformation. The remainder of the energy is absorbed by the target. This absorbed energy results in overall target response that includes bending and shear deformations. Overall target collapse is prevented by designing it so as to have reserve strain energy capacity greater than the total absorbed energy.
6. The blast wave generated due to an explosion imposes a dynamic load on any object within its surroundings. This dynamic load is characterized by rapidly reaching its peak value within a very short time, which then decreases as the blast wave decays (Fig. 8). In general, total blast effect on any structure may be assumed to be dependent on: (a) initial reflected pressure; (b) the incident wave pressure; and (c) the drag pressure. The net effect of blast load is determined by interaction of

Fig. 3 Projectile geometry

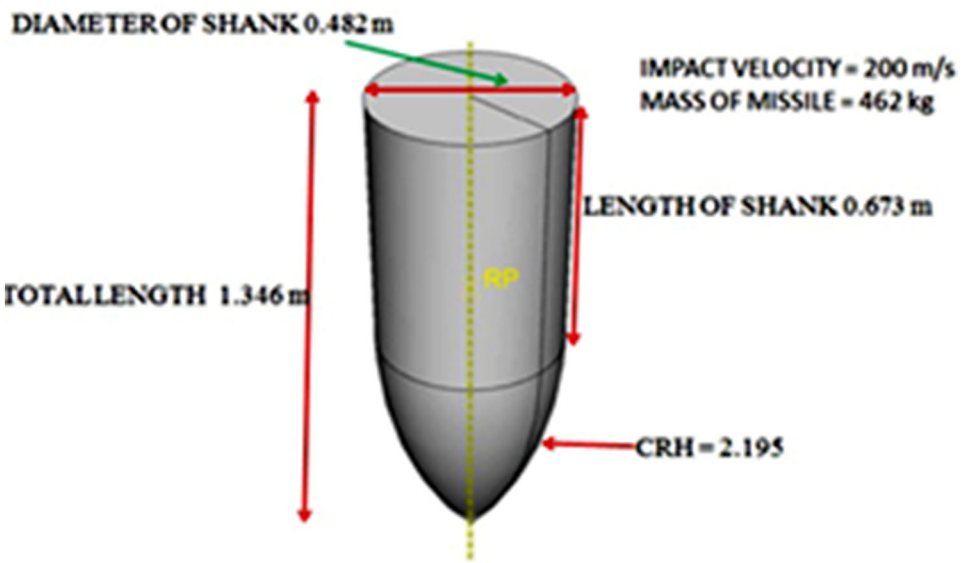

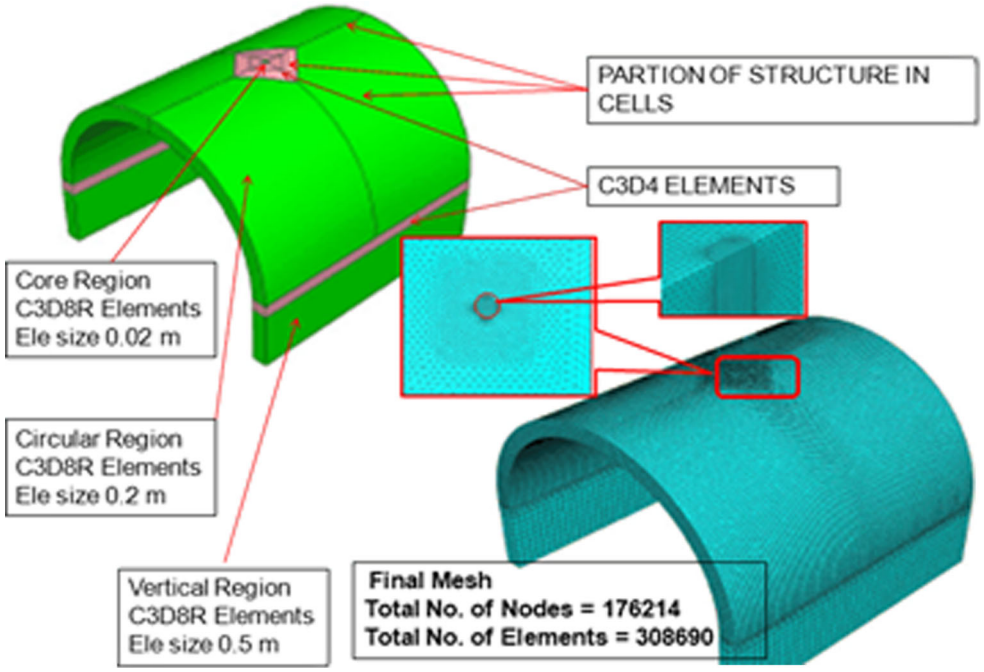

Fig. 4 Meshing details of curved burster slab

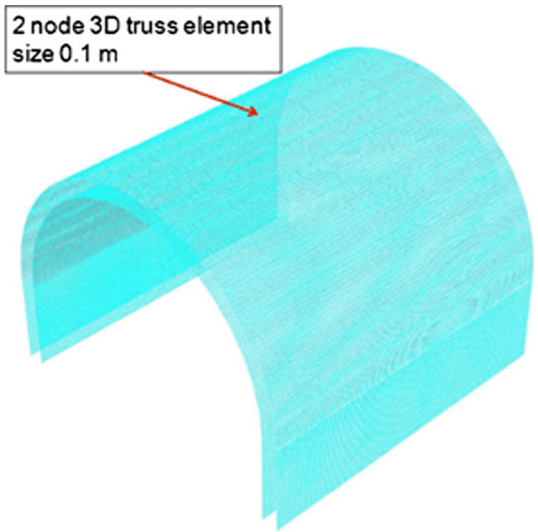

Fig. 5 Meshing details of steel reinforcement in curved burster slab

the above three components which would depend on the geometry of the structure and its position relative to the explosive source. In order to analyze any structure subjected to blast loading, a suitable simulation of these loadings is necessary.

Constitutive Modelling

Concrete

1. Damage plasticity model

The material behavior of concrete was modelled using continuum plasticity based damage model that is capable of modelling quasi-brittle materials like concrete and the rebar by using conventional biaxial stress–strain plasticity model [4]. It assumes that the two main failure mechanisms are tensile cracking and compressive crushing of the concrete material. The evolution of the yield (or failure) surface is controlled by two hardening variables namely, equivalent plastic strain, $\tilde{\varepsilon}_t^{pl}$ in tension and equivalent plastic strain, $\tilde{\varepsilon}_c^{pl}$, in compression. The compressive behavior of concrete is defined through stress–strain curve of concrete by entering the stress and inelastic strain in ABAQUS/explicit.

2. Uni-axial tension and compression behavior

The model assumes that uni-axial tensile and compressive response of concrete is characterized by damaged plasticity, as shown in Fig. 9. The degradation of the elastic stiffness is characterized by two damage variables, d_t and d_c, which are assumed to be functions of the plastic strains, temperature, and field variables:

$$\sigma_t = (1 - d_t)\, E_o \left(\varepsilon_t - \tilde{\varepsilon_t}^{pl}\right) \quad (1)$$

$$\sigma_c = (1 - d_c)\, E_o \left(\varepsilon_c - \tilde{\varepsilon_c}^{pl}\right) \quad (2)$$

Damage parameter, d_t is defined as the ratio of cracking strain to total strain whereas damage parameter, d_c is defined as the ratio of inelastic strain to total strain.

3. Interaction with reinforcement

Effects associated with the rebar/concrete interface, such as bond slip and dowel action, are modelled approximately by introducing some "tension stiffening" into the concrete

Table 2 Summary of finite element modelling

Component	Modelled as	Finite element type	Size (m)	Remarks
Missile	Rigid body	–	L = 1.346 Dia. = 0.482	Mass and velocity assigned with respect to centroid of missile
Core or contact region around missile	Deformable body	3D 8 noded brick	0.02 × 0.02 × 0.02	Contact region equals diameter of missile
Outer region	Deformable body	3D 8 noded brick	0.2 × 0.2 × 0.2	Not in contact with missile
Transition region	Deformable body	3D 4 noded wedge	0.20–0.40	
Steel reinforcement in main tunnel	Deformable body	2 noded truss element	0.10, cover = 40 mm	Using embedded element technique, all components after modelling assembled using assembly module
Steel reinforcement in curved burster tunnel	Deformable body	2 noded truss element	0.10, concrete cover = 40 mm	
Interaction between concrete and steel	Surface to surface kinematic contact algorithm	–	–	Contact assigned only after assembly of different components
Interaction between concrete and sand			μ = 0.60 assigned between concrete and sand and concrete and rock	Contact assigned only after assembly of different components

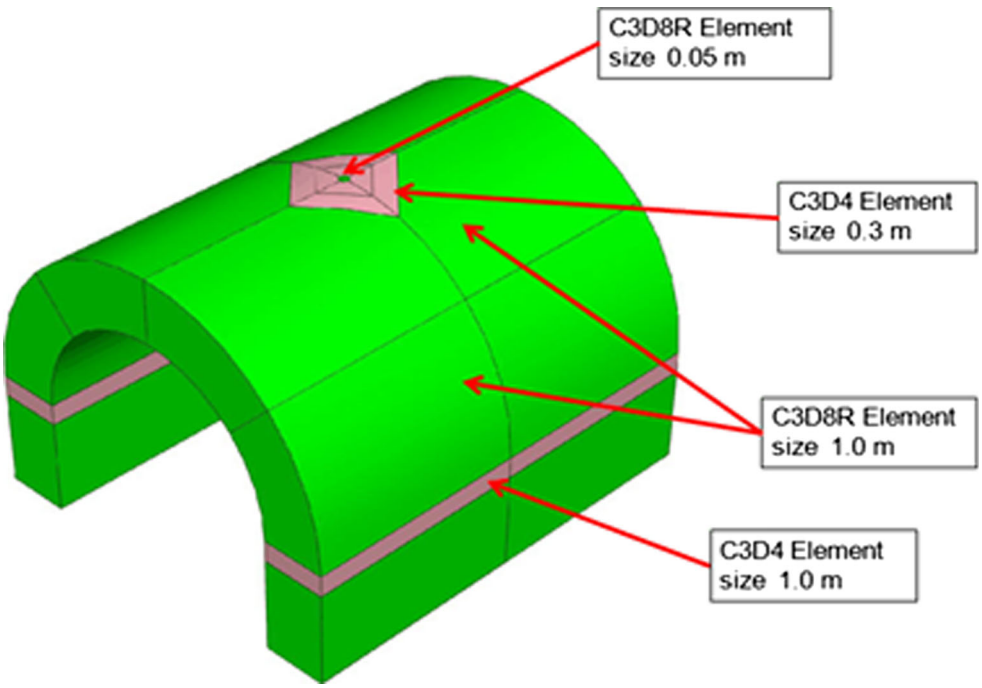

Fig. 6 Meshing details of sand layer

modelling to simulate load transfer across cracks through the rebar. The post failure behavior for direct straining is modelled with tension stiffening, which allows one to define the strain-softening behavior for cracked concrete.

4. Fracture energy cracking criterion

When there is no reinforcement in significant regions of the model, tension stiffening approach described above will introduce unreasonable mesh sensitivity into the results.

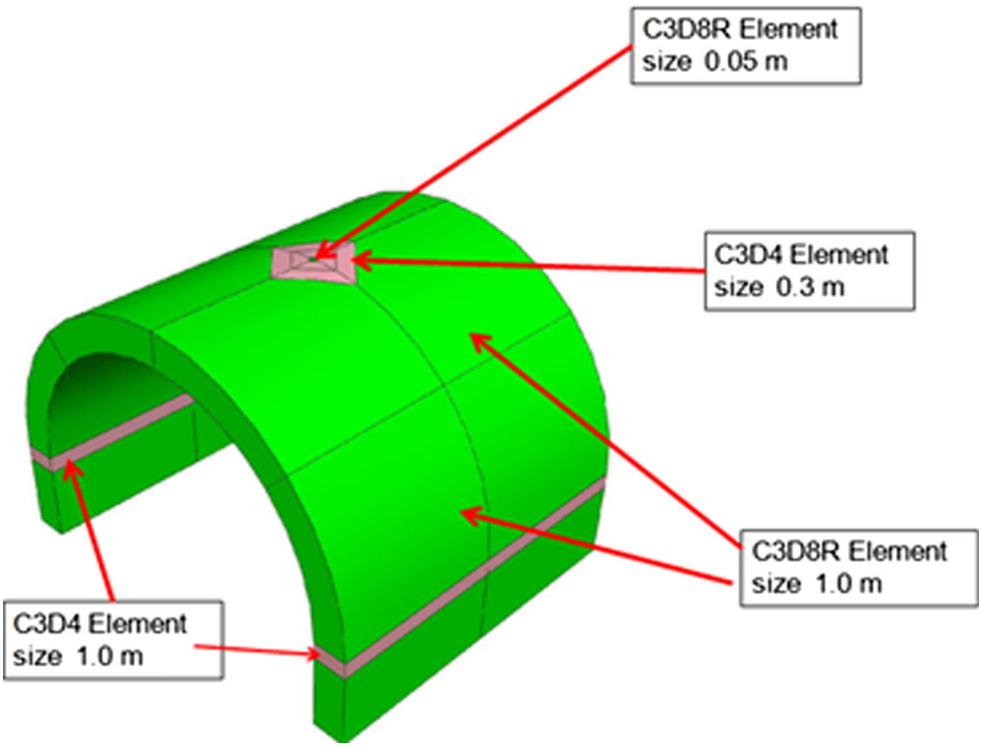

Fig. 7 Meshing details of rock layer

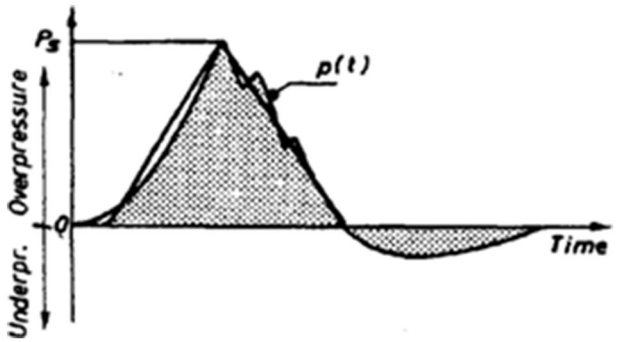

Fig. 8 Typical calculated and idealized blast loads [3]

However, it is generally accepted that Hillerborg's [5] fracture energy proposal is adequate to allay the concern for many practical purposes. It defines the energy required to open a unit area of crack, G_f, as a material parameter, using brittle fracture concepts. There are two ways of defining fracture energy cracking criterion namely, (1) post failure stress-displacement curve, and (2) post failure stress-fracture energy curve. In the present study, the second approach, which assumes a linear loss of strength after cracking, has been used (Fig. 10). Figure 11 shows typical stress–strain curve for concrete under cyclic loading. The properties of concrete are presented in Table 3.

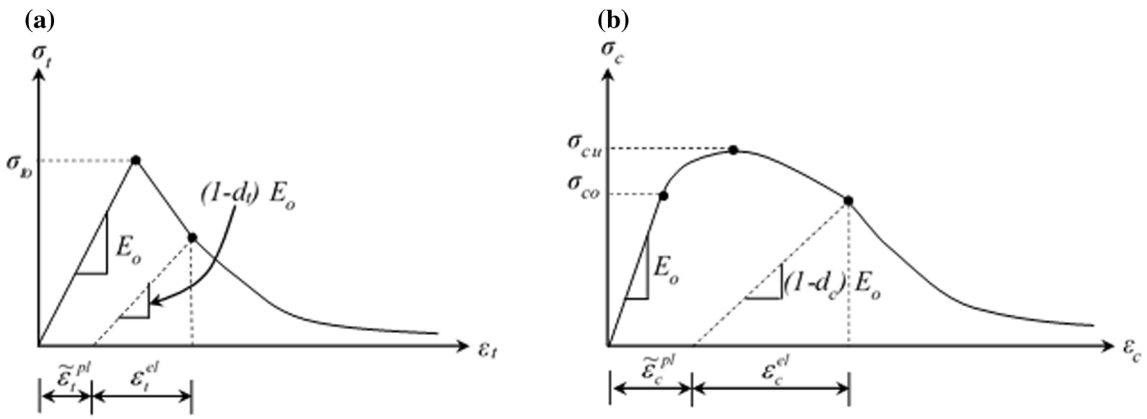

Fig. 9 Response of concrete to uni-axial loading in: **a** tension and **b** compression

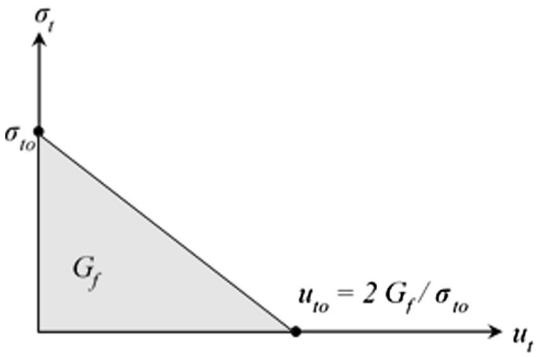

Fig. 10 Post failure stress-fracture energy curve

The compression hardening data is presented in Table 4 which also presents damage data for concrete in tension and compression in which damage parameters were obtained using Eqs. 1 and 2 and Fig. 11.

Modelling of Sand and Rock

The material behavior of sand and rock was modelled using the extended Drucker–Prager Plasticity model available in ABAQUS. This model accounts for a higher compressive yield strength than the tensile yield strength, allows a material to harden and/or soften isotropically, and generally allows for volume change with inelastic behavior: the plastic flow rule defining the inelastic straining allows simultaneous inelastic dilation and inelastic shearing. The various parameters used for sand and rock are presented in Table 5.

Modelling of Reinforcement

The material behavior of steel in main tunnel and burster tunnel was modelled using Johnson–Cook elasto-visco-plastic model [7, 8] and the ductile damage model.

1. Mises yield surfaces

The Mises yield surface has been used to define isotropic yielding. It is defined by the uni-axial yield stress as a function of uni-axial equivalent plastic strain, temperature (Table 6), and/or field variables.

2. Damage initiation criterion for fracture of metals

(a) Ductile criterion

The ductile criterion is a phenomenological model for predicting the onset of damage due to nucleation, growth, and coalescence of voids. The model assumes that the equivalent plastic strain at the onset of damage, $\bar{\varepsilon}_D^{pl}$, is a function of stress tri-axiality and strain rate: $\bar{\varepsilon}_D^{pl}\left(\eta, \dot{\bar{\varepsilon}}^{pl}\right)$, where $\eta = -p/q$ is the stress tri-axiality, p is the confining stress, q is the Mises equivalent stress, and $\dot{\bar{\varepsilon}}^{pl}$ is the equivalent plastic strain rate. The criterion for damage initiation is met when the following condition is satisfied:

$$\omega_D = \int \frac{d\bar{\varepsilon}^{pl}}{\bar{\varepsilon}_D^{pl}\left(\eta, \dot{\bar{\varepsilon}}^{pl}\right)} = 1 \tag{3}$$

Table 3 Material properties of concrete [1]

Property	Magnitude	Units
Density	2400	kg/m^3
Young's modulus	2.7386×10^{10}	N/m^2
Poisson's ratio	0.17	–
Dilation angle	30°	–
Eccentricity	1.40	–
Tensile strength	2.7	MPa
Fracture energy	90	N/m^{-1}

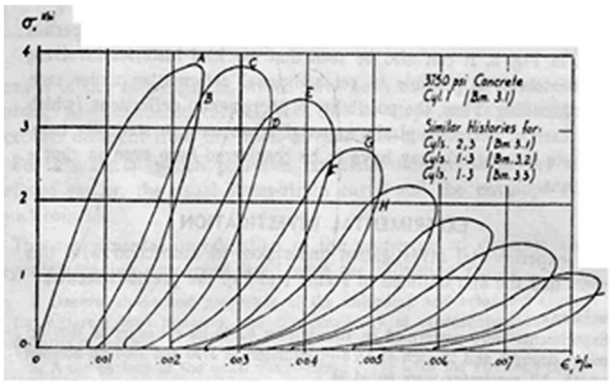

Fig. 11 Stress–strain curve for concrete under energy curve cyclic loading [6]

(b) Ductile damage model

In this model, the damage evolution law describes the rate of degradation of material stiffness once the corresponding initiation has been reached. At any time during the analysis, stress tensor in the material is given by the scalar damage equation

$$\sigma = (1 - D)\,\sigma' \tag{4}$$

where D is the overall damage variable and σ' is the effective (or undamaged) stress tensor computed in the current increment. The material loses its load-carrying capacity when $D = 1$. By default, an element is removed from the mesh if all the section points in any integration location have lost their load carrying capacity. The values of initiation parameters are considered as: fracture strain = 1.5; stress tri-axiality = 0.333 and strain rate = 0.0005.

3. Johnson–Cook plasticity model [7, 8]

(a) Johnson–Cook hardening

The equivalent von Mises stress of the Johnson–Cook model is expressed in the following form:

Table 4 Data for concrete compression hardening and damage in tension and compression [1]

Compression hardening		Concrete compression damage		Concrete tensile damage	
Yield stress (N/m^2)	In-elastic strain	Damage parameter, d_c	In-elastic strain	Damage parameter, d_t	Displacement (m)
0.976×10^7	0	0	0	0	0
2.346×10^7	0.0006	0.4573	0.00125	0.9	6.66×10^{-5}
2.5×10^7	0.0008	0.721	0.00345	–	–
2.6×10^7	0.0012	0.8005	0.0044	–	–
1.932×10^7	0.0015	0.853	0.0053	–	–
1.52×10^7	0.0027	0.916	0.0074	–	–
0.97×10^7	0.0052	–	–	–	–
0.7×10^7	0.0058	–	–	–	–

Table 5 Material parameters for sand and rock [1]

Sand	Magnitude	Rock	Magnitude
Mass density	1800 kg/m^3	Mass density	2400 kg/m^3
Young's modulus	6×10^7 N/m^2	Young's modulus	4×10^9 N/m^2
Poisson's ratio	0.3	Poisson's ratio	0.25
Friction angle	40°	Friction angle	20°
Flow stress ratio	1	Flow stress ratio	1
Dilation angle	10°	Dilation angle	0°
Yield stress	1.25×10^5 N/m^2	Yield stress	1.5×10^5 N/m^2
Absolute plastic strain	0	Absolute plastic strain	0

Table 6 Material and plasticity parameters for steel [1]

Property	Magnitude	Plasticity parameters	
		Yield stress	Plastic strain
Mass density	7850 kg/m^3	3.046×10^8	0
Young's modulus	2×10^{11} N/m^2	3.441×10^8	0.0244
Poisson's ratio	0.33	3.855×10^8	0.0951
Friction angle	40°	4.503×10^8	0.1384
		4.702×10^8	0.191
		5.0×10^8	0.2324
		5.8×10^8	0.2728

$$\bar{\sigma}\left(\bar{\varepsilon}^{pl}, \dot{\bar{\varepsilon}}^{pl}, \hat{T}\right) = \left[A + B\left(\bar{\varepsilon}^{pl}\right)^n\right]\left[1 + C\,\ln\left(\frac{\dot{\bar{\varepsilon}}^{pl}}{\dot{\varepsilon}_o}\right)\right]\left[1 - \hat{T}^m\right] \tag{5}$$

where A is quasi-static yield stress, B is a hardening constant, n is the hardening exponent, C is the strain-rate sensitivity parameter and m is the temperature sensitivity parameter. $\bar{\varepsilon}^{pl}$ is the equivalent plastic strain, $\dot{\bar{\varepsilon}}^{pl}$ is equivalent plastic strain rate, $\dot{\varepsilon}_o$ is a reference strain rate and $\hat{T}$ is non dimensional temperature defined as;

$$\hat{T} = \frac{(T - T_o)}{(T_{melt} - T_o)} \quad T_o \le T \le T_{melt} \tag{6}$$

where T is the current temperature, T_{melt} is the melting temperature and T_o is the room temperature.

(b) Johnson–Cook failure criterion

Johnson–Cook dynamic failure model assumes the failure to occur when the damage parameter exceeds a value of unity. The damage parameter is defined as:

$$\omega = \sum\left(\frac{\Delta\bar{\varepsilon}^{pl}}{\bar{\varepsilon}_f^{pl}}\right) \tag{7}$$

where $\Delta\bar{\varepsilon}^{pl}$ is an increment of the equivalent strain, $\bar{\varepsilon}_f^{pl}$ is the equivalent plastic strain at failure, and the summation is performed over all loading increments in the analysis. The strain at failure, $\bar{\varepsilon}_f^{pl}$, is assumed to be dependent on a non-dimensional plastic strain rate, dimensionless pressure-deviatoric stress ratio, (where p is the stress and q is the Mises stress); and the non-dimensional temperature, $\hat{\theta}$ defined earlier in the Johnson–Cook hardening model.

$$\bar{\varepsilon}_f^{pl} = \left[d_1 + d_2\exp\left(d_3\frac{p}{q}\right)\right]\left[1 + d_4\ln\left(\frac{\dot{\bar{\varepsilon}}^{pl}}{\dot{\varepsilon}_0}\right)\right](1 + d_5\hat{\theta}) \tag{8}$$

where d_1–d_5 are the stress tri-axiality failure parameters measured at or below the transition temperature and are a function of the necking phenomenon, and $\dot{\varepsilon}_0$ is the reference strain rate.

Response of Curved Burster Slab With and Without Reinforcement

On the basis of numerical simulation discussed above, 1.2 m thick curved burster slab (CBS) alone was first analysed to obtain its response to the impact and penetration caused by incoming 462 kg (1020 lbs) missile travelling with a velocity of 200 m/s. The penetration depth was evaluated with and without reinforcement. The depth of penetration was found to be significantly affected by the provision of reinforcement. The maximum penetration depth of the missile was found to be 0.629 m in absence of reinforcement and 0.334 m with reinforcement in the slab. Table 7 gives the comparison of extent of damage in curved burster slab when two different models are used to simulate the fracture in concrete and steel.

Response of Complete Tunnel Assembly to Missile Penetration

Complete tunnel assembly consists of all the components of the tunnel as shown in Fig. 2. The simulation was carried out to predict the maximum penetration depth in the tunnel assembly. The results obtained are presented in Figs. 12 and 13 in terms of compression and tension damage respectively. The compression damage was found to be negligible while some tensile damage was noticed at the bottom face of the curved burster slab. The values of penetration depth of the missile are presented in Table 8 along with the penetration depths obtained for flat and curved burster slabs. It was found that the missile penetrated into the rock cover up to a depth of 1.843 m and then came to rest as a result of which the missile remained stuck in the rock cover only and could not reach the burster slab. The results shown in Figs. 12 and 13 also show

Table 7 Damage comparison in curved burster slab

Case studied	Damage model	Spalling Dia. (m) Top	Scabbing Dia. (m) Bottom	Max. strain in reinforcement
CBS without reinforcement	Ductile damage for concrete	2.5	2.9	–
CBS with reinforcement	Ductile damage model for concrete and steel	2.85	5.2	0.283
CBS with reinforcement	Johnson–Cook model for reinforcement	4.1	9.0	0.335

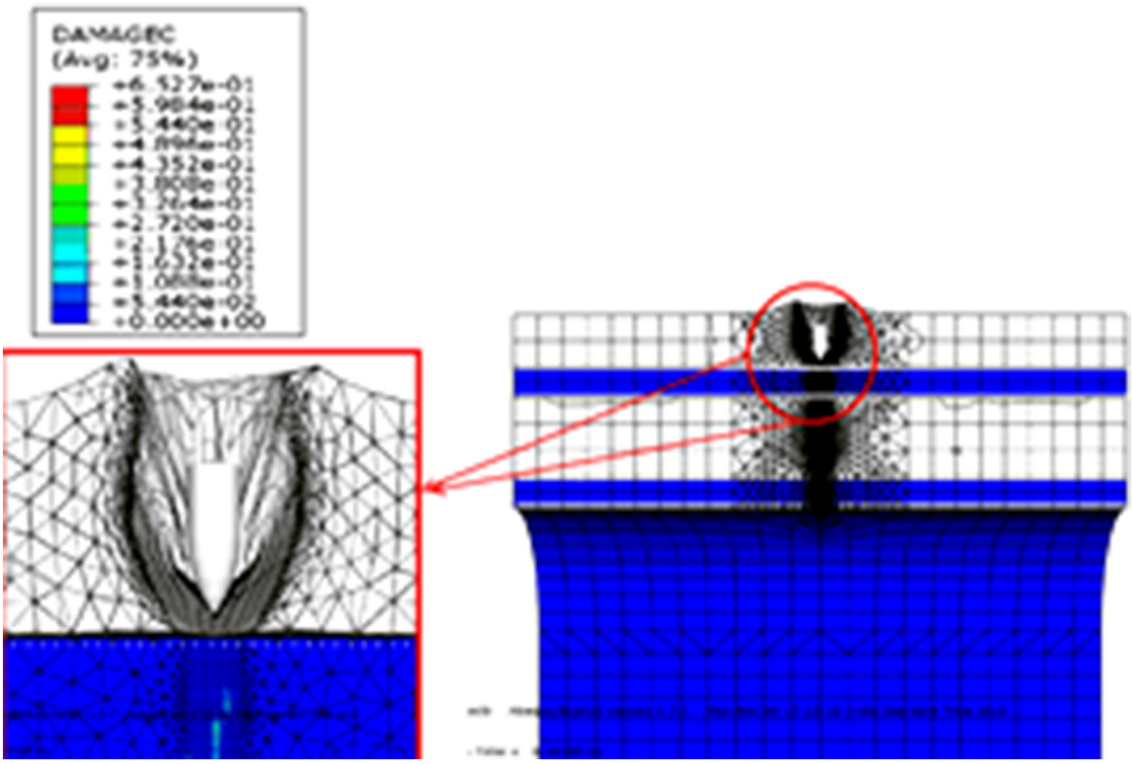

Fig. 12 Compression damage in complete tunnel assembly

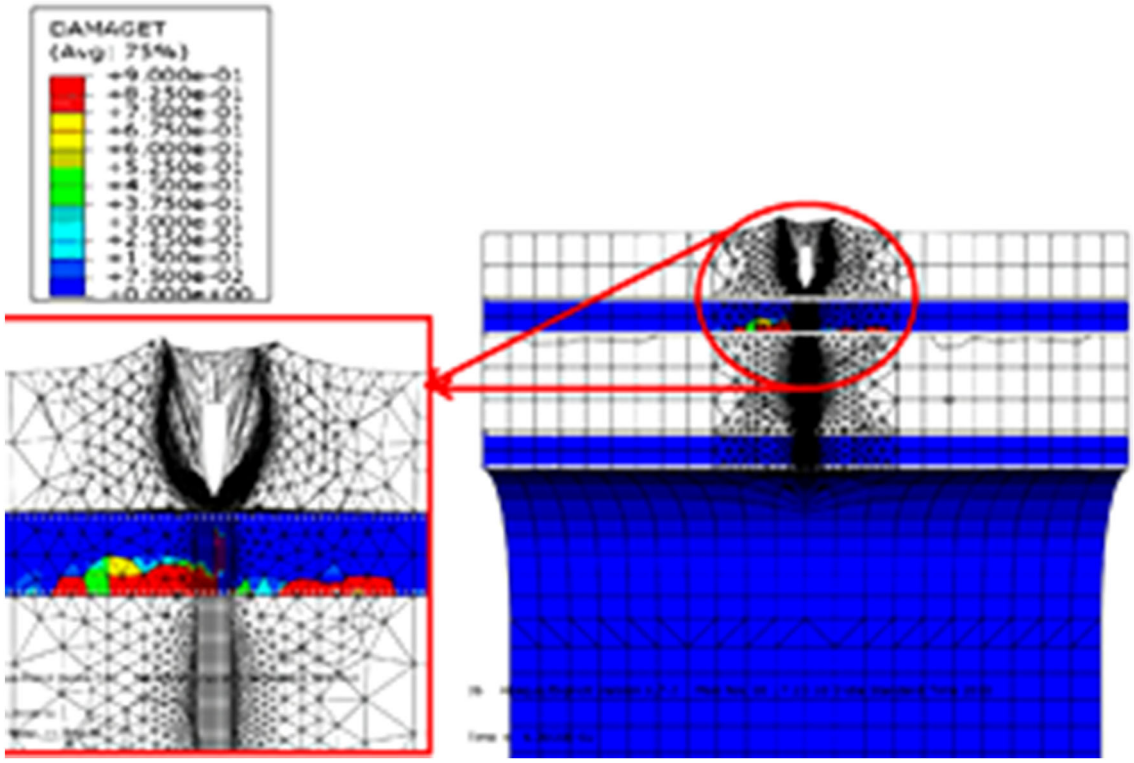

Fig. 13 Tension damage in complete tunnel assembly

Table 8 Comparison of missile penetration depth in burster slab and complete tunnel assembly

Cases studied	Penetration depth (m)		
	Without reinforcement	Reinforcement with Ductile damage model	Reinforcement with Johnson–Cook damage model
Flat burster slab	0.339	0.308	0.308
Curved burster slab	0.629	0.334	0.321
Complete tunnel assembly	–	1.843	1.843

the location of missile after maximum penetration. The burster slab experienced insignificant damage due to the penetration of the missile.

Figures 14 and 15 show respectively von-Mises stresses and deformations in the reinforcement for the tunnel and the burster slab. As such the stresses and the deformations are within the permissible limit and the whole tunnel assembly was found to be safe due to missile penetration except the deterioration of 1.8 m of rock cover.

Combined Effect of Missile Penetration and Blast Loading

Blast Loads

The magnitude and distribution of the blast load on the structure is a function of the type of explosive material, weight of the explosive and the location of explosion in relation to the protective structure. The important variables which affect the intensity of loading are (1) weapon size and distance from the structure, (2) mechanical properties of soil or rock between detonation point and the structure, and (3) depth of weapon penetration at the time of detonation (depth of burst). There are two important cases to consider in assessing the ground shock threat to buried facilities: (a) missiles that explode overhead, generally on or within the protective concrete or rock rubble overlay which causes direct loading on the roof slab, and (b) weapons that penetrate into the surrounding soil and detonate adjacent to the facility, loading the walls and floor of the structure. While general ground shock prediction equations can be applied for both these cases, however, the effect of site geology and the protective overlay requires a somewhat different application of these equations. A

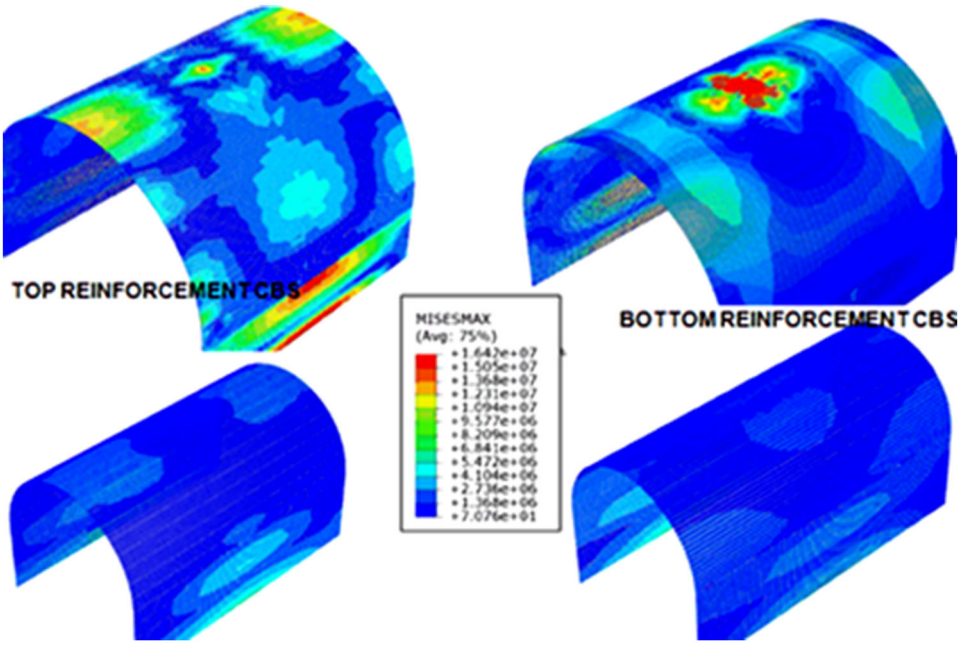

Fig. 14 Mises stress in reinforcement in complete tunnel assembly

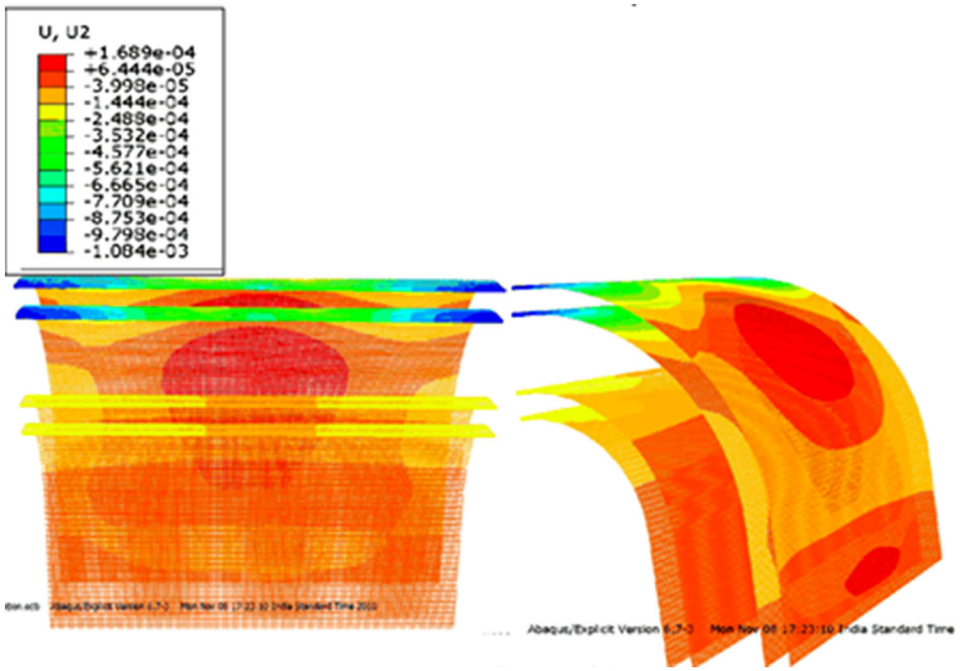

Fig. 15 Deformation of reinforcement in complete tunnel assembly

possible situation of underground structures subjected to impact and blast loading is shown in Fig. 16.

Soil Property Effects

Shock propagation through earth media is a complex function of dynamic constitutive properties of soil, the detonation products and the geometry of explosion. No single soil index or combination of indices can adequately describe the process in a single way for all the cases. Soil water content can have a profound influence, especially when soil saturation approaches 100%, pronounced increase in peak stresses and acceleration has been observed in wet clays, clay shales, and sandy clays. Granular soils with high relative density are not as strongly influenced by water saturation as the cohesive soils. However, the effect of water in sand with low relative density can produce effects similar to those seen in cohesive soils. Seismic velocity, c, often used as a crude index of soil or rock properties for ground shock prediction,

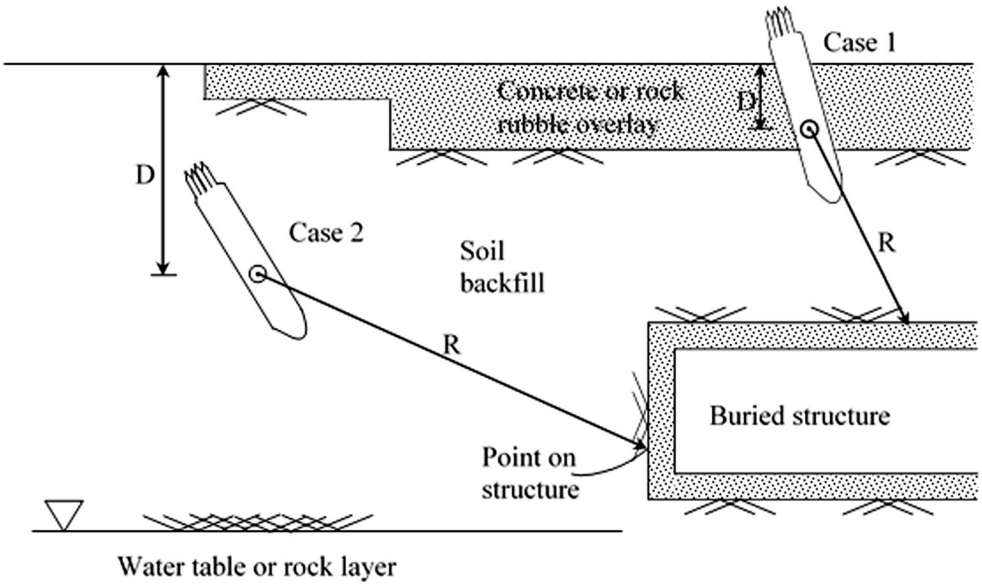

Fig. 16 Buried concrete targets subjected to impact loading [9]

provides a simple measure of the stiffness and density of soil through the relationship:

$$c = \frac{\sqrt{M}}{\rho_o} \tag{9}$$

where M is the stiffness or modulus of the soil and ρ_o is the mass density. Dry unit weight can also be an effective index for ground shock attenuation. Soils with high relative density or low volume of air voids will attenuate the ground shock more slowly than low relative density or high air void materials. Figure 17 shows the relationship between peak stresses and particle velocities from fully contained explosions in typical soils [9].

Ground Shock Predictions [1]

Stress and particle velocity pulses can be characterized by exponential type time histories that decay rapidly in amplitude and broaden as they propagate outward from the explosion. The arrival time, t_a is the elapsed time from the instant of detonation to the time at which the ground shock arrives at a given location:

$$t_a = R/c \tag{10}$$

where $R =$ distance from the explosion, $c =$ average seismic or propagation velocity at a distance R. Typically, these waveforms rise sharply to their peak value such that the rise time, t_r can be expressed as:

$$t_r = 0.1 t_a \tag{11}$$

The shock pulse decays monotonically from the peak value to nearly zero over a time period of one to three times the value of t_a, as given by the following equations:

$$P_{(t)} = P_o e^{-\alpha t/t_a}, \quad t \geq 0 \tag{12}$$

$$V_{(t)} = V_o(1 - \beta t/t_a)\, e^{-\beta t/t_a}, \quad t \geq 0 \tag{13}$$

where $P_{(t)} =$ shock stress, $V_{(t)} =$ particle velocity and α, $\beta =$ time constants and have site specific values. They can be taken as $\beta = 1/2.5$, $\alpha = 1.0$ for most applications. P_o and V_o are the peak values of shock stress and particle velocity. As the characteristic arrival time is inversely proportional to seismic velocity, explosions in high velocity media like the saturated clays produce a very short, high frequency pulse with high acceleration and low displacements. On the other hand, detonation in dry, loose materials produce ground motions of much longer duration and low frequency. Peak particle velocity and peak stress are related by the following expression:

$$P_o = \rho\, c\, V_o \tag{14}$$

where ρ is the mass density. Free field stresses and ground motions from missiles/bombs detonating within burster layer or in the soil near a structure are given by [9]:

$$P_o = f * (\rho\, c) * \left(\frac{R}{W^{\frac{1}{3}}}\right)^{-n} \tag{15}$$

$$V_o = f * 160 * \left(\frac{R}{W^{\frac{1}{3}}}\right)^{-n} \tag{16}$$

$$a_o * W^{\frac{1}{3}} = f * 50 * c * \left(\frac{R}{W^{\frac{1}{3}}}\right)^{(-n-1)} \tag{17}$$

$$\frac{d_o}{W^{\frac{1}{3}}} = f * 500\, \frac{1}{c} \left(\frac{R}{W^{\frac{1}{3}}}\right)^{(-n+1)} \tag{18}$$

$$\frac{I_o}{W^{\frac{1}{3}}} = f * \rho_o * 1.1 * \left(\frac{R}{W^{\frac{1}{3}}}\right)^{(-n+1)} \tag{19}$$

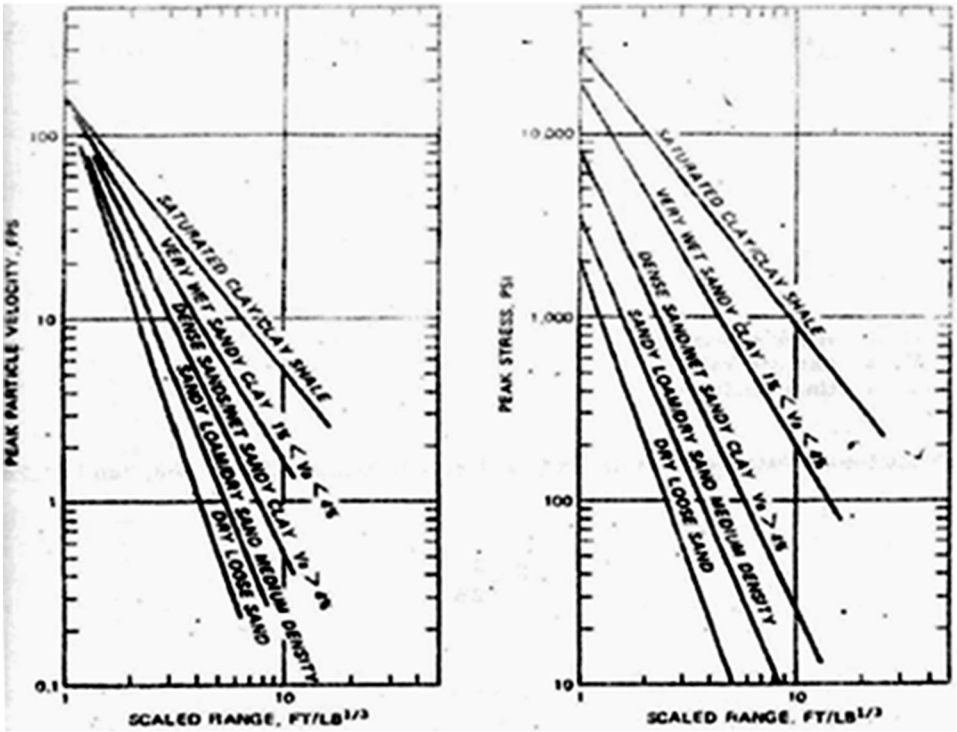

Fig. 17 Peak particle velocity and peak stress from contained explosions in soils [9]

where P_o is the peak pressure, psi; f, the coupling factor; $(\rho \cdot c)$, the acoustic impedance, psi/fps; R, the distance to the explosion, ft; W, the charge weight, lb; n, the attenuation coefficient; V_o, the peak particle velocity, fps; a_o, the peak acceleration, g/s; c, the seismic velocity, fps; d_o, the peak displacement, ft; I_o, the impulse, lb-s/in^2 and ρ_o = mass density, lb-s^2/ft^4 (Table 9). For preliminary design consideration, Table 9 can be used in selecting the seismic velocity, acoustic impedance and attenuation coefficients.

Ground Shock Coupling Factor

The magnitude of stress and ground motion is greatly enhanced as the weapon penetrates deeply into the soil or a protective burster layer, before it detonates. The concept of an equivalent effect coupling factor is introduced to account for the effect on ground shock parameters. The coupling factor, f is defined as the ratio of the ground shock magnitude from a partially buried or a shallow buried weapon (near surface burst) to that from a fully buried weapon (contained burst) in the same medium.

$$f = (P, V, d, I, a)_{near\,surface} / (P, V, d, I, a)_{contained} \quad (20)$$

A single coupling factor is applicable for all ground shock parameters which depend on the depth of burst (measured to the center of the weapon) and the medium in which the detonation occurs i.e., soil, concrete, or air. It is important to note that the coupling factor concept does not indicate the size of an equivalent charge but is a reduction factor applied to the ground shock computed for a contained burst to account for the effects of a shallow weapon detonation depth. Coupling factors are different for bursts in air, soil, and concrete and depend upon the scaled depth of burst of the weapon. These factors are shown in Fig. 18.

Discussion of Results

The methodology discussed above in "Ground Shock Predictions [1]" and "Ground Shock Coupling Factor" sections was employed to define the blast load effects on the complete assembly of (main tunnel–sand layer–burster tunnel–overburden rock). Two different structural configurations of the complete assembly were studied wherein the combined effect of missile penetration and subsequent explosion was considered. Numerical simulations were carried out initially without blast pressure to obtain the depth of penetration of missile in order to find the clear distance from detonation point to the tunnel surface. It was assumed in this study that explosion occurs after the missile has penetrated to a maximum depth. Once the penetration depth was obtained, the corresponding blast pressure was calculated using the Eq. 15 and the pressure versus time curve was generated using Eq. 12. The pressure thus calculated was uniformly distributed over the

Table 9 Soil properties for calculating ground shock parameters [9]

Material description	Seismic velocity, c (fps)	Acoustic impedance, ρc (psi/fps)	Attenuation coefficient, n
Loose, dry sand and gravels with low relative density	600	12	3–3.25
Sandy loam, loess, dry sands and backfill	1000	22	2.75
Dense sand with high relative density	1600	44	2.5
Went sandy clay with air voids (greater than 4%)	1800	48	2.5
Saturated sandy clays and sands with small amount of air voids (less than 1%)	5000	130	2.25–2.5
Heavy saturated clays and clay shales	> 5000	150–180	1.5

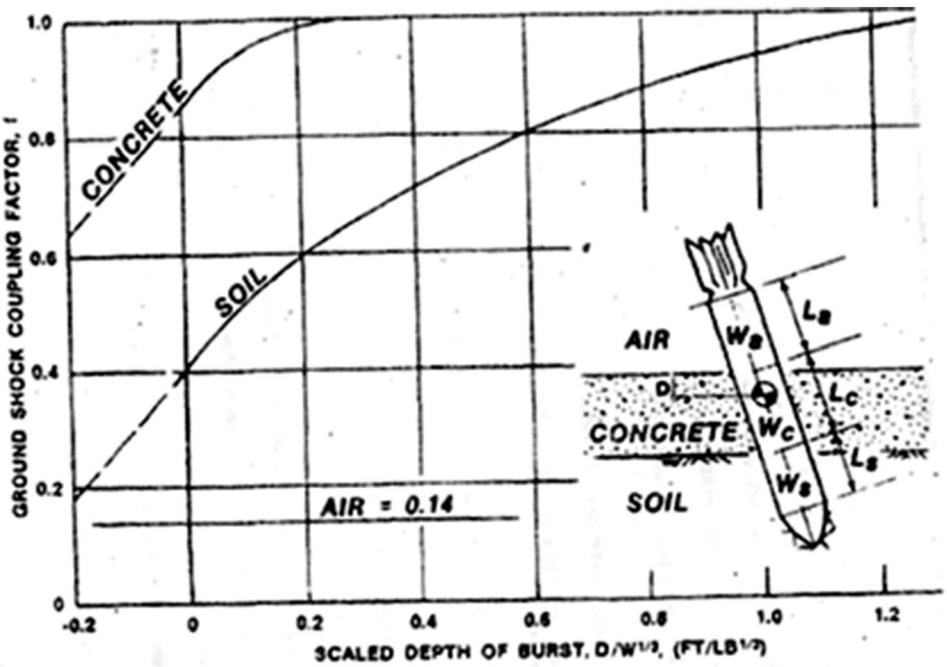

Fig. 18 Ground shock coupling factor as a function of scaled depth of burst for air, soil, and concrete [9]

circular portion of the burster tunnel. The results for two different cases studied for penetration as well as blast loading are discussed below:

Case-A: Tunnel Assembly with a 2 m Thick Rock Cover, 1.2 m Thick Burster Slab, 3.0 m Thick Sand Layer and 1.2 m Thick Main Tunnel (Fig. 19)

In this case, the missile had penetrated up to a depth of 1.843 m (Table 8) in the rock cover as shown in Fig. 20 and hence the parameter, R i.e. distance to the explosion, was found to be 5.2 m. The pressure calculated at the top of burster slab using Eq. 15 was found to be 5.87 MPa. The calculation sequence for the blast pressure is presented in Table 10.

After applying the uniformity factor obtained as 0.63 [9] and reflective pressure factor of 1.5 [9], the blast pressure works out to be 5.547 MPa. The arrival time of the shock wave, $t_a = (R/c) = (8.9 \times 3.28/4000) = 7.3 \times 10^{-3}$ s = 7.3 ms where R has been taken as the distance from detonation point to the mid plane of the circular portion of tunnel, and hence, pressure at any time instant, t can be computed by using Eq. 12 in which time, t is in milli-seconds. Therefore, $P_{(t)} = 5.54 \quad e^{-(1\times t/7.3)}$, and $P_{(1\text{ms})} = 4.83$ MPa. The pressure has reduced with an increase in time and attained a value of 1 MPa in 12 ms. A table of pressure versus time curve was thus generated and incorporated in ABAQUS. The results obtained for this case are presented in Figs. 21a–d and 22a–d in the form of normal stress and principal stresses respectively. The results obtained reveal that the intensity of the stress is low during the penetration of missile. However, after the penetrating missile comes to a halt, the influence of blast pressure increased the intensity of stresses, particularly in the tunnel to a level of 28.07 MPa compressive. The tunnel can successfully withstand these stresses without any damage.

Case-B: Tunnel Assembly Consisting of 6.5 m Thick Rock Cover, 3.0 m Thick Sand Layer and 1.2 m Thick Tunnel (Fig. 23)

In this case, the missile penetrated up to 4.8 m into the rock cover. The value of the parameter, R was accordingly found to be 5.7 m. The pressure calculated at the top of burster slab using Eq. 15 was found to be 4.67 MPa (Table 10). After applying the uniformity factor obtained as 0.63 [9] and reflective pressure factor of 1.5 [9], the blast pressure works out to be 4.48 MPa (Table 12). The arrival time of the shock wave, $t_a = (R/c) = 9.49 \times 3.28/4000 = 7.708$ ms and hence pressure at any time instant, t can be computed by using Eq. 12. Therefore, $P_{(t)} = 4.48\, e^{-(1\times t/7.708)}$, and $P_{(1\text{ms})} = 3.935$ MPa. The pressure has reduced with an increase in time and attained a value of 1 MPa in 11 ms. A table of pressure versus time curve was thus generated and incorporated in ABAQUS.

The results thus obtained are presented in Fig. 24a–d in the form of principle stresses. The blast pressure in this case has reduced significantly due to increased depth of overburden from 2.0 m in Case-A to 6.5 m in this Case-B. The maximum principal stress reached in this case is 4.76 MPa compressive. The tunnel therefore can efficiently withstand this pressure without any damage.

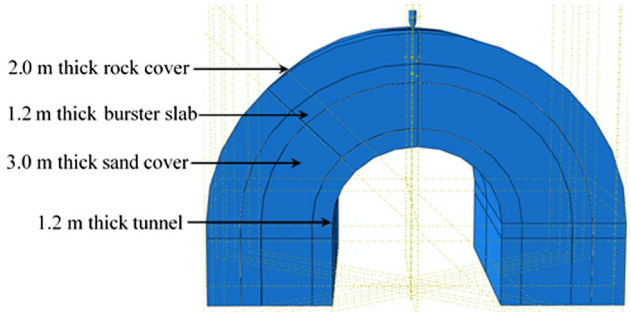

Fig. 19 Tunnel assembly with 2.0 m thick rock cover, 1.5 m thick burster slab, 3.0 m thick sand layer and 1.2 m thick tunnel

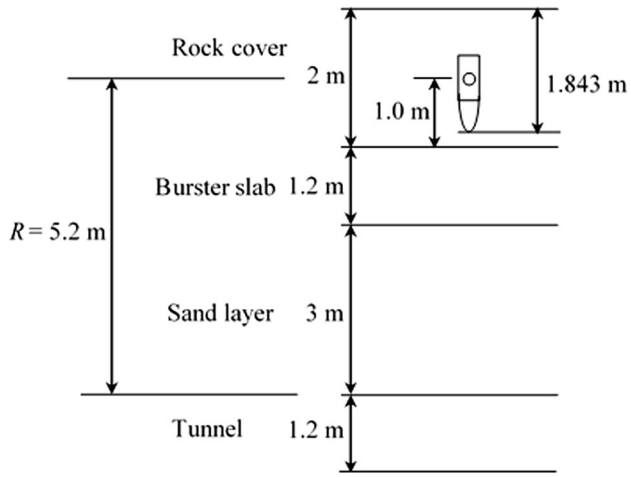

Fig. 20 Calculation of *R* for tunnel assembly

Concluding Remarks

The above study has led to the following significant conclusions:

1. The numerical experiments performed to simulate the penetration of the impacting missile clearly demonstrated that the concrete damage plasticity model proposed by Lubliner et al. [3] can reliably simulate the phenomena of penetration of a missile into a reinforced concrete slab.
2. The damage observed in case of the curved burster slab is highly localised when there is no reinforcement in the slab. However, the penetration depth is 0.629 m. In case of circular burster slab with reinforcement, the behavior observed is exactly the reverse i.e. the penetration depth of missile is 0.334 m whereas the damage has spread over a significantly larger area.
3. The study of the behavior of the complete tunnel assembly which includes the tunnel, sand layer, circular burster slab and the rock cover, has

Table 10 Calculation of blast pressure on tunnel assembly

Case	Rock cover (m)	Missile penetration, (m) Table 8	Coupling factor, *f* Figure 18	Seismic velocity, *c* (fps) Table 9	Accoustic impedance, $\rho \cdot c$ Table 9	Distance to explosion, *R* (m)	Charge weight, *W* (lbs)	Attenuation coeff., *n* Table 9	Peak pressure, P_o psi (MPa) Equation 15	Uniformity factor TM 5-855-1 [9]	Load factor TM 5-855-1 [9]	$(P_o)_{\text{mod}}$ (MPa)
A	2.0	1.843	0.65	4000	44	5.20	661	2.5	852.5 (5.87)	0.63	1.5	5.55
B	6.5	4.80	0.65	4000	44	5.70	661	2.5	678.0 (4.67)	0.64	1.5	4.48

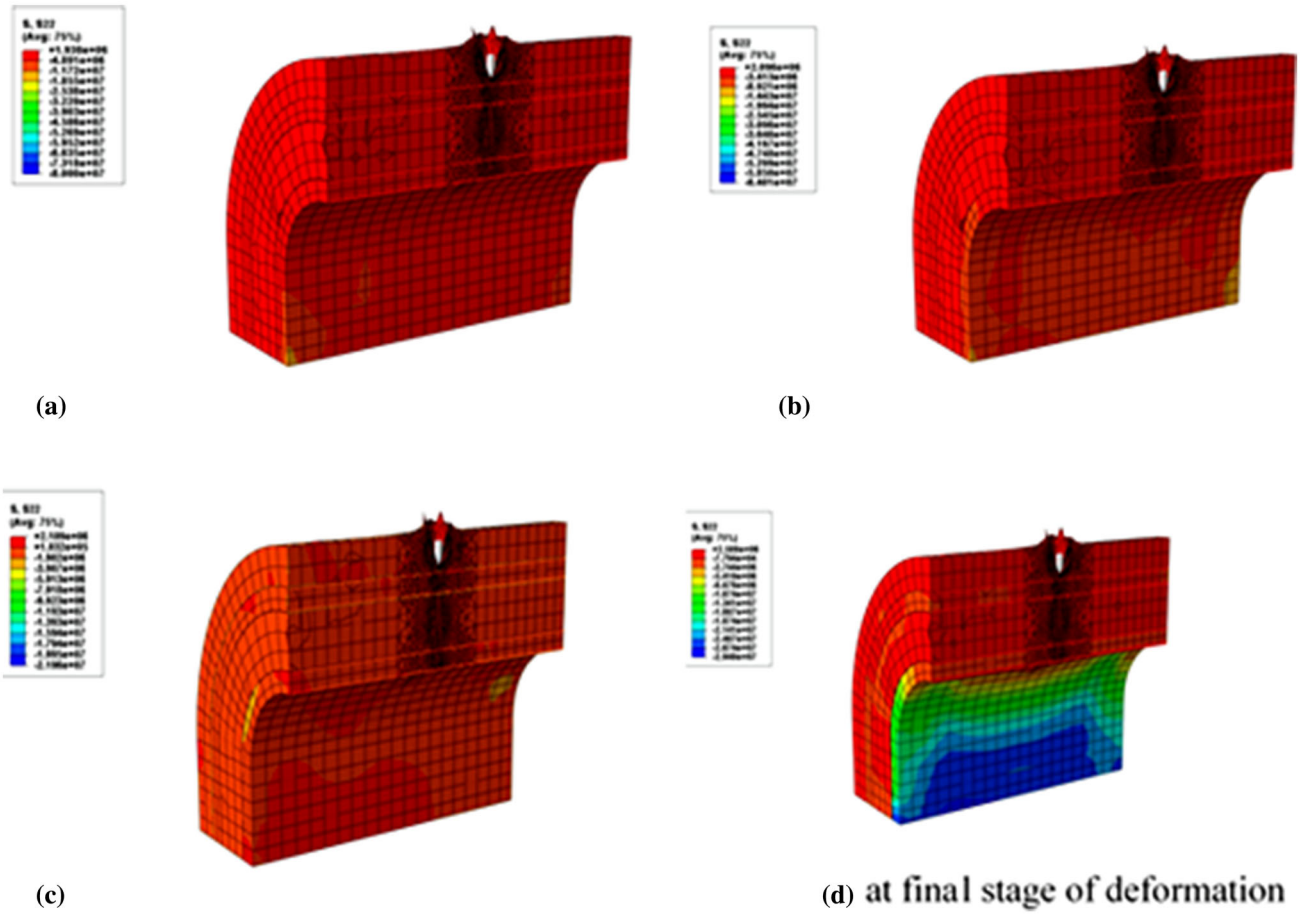

Fig. 21 Variation of normal stress (σ_{yy}) in the direction of applied load at different time instants

demonstrated that the missile can penetrate into the rock cover up to a depth of 1.843 m only and hence cannot reach the burster slab. The burster slab was found to experience negligible damage due to the penetration of missile. Both the stresses and deformations in the entire assembly were found to be within the permissible limits and therefore the whole assembly was found to be safe.

4. Two different geometric configurations were considered wherein the influence of missile penetration and blast effect were studied simultaneously The highest blast pressure was found to be 5.87 MPa for "Case A" with 2 m thick of rock cover, 1.2 m thick buster slab, 3.0 m thick sand layer and 1.2 m thick tunnel. However, the tunnel withstood this pressure without any significant deformation. For the "Case B" with 6.5 m thick rock cover, 3.0 m thick sand layer and 1.2 m thick tunnel, the blast pressure was found to be 4.67 MPa. The tunnel therefore effectively survived this pressure without any deformation.

Case Study of SSI of Industrial Cooling Towers Under Extreme Wind Loading Condition

The Problem

The present day natural draught hyperbolic cooling towers, built in several thermal and nuclear power plants, are among the largest shell structures (Fig. 25). These special structures have gained considerable importance in civil engineering field during past few decades. Such towers are hyperbolic shells of revolution supported by closely spaced inclined columns. The foundation for the columns is in the form of an annular raft or annular raft supported by raker piles, depending upon the nature of the underlying soil strata.

The main lateral loading for such structures is produced by wind, except in those cases where the earthquake forces can also be significant. The spectacular failure of cooling towers at Ferry Bridge in England in 1965 during high winds can be seen in Fig. 26 [11]. Failure of cooling towers during extreme wind also occurred at Ardeer in Scotland in 1973, at Bouchain in France in 1975 and at Fiddler's Ferry

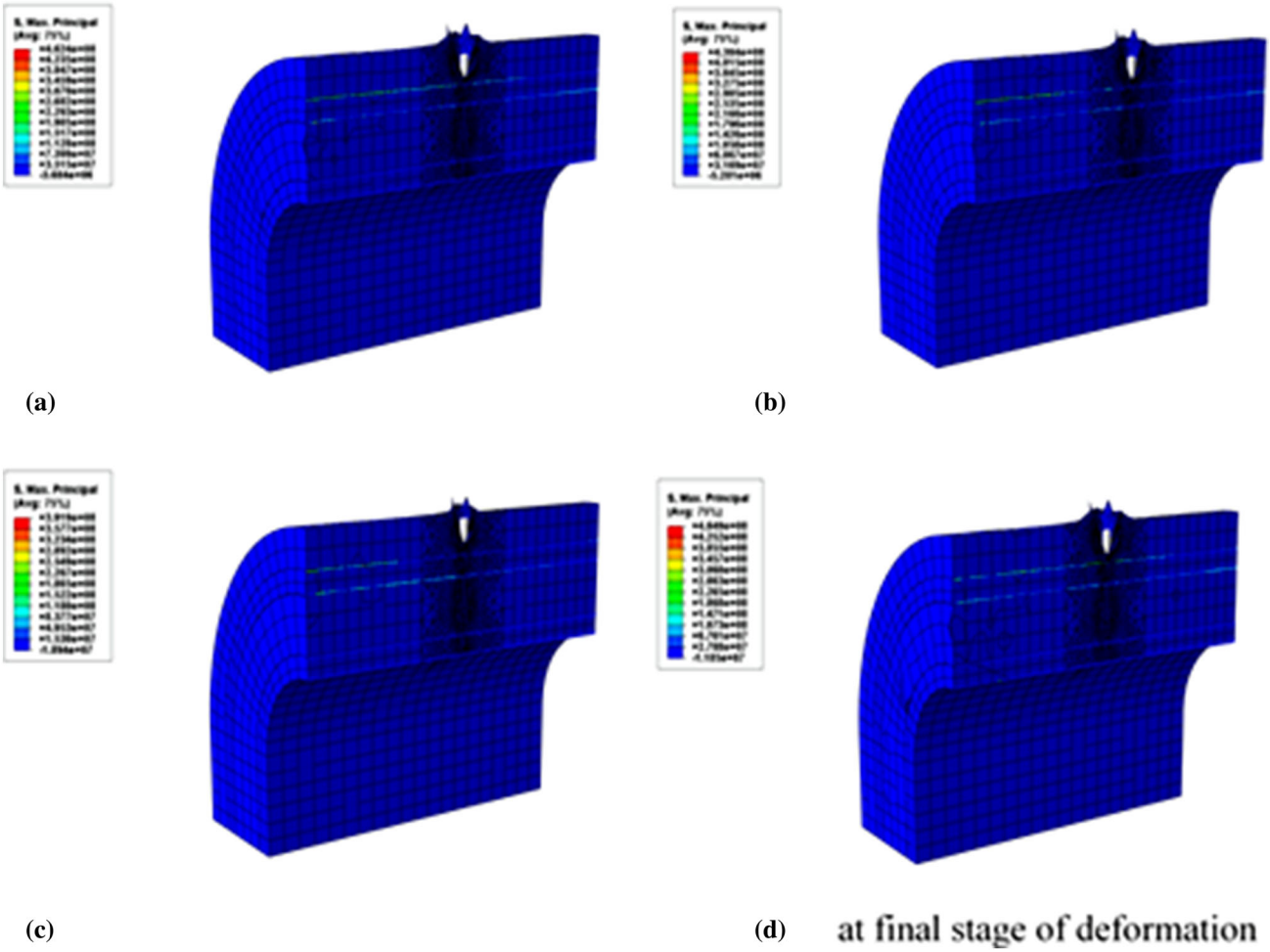

Fig. 22 Variation of maximum principal stress in the tunnel assembly

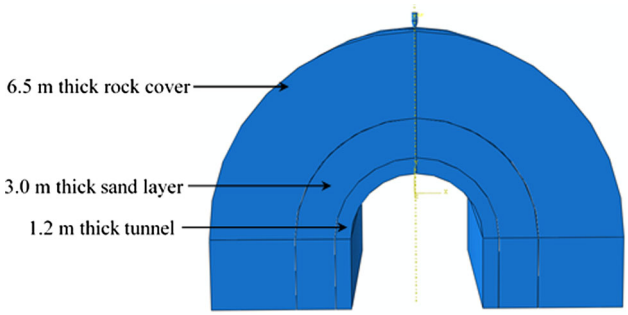

Fig. 23 Tunnel assembly with 6.5 m thick rock cover

in Yorkshire in UK in 1984. These failures attracted the attention of many investigators.

With increase in height of cooling towers and reduction in shell curvature, their flexural response to loads with unsymmetrical distribution of wind pressures became important from the point of view of the safety of the structure. The wind forces are random in nature. The wind load on a tower, will in practice, be unsymmetrical due to very nature of the wind phenomenon as well as due to the influence of other structures in close vicinity or other towers, if there is a battery of towers. Thus, a cooling tower is truly loaded with unsymmetrical dynamic loads. The simplest approach for the analysis is to work on the basis of the mean (static) symmetrical wind load, suitably modified by the 'gust factor'. However, more rigorous treatment will involve dynamic response of tower subject to loading as it actually occurs. Thus, gigantic RC shell structures need suitable numerical modelling of wind loads based on field measurements or the wind tunnel studies and physical modelling of the tower shell along with its soil-foundation system.

The influence of unequal settlement of foundation on stress resultants in the tower shell was studied by Lu et al. [12], Kato and Yoshinao [13], Kato et al. [14–16], Tilak et al. [17], Kato et al. [18], Cheong [19], Horr and Safi [20] and Viladkar et al. [21]. Shu and Wenda [22] obtained the gust factors for cooling towers considering the influence of soil medium.

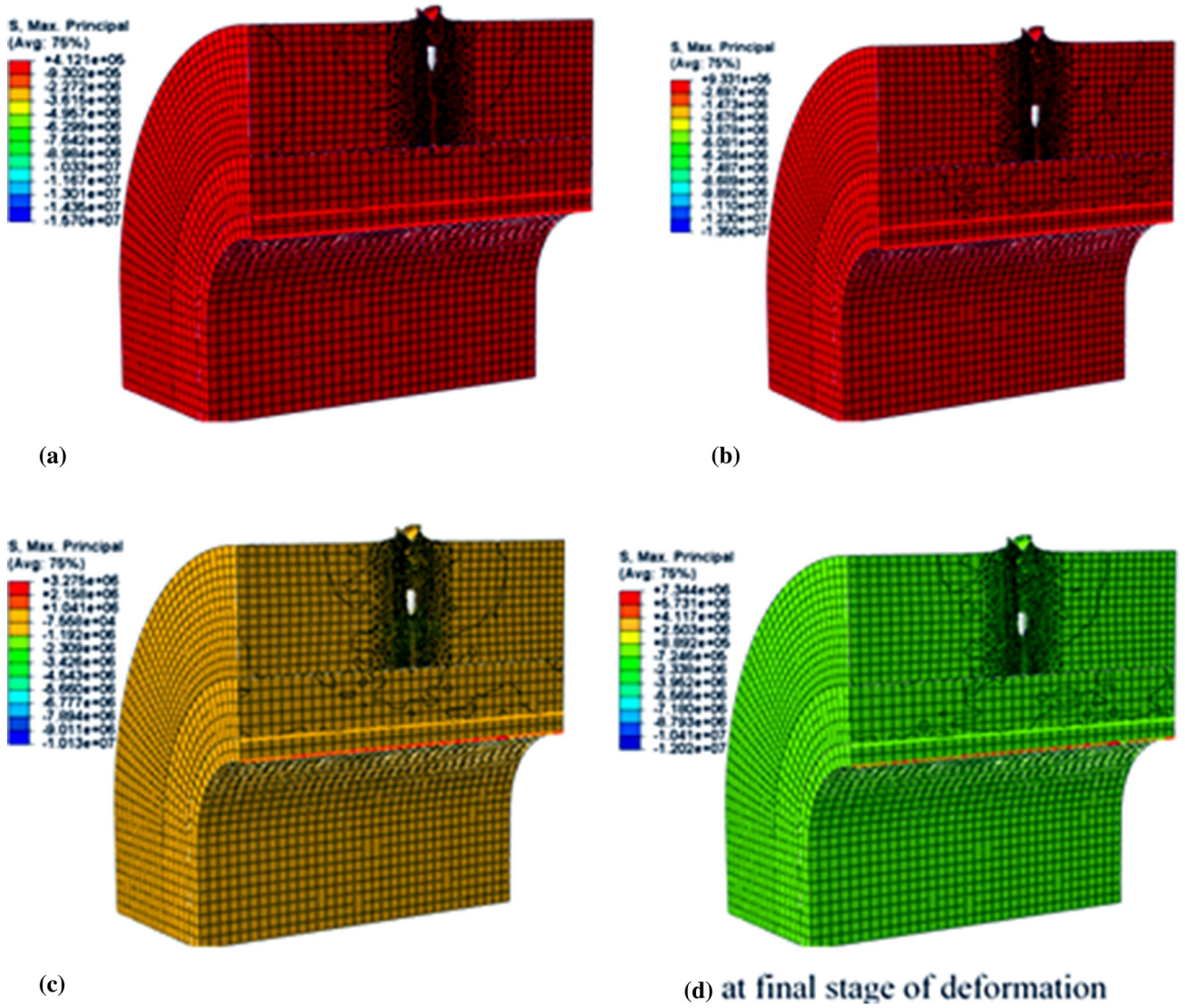

Fig. 24 Variation of maximum principal stress in tunnel assembly

Fig. 25 Cooling towers in Kakrapar nuclear power plant [10]

The case study presented here involves investigation of a cooling tower constructed for a nuclear power plant in an area where the extreme wind intensity is of the order of 50 m/s or about 180 km/h. The study was undertaken in view of the collapse of some of the cooling towers in other countries and in view of the fact that these are tall and sensitive structures, the cooling tower-foundation-soil system was therefore treated as one integral compatible unit and subjected to both symmetrical and unsymmetrical wind loading conditions. The complex nature of the problem necessitated some wind tunnel testing of model cooling tower under gradient wind loading and a sophisticated and robust modeling, which in turn would yield desirable accuracy in the response. The aim was to predict—(1) radial displacements, and membrane forces in tower shell, (2) column forces and moments in supporting A-frames, and (3) settlements, contact pressure distribution and bending moments in the annular raft, so that cooling tower and its foundation system could be designed

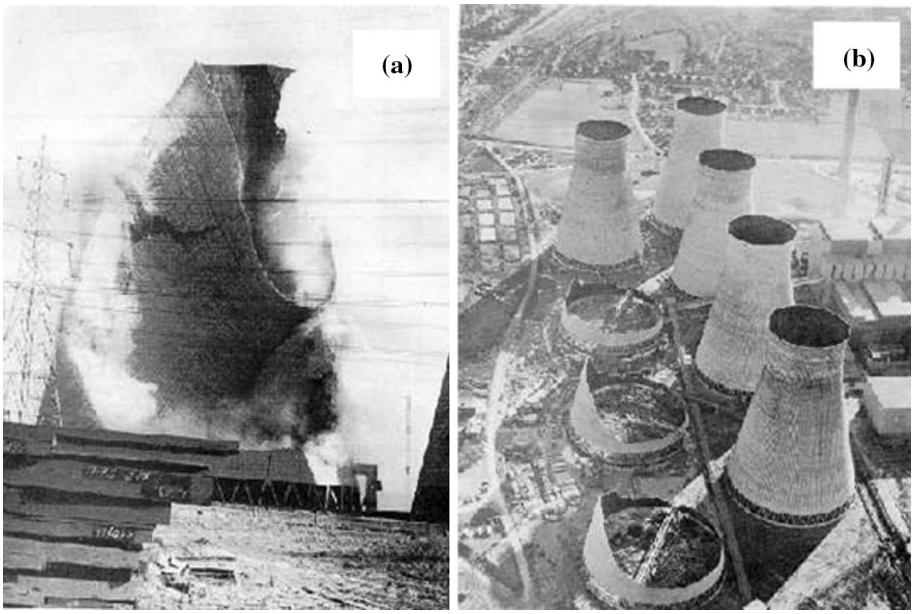

Fig. 26 **a** Ferry Bridge, tower collapse in UK during high winds; **b** aftermath of failure [11]

with sufficient confidence. The results have been compared with non-interactive response of tower in which A-frame column bases were treated as fixed at the base.

The Case Study of Cooling Tower Kakrapar Atomic Power Plant

Tower and Supporting Columns

This is a case study of cooling towers at the Kakrapar Nuclear Power Plant near Surat in Gujarat. This analysis assumed importance in view of the earlier failure of cooling towers under extreme wind conditions in some other countries. The geometry of cooling tower and supporting columns (A-frames) are presented in and Fig. 27a, b and in Table 11. The cooling tower, having a varying thickness along its height, has been supported by 88 diagonal columns and an annular raft supporting the A-frames (Fig. 27b).

Supporting Soil and Its Properties

The cooling tower-foundation system rests on a soil strata as presented in Table 12 (SSI Case-I). The soil strata consists of three layers, namely, (1) a 2 m thick layer of firm to stiff silty clay, (2) a 4 m thick layer of dense sand, and (3) a 10 m thick third layer of weathered and fragmented basalt. The values of penetration resistance are correlated with the elastic modulus, E_s of soil. The third layer below the raft is a weathered and fragmented rock for which the value of elastic modulus has been obtained on basis of rock mass rating (RMR) [23]. The fragmented basalt had a RMR of 40 and hence it falls in class IV i.e. poor rock.

Unsymmetrical Wind Load Modelling

Indian Standard code of practice [24] and British Standard [25] specify the use of the Fourier cosine series to express the circumferential wind pressure distribution (symemtrical) around a cooling tower including an allowance for internal suction.

The net mean surface unsymmetrical wind pressure distribution on the shell surface and the corresponding pressure coefficients were obtained and reported by Krishna et al. [26]. These coefficients were obtained on basis of aerodynamic tests conducted in a boundary layer wind tunnel on a 1:400 scale model of a rigid tower including the surrounding buildings and structures as a part of the power plant layout. These tests were conducted under gradient wind conditions at a wind speed corresponding to Reynolds number of 2.55×10^5. The net mean pressure coefficients (normalized with respect to pressure corresponding to wind speed at throat level) were presented by Krishna et al. [26] at different tower elevations (as measured from the throat level) and for different positions on the shell surface (Table 13). The unsymmetrical pressure distribution has been referred to herein as "measured pressure coefficients". A typical plot of pressure distribution around the circumferential direction at selected elevations has been shown in Fig. 28. The vertical profile of design wind pressure adopted in this study is similar to the one given by ACI-ASCE Committee 334 [27] report.

Karisiddappa [28] was the first to represent this unsymmetrical wind pressure distribution in terms of Fourier sine–cosine series of the form:

$$c(\phi) = \sum_{n=0}^{\infty} a_n \cos(n\phi) + \sum_{n=0}^{\infty} b_n \sin(n\phi) \quad (21)$$

where $c\ (\phi)$ are the unsymmetrical pressure coefficients, n represents the number of harmonics, a_n and b_n are the harmonic constants, and ϕ, the horizontal angle measured from the windward direction. The net mean pressure coefficients as measured in wind tunnel test at throat level of the cooling tower (column 10 in Table 13) were considered for obtaining harmonic constants, a_n and b_n of the above Fourier sine–cosine series These harmonic constants are presented in Table 14.

These constants are presented up to 13 harmonics only. Using these harmonic constants, pressure coefficients, $c\ (\phi)$ were evaluated which are plotted in Fig. 28 for some typical tower elevations. Pressure coefficients as specified by IS/BS codal provisions are also plotted in the same Fig. 28. The Design Wind Speed, V_Z is therefore obtained by modifying the basic wind speed and is expressed as per from IS: 875 (Part-3) [29] as:

$$V_Z = V_b \cdot K_1 \cdot K_2 \cdot K_3 \quad (22)$$

where V_b is the basic wind speed; K_1 is the probability factor or the risk coefficient; K_2 is the factor which accounts for the terrain, and height and size of the structure; and K_3 is the topography factor. The basic or the reference wind speed, V_b at 10 m above the ground surface, i.e. V_{10}, for the site in question was obtained from IS: 875 (Part-3) [29] as 159.50 km/h with a return period of 50 years. Similarly, factors, K_1, K_2, and K_3 were obtained from IS: 875 (Part-3) [29].

Design wind pressure, q developed by the design wind speed, is given by IS: 875 (Part-4) [30] as–

$$q = \frac{1}{2}\rho_{air}(V_Z)^2 = 0.6 \times (V_Z)^2 \quad (23a)$$

$$q = \frac{1}{2}\rho_{air}(V_Z)^2 = 0.6 \times (5/18)^2 (V_Z)^2 = 0.047\,(V_Z)^2 \quad (23b)$$

It may be noted that units of V_Z in Eq. 23a are km/h and in Eq. 23b are m/s. ρ_{air} is the mass density of air = 1.2 kg/m^3. Corresponding wind pressure at any angle, ϕ measured from the windward meridian, and at any height, z is given by:

$$p_z = c(\phi) \cdot q \cdot H(z) = c(\phi) \cdot q \cdot \left(z/z_g\right)^{2\alpha} \quad (24)$$

where z_g is the gradient height (= 10.0 m above the ground surface in this work) and is a function of ground roughness, and α is the power law index (= 0.1). The units of pressure, p_z will be kgf/m^2.

Finite Element Modelling

A system comprising tower shell, column supports, annular raft and the soil mass has been analyzed by three dimensional finite element analysis in a single step considering linear elastic behavior of all the components. Semi-Loof shell element [31, 32], which is an iso-parametric non-confirming element, is perhaps the most efficient element for the solution of shells having arbitrary geometry, accounts for both membrane and bending actions, and is particularly suitable for modeling the cooling tower shell whose Gaussian curvature is negative. Therefore, the interactive analysis of the whole system was carried out by using—(1) semi-Loof shell elements for the tower shell, (2) semi-Loof beam elements for supporting columns, (3) iso-parametric plate bending elements for annular raft and (4) eight and sixteen noded brick elements for the soil mass. Details of formulation of these elements are available elsewhere [21, 33]. As the wind load considered here happens to be unsymmetrical, full tower geometry and the soil medium were discretized. For the convenience of modeling, soil layers were considered as circular in plan. The lateral extent of soil mass considered is 7 to 8 times the width of annular raft (5.7 m) from the center line of the raft on either side. The overall discretization schedule has been presented in Table 15. All nodes of shell elements at the top of tower have been considered free. Three nodal displacements u, v and w at all nodes of the bottom most layer of soil have been restrained. For the nodes around the outer periphery of soil layers, $u = v = 0$ condition has been imposed.

Software developed for the purpose consists of a variety of elements, each with different degrees of freedom per node. Conventional Frontal Solution technique, duly modified to account for the varying element configuration, has been implemented in the present work [34, 35]. The solution therefore yields deformations at all nodal points in the continuum, rotations at various nodal points in the shell; supporting column junctions and the annular raft. It also gives stress resultants in the supporting soil continuum. The software was used to analyze the case of cooling tower shell whose geometry is described in Table 11. Interactive analysis was carried out for all the three cases of soil properties considered for the three cases, namely SSI Case-I, SSI Case-II and SSI Case-III (Table 12). The results have been compared with those obtained for the condition of fixed column bases i.e. non-interactive analysis (NIA).

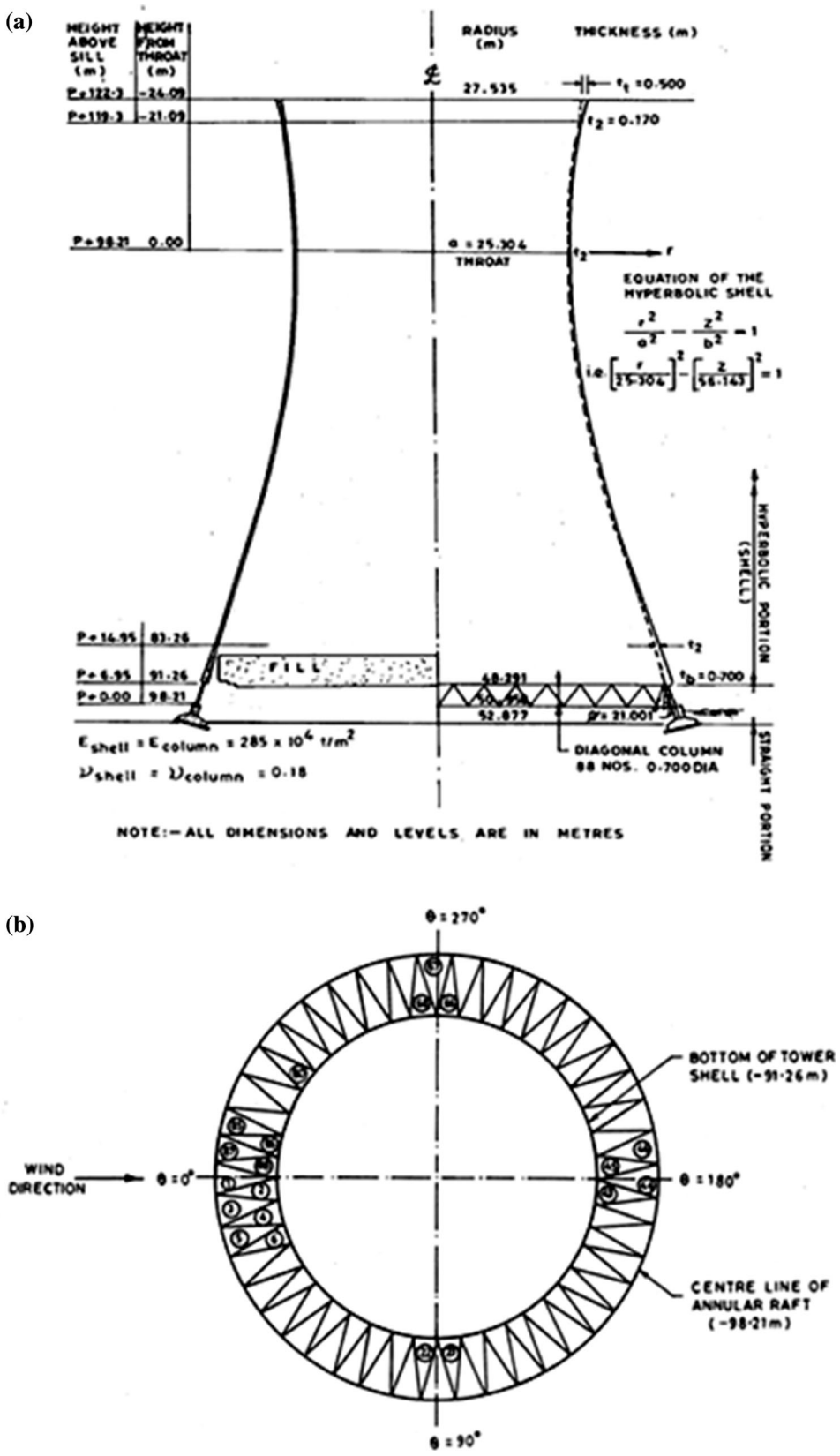

Fig. 27 **a** Geometry of the cooling tower; **b** schematic diagram showing column positions [17]

Table 11 Geometrical and material properties of hyperbolic cooling tower and its foundation

Sl. no.	Parameter description	Symbol	Parametric value
1.	Height above throat level	Z_t	24.09 m
2.	Height below throat level	Z_b	91.26 m
3.	Radius at top	r_t	27.535 m
4.	Radius at bottom	r_b	52.877 m
5.	Radius at throat level	a	25.304 m
6.	Circular spacing of column pairs (A-frames)		8.1818°
7.	Diameter of columns		0.7 m
8.	No. of column pairs (diagonal columns)		88
9.	Height of A-frames		6.95 m
10.	Shell thickness at bottom	t_b	0.7 m
11.	Shell thickness at top	t_t	0.5 m
12.	Shell thickness at throat level	T	0.17 m
13.	Young's modulus for shell and column	E	285×10^4 t/m^2
14.	Poisson's ratio for shell and column	μ	0.18
15.	Inner diameter of annular raft		96.216 m
16	Outer diameter of annular raft		107.616 m
17	Thickness of annular raft		5.0 m
18	Depth of annular raft below ground surface		5.0 m

Table 12 Description of soil layers and their properties

SSI case	Depth (m)	Strata thickness (m)	Soil type	SPT N value	Elastic modulus (t/m^2)	Poisson's ratio, μ	Remarks
I	0–2	2.0	Stiff silty clay	31	3250	0.35	Actual observed soil strata
	2–6	4.0	Dense sand	70	10,500	0.30	
	6–16	10.0	Weathered and fragmented rock	100	2,40,000	0.20	
II	0–2	2.0	Silty sand	–	1250	0.35	Considered for parametric study
	2–6	4.0	Loose sand	–	1750	0.30	
	6–16	10.0	Medium dense sand	–	3750	0.25	
III	0–2	2.0	Medium dense sand	–	3500	0.25	Considered for parametric study
	2–6	4.0	Dense sand	–	5500	0.20	
	6–16	10.0	Dense sand	–	6750	0.20	

Response of Cooling Tower to Unsymmetrical Wind Loading

Radial Displacements

The variation of radial displacements along the height of tower at $\phi = 0°$ meridian has been presented in Fig. 29a for all the four types of analyses. It has been observed that unlike the displacement profile for symmetrical wind pressure distribution (Fig. 29b), in which case the maxima of radial displacement occurs at a height of about 55.0 m below the throat level, the maxima of radial displacements due to unsymmetrical loading for both interactive and the non-interactive analyses occurs near the throat level at an elevation of − 12.21 m (Fig. 29a). Maximum radial displacement has been observed in the interactive analysis, namely SSI: case-II, which is almost three times the displacement observed in the non-interactive analysis. However, all the three interactive analyses predict higher values of radial displacements along the tower height at $\phi = 0°$ meridian.

Table 13 Net mean pressure coefficients from wind tunnel test [26]

ϕ (°)	Elevation in 'm' measured from throat level											
	− 79.60	− 69.70	− 59.80	− 50.90	− 39.80	− 29.90	− 19.84	− 9.92	0.00	10.04	19.96	23.07
0	0.73	0.88	0.80	0.68	0.76	0.65	0.65	1.11	1.23	1.27	1.22	0.58
10	0.66	0.89	0.75	0.66	0.80	0.65	0.73	1.11	1.29	1.28	1.31	0.74
20	0.53	0.77	0.63	0.56	0.73	0.55	0.65	1.18	1.14	1.12	1.14	0.89
30	0.36	0.45	0.39	0.36	0.50	0.31	0.47	1.05	0.82	0.83	0.77	0.89
40	0.18	0.06	0.02	0.05	0.10	− 0.05	0.20	0.44	0.45	0.45	0.34	0.50
50	− 0.003	− 0.21	− 0.38	− 0.35	− 0.42	− 0.47	− 0.22	− 0.47	0.02	0.02	− 0.02	0.09
60	− 0.33	− 0.42	− 0.74	− 0.79	− 0.95	− 0.89	− 0.81	− 1.03	− 0.38	− 0.38	− 0.25	− 0.13
70	− 0.82	− 0.85	− 1.06	− 1.21	− 1.38	− 1.34	− 1.46	− 0.88	− 0.68	− 0.68	− 0.40	− 0.14
80	− 1.46	− 1.58	− 1.33	− 1.52	− 1.65	− 1.74	− 1.92	− 0.25	− 1.83	− 1.83	− 0.51	− 0.13
90	− 2.03	− 2.27	− 1.44	− 1.64	− 1.72	− 1.96	− 2.02	0.08	− 0.84	− 0.84	− 0.57	− 0.21
100	− 2.19	− 2.44	− 1.27	− 1.49	− 1.57	− 1.82	− 1.77	− 0.21	− 0.73	− 0.73	− 0.51	− 0.33
110	− 1.89	− 2.00	− 0.84	− 1.09	− 1.20	− 1.32	− 1.29	− 0.75	− 0.56	− 0.56	− 0.35	− 0.32
120	− 1.44	− 1.43	− 0.39	− 0.61	− 0.72	− 0.67	− 0.76	− 0.89	− 0.36	− 0.36	− 0.19	− 0.22
130	− 1.30	− 1.26	− 0.14	− 0.24	− 0.30	− 0.20	− 0.32	− 0.49	− 0.21	− 0.21	− 0.12	− 0.15
140	− 1.55	− 1.53	− 0.14	− 0.11	− 0.08	− 0.04	− 0.05	0.01	− 0.15	− 0.15	− 0.15	− 0.10
150	− 1.77	− 1.75	− 0.22	− 0.14	− 0.06	− 0.8	0.01	0.14	− 0.15	− 0.15	− 0.17	− 0.26
160	− 1.46	− 1.47	− 0.20	− 0.17	− 0.10	− 0.10	− 0.05	− 0.06	− 0.15	− 0.15	− 0.09	− 0.22
170	− 0.59	− 0.80	− 0.11	− 0.09	− 0.07	0.01	− 0.05	− 0.17	− 0.09	− 0.09	0.11	− 0.12
180	0.33	− 0.23	− 0.08	0.05	− 0.04	0.16	0.11	0.02	− 0.03	− 0.03	0.13	− 0.11
190	0.81	− 0.01	− 0.15	0.12	0.12	0.20	0.28	0.25	− 0.04	− 0.04	0.06	− 0.23
200	0.69	0.00	− 0.22	0.09	0.11	0.11	0.18	0.20	− 0.15	− 0.15	− 0.12	− 0.30
210	0.36	0.12	− 0.17	0.01	0.03	− 0.02	− 0.34	− 0.11	− 0.27	− 0.27	− 0.28	− 0.17
220	0.17	0.31	− 0.10	− 0.02	− 0.03	− 0.07	− 1.10	− 0.32	− 0.28	− 0.28	− 0.30	0.10
230	0.15	0.28	− 0.19	− 0.03	− 0.07	− 0.08	− 1.66	− 0.25	− 0.17	− 0.17	1.18	0.23
240	0.06	− 0.14	− 0.53	− 0.14	− 0.18	− 0.18	− 1.75	− 0.12	− 0.07	− 0.07	− 0.05	0.08
250	− 0.23	− 0.70	− 0.96	− 0.44	− 0.45	− 0.44	− 1.50	− 0.30	− 0.12	− 0.12	− 0.03	− 0.18
260	− 0.56	− 1.01	− 1.23	− 0.88	− 0.84	− 0.84	− 1.39	− 0.79	− 0.35	− 0.35	− 0.13	− 0.23
270	− 0.69	− 0.97	− 1.26	− 1.26	− 1.19	− 1.22	− 1.58	− 1.24	− 0.61	− 0.61	− 0.28	− 0.03
280	− 0.62	− 0.82	− 1.16	− 1.42	− 1.36	− 1.43	− 2.09	− 1.35	− 0.73	− 0.73	− 0.36	0.16
290	− 0.55	− 0.77	− 1.06	− 1.31	− 1.30	− 1.38	− 2.50	− 1.17	− 0.66	− 0.66	− 0.32	0.07
300	− 0.58	− 0.74	− 0.93	− 1.00	− 1.05	− 1.07	− 2.49	− 0.93	− 0.44	− 0.44	− 0.19	− 0.26
310	− 0.62	− 0.50	− 0.64	− 0.50	− 0.71	− 0.59	− 2.03	− 0.71	− 0.18	− 0.18	− 0.02	− 0.48
320	− 0.47	0.00	− 0.16	− 0.19	− 0.33	− 0.08	− 1.35	− 0.33	0.11	0.11	0.15	− 0.34
330	− 0.09	0.35	0.36	0.18	0.05	0.31	− 0.67	0.25	0.43	0.43	0.36	0.04
340	− 0.36	0.82	0.70	0.45	0.37	0.53	− 0.08	0.81	0.78	0.78	0.63	0.37
350	− 0.66	0.88	0.82	0.62	0.62	0.61	0.38	1.09	1.09	1.09	0.95	0.51

Membrane Forces in Tower Shell

The variation of the membrane forces along the height of tower at $\phi = 0°$ and $\phi = 67.81°$ meridian has been presented for unsymmetrical wind loading in Figs. 30 and 31 respectively. Figure 30a shows that variation of hoop compressive force along the height of tower at $\phi = 0°$ meridian is identical to the corresponding variation for symmetrical wind loading [21]. The hoop force becomes tensile only at an elevation of about 40.0 m below throat level for all the three cases of interactive analysis (Fig. 30a). The meridional forces have been found to be tensile all along the height of tower at $\phi = 0°$ meridian for unsymmetrical wind loading (Fig. 30b) in all the three cases of interactive analysis. Non-interactive analysis yields values which are less than those due to interaction.

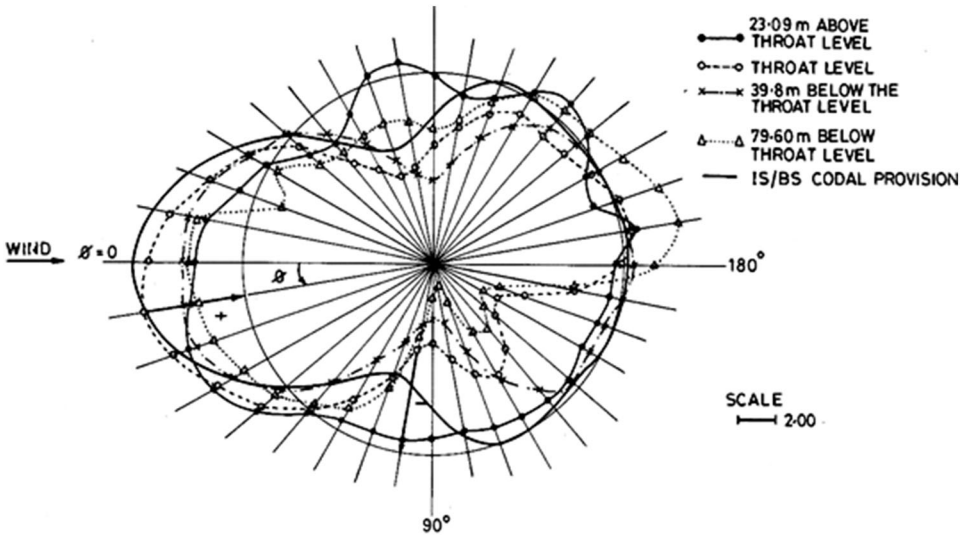

Fig. 28 Typical measured circumferential wind pressure distribution profile (coefficients)

Table 14 Harmonic constants, a_n and b_n for unsymmetrical pressure distribution

Harmonic no.	a_n	Harmonic no.	a_n	Harmonic no.	b_n	Harmonic no.	b_n
0	− 0.0.3561	7	− 0.0385	0	–	7	0.0462
1	0.5763	8	− 0.0080	1	− 0.1167	8	0.0062
2	0.7537	9	0.0002	2	0.4523	9	0.0104
3	0.2865	10	0.0086	3	− 0.0578	10	0.0065
4	0.0623	11	0.0122	4	0.1074	11	− 0.0002
5	− 0.1995	12	0.0056	5	− 0.1336	12	− 0.0110
6	0.1438	13	− 0.0029	6	0.0285	13	− 0.0053

This trend is similar to the corresponding meridional force variation for symmetrical wind loading [21].

Comparison of Fig. 31a with Fig. 30a and Fig. 31b with Fig. 30b shows, in general, a reversal of trend of both hoop and the meridional forces all along the height of tower at $\phi = 67.81°$ meridian as compared to those for 0° meridian. The hoop forces at $\phi = 67.81°$ meridian are tensile all along the height of tower except at the base where these are compressive in nature (Fig. 31a). The meridional forces are compressive all along the height (Fig. 31b). The hoop forces have been found to be independent of the method of analysis. However, the values of meridional forces due to interaction are on the higher side. Comparison of hoop forces for unsymmetrical loading (Fig. 31a) with corresponding hoop forces for symmetrical loading [20] shows that magnitude of tensile hoop forces is larger at 67.81° meridian. Similar comparison for meridional forces along the height of tower (Fig. 31b and [21]) suggests that meridional forces are compressive both at 0° meridian and at 67.81° meridian irrespective of whether the loading is symmetrical or unsymmetrical.

Table 15 Discretization schedule

No. of semi loof shell elements	Tower shell	440
No. of semi loof beam elements	A-frame members	88
No. of plate bending elements	Annular raft	44
No. of 3-D brick elements	Soil mass	792
Total no. of elements		1364
Total no. of nodes		3604
No. of restrained nodes		792
Total no. of equations		13,464

Bending Moments in Tower Shell

The variation of hoop moment, M_ϕ and meridional moment, M_s in the tower shell at $\phi = 0°$ meridian is presented in Fig. 32 along the height the height of tower. Both non-interactive and the interactive analyses produce the same trend of variation of both hoop and the meridional moments all along the height except at the base of the tower, where non-interactive analysis and the SSI: Case-II

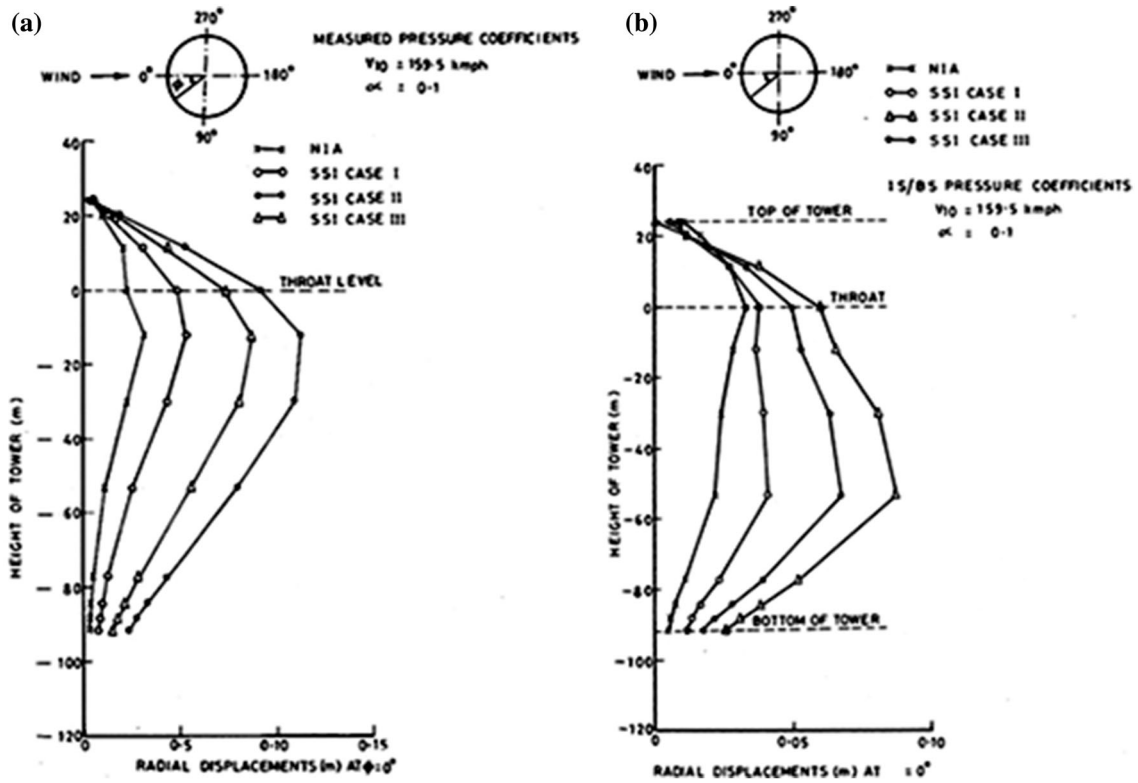

Fig. 29 Variation of radial displacements along 0° meridian for **a** unsymmetrical loading, **b** symmetrical loading

predict hogging hoop moments as against the sagging moments predicted by the other two interactive analyses. Also, highly pronounced values of M_ϕ have been obtained for SSI Case-III as compared to those obtained from non-interactive analysis. The largest value has been predicted in SSI Case-II which is twice the value obtained from NIA. The variation of meridional moment, M_s (Fig. 32b) shows that the values predicted in SSI Case-II are the largest. Study of the variation in values of both hoop moment, M_ϕ and meridional moment, M_s around the circumference of tower at an elevation of 2.58 m below the throat level suggest that their variation follows the wind pressure distribution profile considered in the analysis in the circumferential direction.

Settlement Profile of Annular Raft

The profiles of total settlement and the corresponding differential settlement of the annular raft are shown in Fig. 33 for all the three interactive analyses. Differential settlements have been calculated by normalizing these with respect to the maximum settlement. The maximum value of differential settlement occurs respectively at $\phi = 0°$, 85.91° and 282.30° for the three cases of interaction. Out of the three, the maxima value of differential settlement i.e. 23.55 mm has been obtained at $\phi = 85.91°$ in SSI Case-II.

Contact Pressure Distribution Below Annular Raft

The contact pressure distribution obtained at the base of annular raft (at − 98.632 m elevation) is plotted in Fig. 34. Contact pressure is compressive in the sectors, $\phi = 0°$ to 40°, $\phi = 115°$ to 230° and from $\phi = 310°$ to 360°. Contact pressure becomes tensile between $\phi = 40°$ to 115° and $\phi = 230°$ to 310°. In reality, this tension may not occur if the effect of soil surcharge due to embedment of foundation is taken into account.

Bending Moments in Annular Raft

Study of bending moments, M_x and M_y in the annular raft for values of ϕ ranging from 0° to 360° suggests that the annular raft experiences the maximum values of both the moments in SSI Case-II which represents the weakest strata. Moreover, it has also been observed that absence of a stiff layer at the base of the raft causes a reversal of moment, M_x and this has been validated in the two interactive analyses i.e. SSI Cases-II and III.

Concluding Remarks

1. Unsymmetrical wind pressure distribution represented by Fourier sine–cosine series with 7 harmonic terms

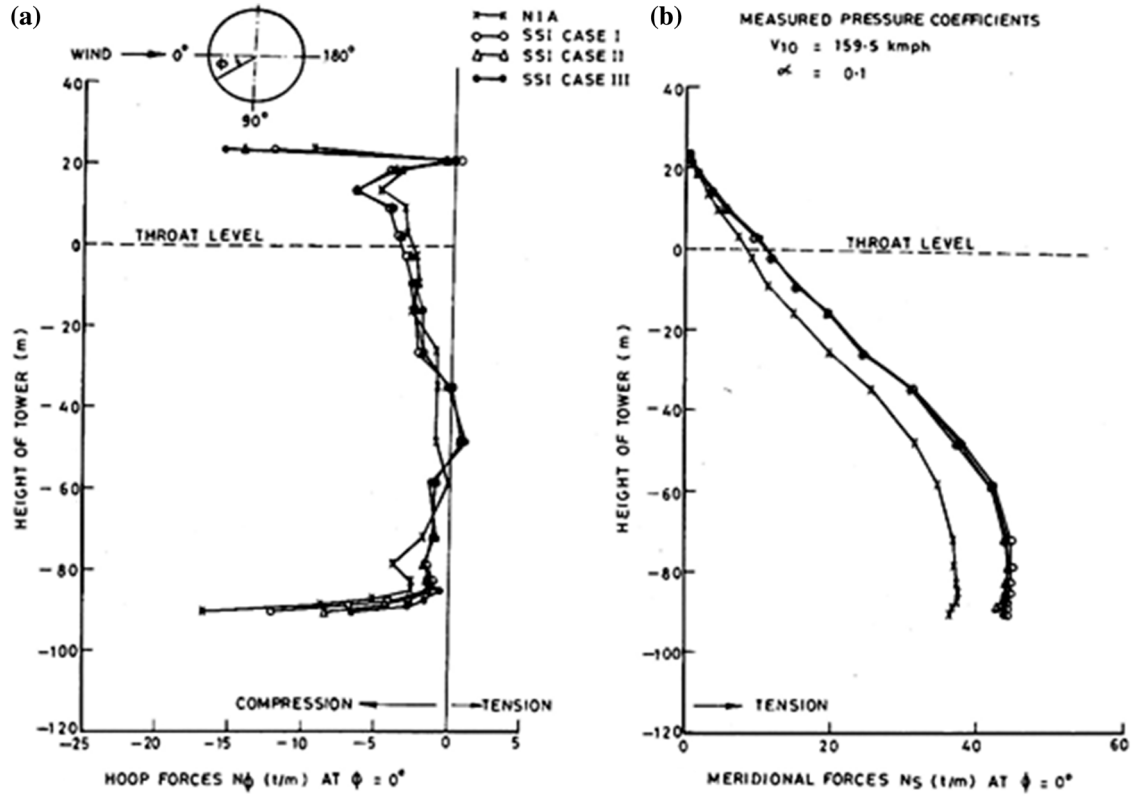

Fig. 30 Variation of membrane forces along 0° meridian unsymmetrical wind loading

gives satisfactory representation of wind loading. In a situation where there is the grouping of towers or presence of other structures in their vicinity, experimental determination of wind pressure in a wind tunnel is a must.

2. It was for the first time that semi-Loof shell and semi-Loof beam elements were successfully used for finite element modelling of cooling tower shell and the supporting A-frames. Semi-Loof shell element has given very encouraging results in situations where both membrane and bending actions dominate the tower response.
3. The proposed three dimensional finite element modelling of tower shell-column supports-annular raft-soil mass system is more realistic and it was for the first time that such a three dimensional interactive analysis of was carried out for the condition of unsymmetrical wind pressure distribution.
4. Unsymmetrical wind pressure distribution causes total alteration in the nature of radial displacements along the height of tower vis-à-vis the symmetrical pressure distribution.
5. Significant redistribution of hoop and meridional forces and moments occurs in the tower shell and the column supports including the reversal in the nature of forces and moments, both due to SSI and the unsymmetrical wind pressure distribution.
6. The annular raft even with a thickness of 5.0 m behaves as a flexible foundation and experiences maximum differential settlement of 14.57 mm at $\phi = 73.64°$ in case of symmetrical wind pressure distribution and 23.55 mm at $\phi = 85.91°$ for the unsymmetrical pressure distribution.

Case study of HRT of Kishanganga Hydro Power Project

Introduction

The project, which was undertaken in the state of Jammu and Kashmir, and is still a matter of discussion and controversy, envisages the construction of a 37 m high concrete face rock fill dam across the river Kishanganga along with a spillway, a diversion tunnel, an intake structure and an adit to head race tunnel (HRT) in the Gurez valley. It also involves construction of a 24 km long head race tunnel, a surge shaft, and 3 × 110 MW turbine-generators installed in an underground power house complex at the Bandipora end of the project. After generating the power,

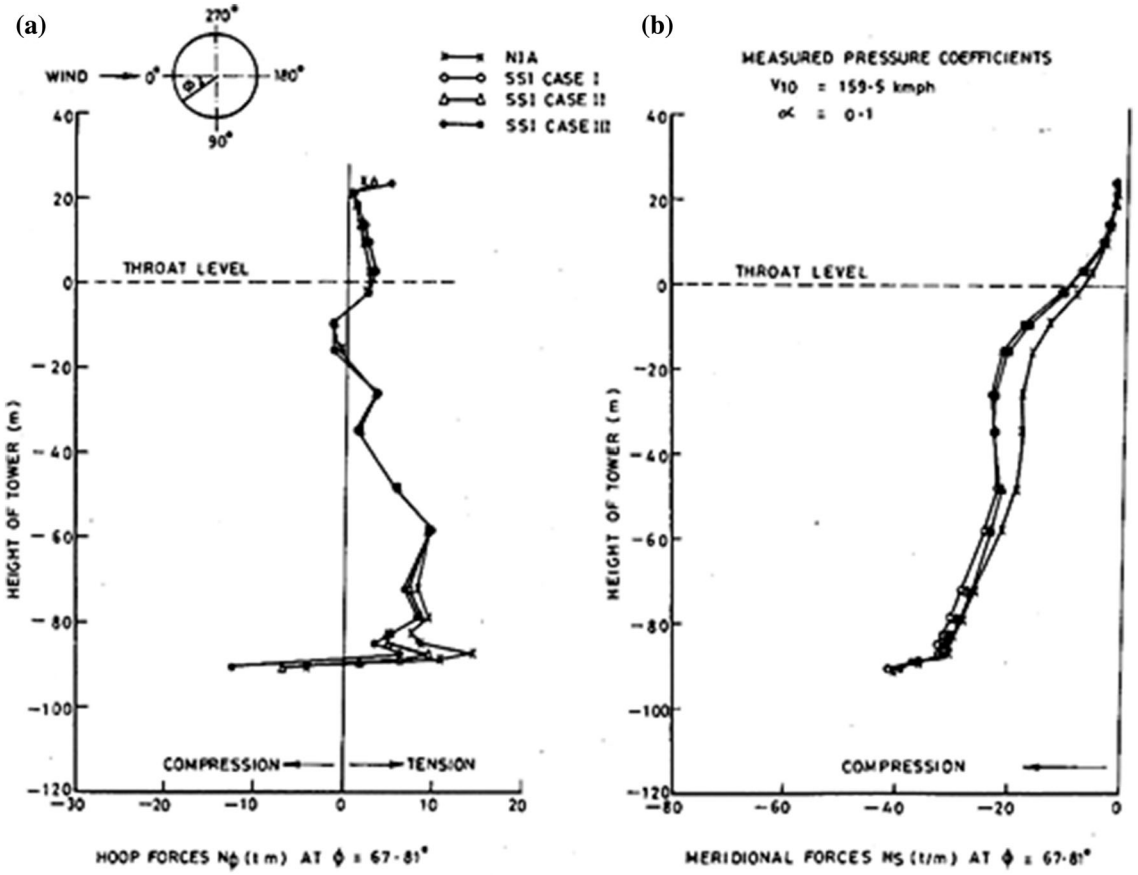

Fig. 31 Variation of membrane forces along 67.81° meridian for unsymmetrical wind loading

water is discharged through a tail race channel (TRT) into Wular Lake. The drop in elevation from the dam to the underground power house generates a hydraulic head of 697 m (2287 ft). Figure 35 shows the topographic map of the project area [36]. It was proposed to construct the HRT using TBM technology. However, in view of the complex nature of Himalayan geology, it was not known whether the TBM technology would be successful or not. The TBM shield was designed to withstand a maximum pressure of 1 MPa. In view of the 24 km length of HRT which was to pass through many geological formations [36], it was essential—(1) to identify the geological conditions all along the stretch of HRT, (2) to identify ground conditions which would be encountered—(a) during excavation of the HRT using TBM, and (b) the influence of ground conditions on the permanent lining or the support system, and (3) to ensure that pressure of the TBM shield does not exceed 1 MPa.

Geomorphology of Project Area

The project, being a run-off the river scheme, tames the run-off water of Kishanganga river and diverts it through a 24 km long power tunnel to an underground powerhouse located near Bandipora. The Kishanganga river, which flows roughly from east towards west in the dam site area and further down, takes a northwesterly turn. But the diverted water is conducted through HRT towards S-SW and hence away from the main river. The HRT follows a NE–SW trending ridge (Fig. 36), being mainly located on the northwestern slope of the ridge. The ridge is highly rugged in nature and is dissected by a number of streams on the northwestern and southeastern sides. Many of these streams are deep and U-shaped in nature due to movement of glacial ice along the courses. On this slope, a number of northwesterly flowing streams join a fairly big stream flowing towards northeast and ultimately joining the Kishanganga River. The elevations on this ridge range from 2800 m to about 4000 m, with fairly steep slopes. The rock cover over HRT, which varies very widely, is maximum on the southern side of the tunnel. The southern nose of this ridge has moderate slopes, where the powerhouse is located underground within the Panjal volcanics.

Geological Settling of HRT

The HRT is located in the northwestern part of the Kashmir Himalaya, where meta-sedimentary rocks are

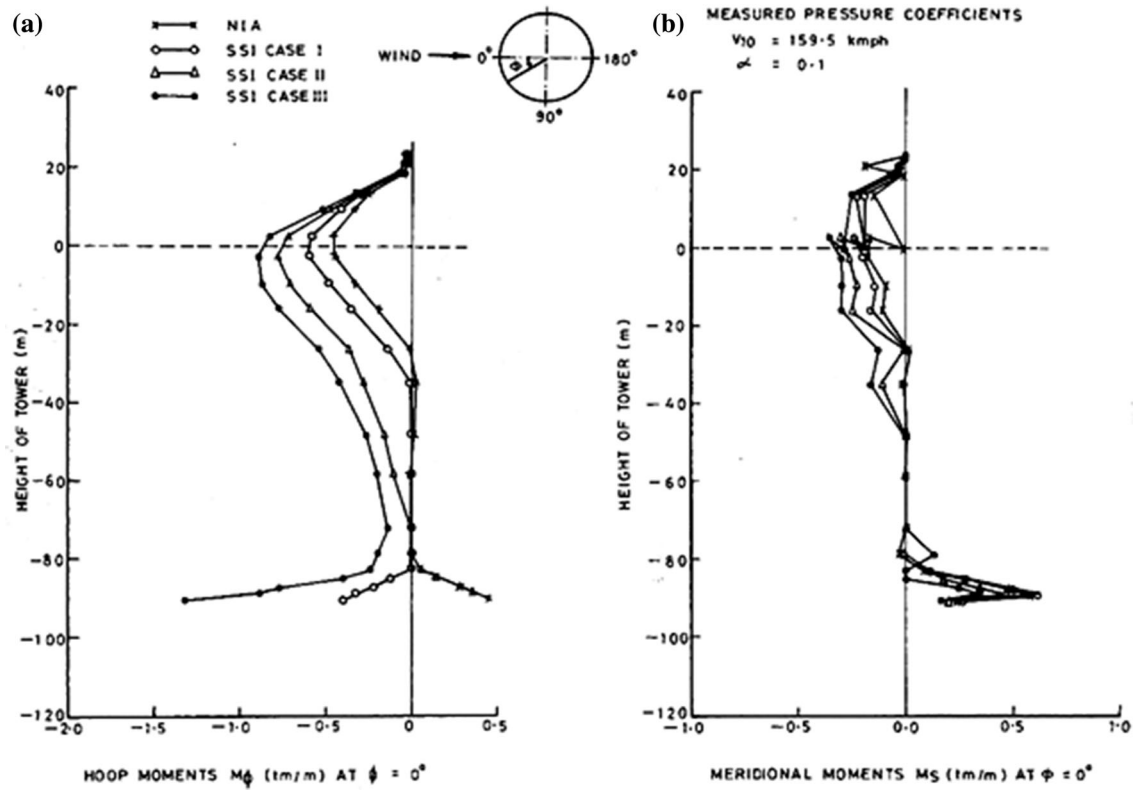

Fig. 32 Variation of bending moments along 0° meridian in tower shell

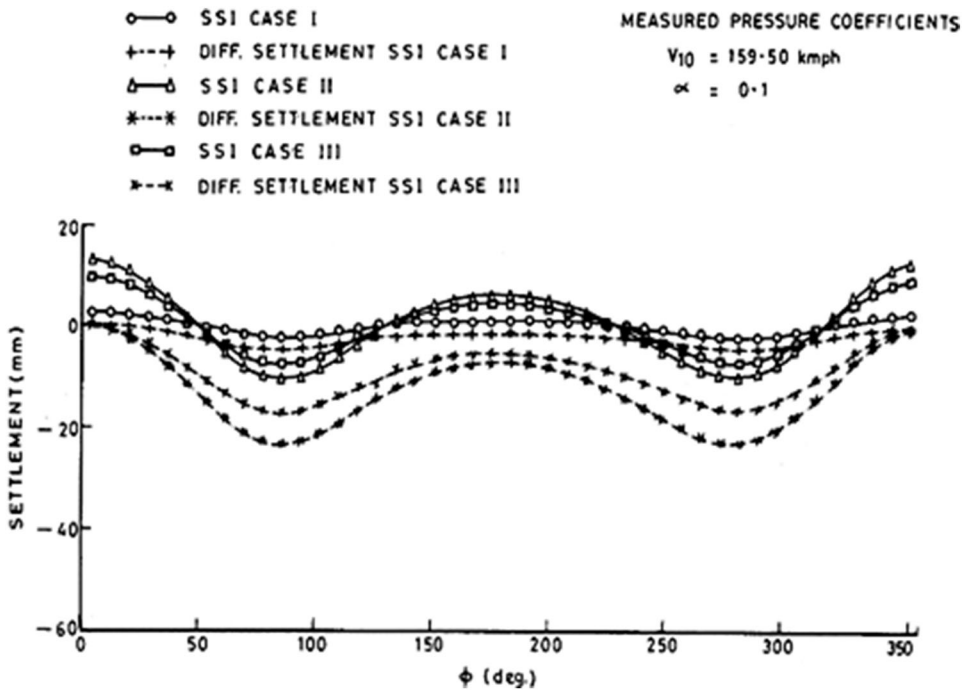

Fig. 33 Settlement profile along the centre line of the annular raft

dominantly located in association with Panjal volcanics and Grano-diorite intrusive. The HRT traverses roughly perpendicular to the general trend of the rock contacts. While the tunnel passes from north to south (Fig. 36), the general contacts are aligned in east–west direction. From south (the powerhouse end) towards north (the dam site end), various geological Formations encountered are (Fig. 36).

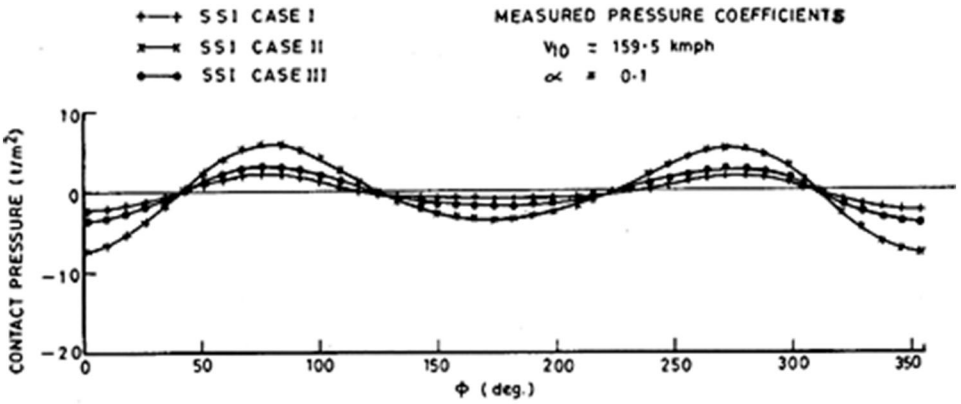

Fig. 34 Contact pressure distribution below the annular raft at − 98.632 m elevation

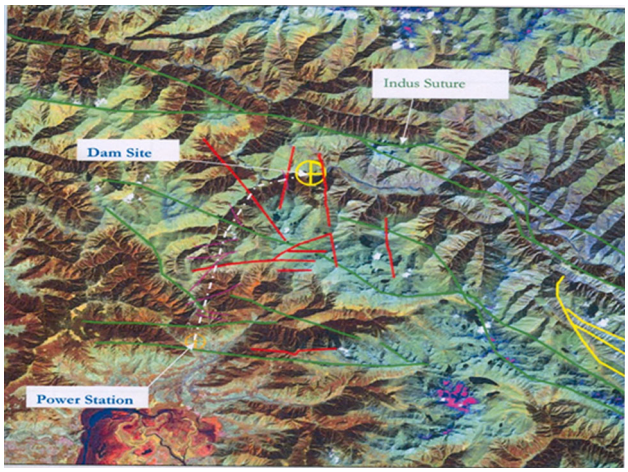

Fig. 35 Topographic map of project area, KGHEP, J&K [36]

Panjal Volcanics

Panjal volcanics is a basic rock representing the lava flow close to the surface. The rocks were subsequently metamorphosed, and hence called as meta-volcanics (Fig. 37). These rocks, being more prone to weathering, are more weathered close to the surface. The rocks are grayish, greenish and grayish blue colored, fine grained, hard to very hard and jointed to massive in nature. The rocks, which are vesicular in nature, show well developed foliations and are exposed at both the ends of tunnel close to the portal area.

The geological discontinuities observed in these rocks were found to have resultant attitudes as follows:

Foliation, F	Strike—N60°E	Dip—45°/towards N150°	
Joint, J1	Strike—N80°	Dip—70°/towards N350°	Spacing 30–50 cm
Joint, J2	Strike—N90°	Dip—20°/towards N180°	Spacing > 70 cm
Joint, J3	Strike—N140°	Dip—70°/towards N50°	Spacing 30–50 cm

Most of the joint surfaces are rough and undulating in nature. Most of the joints are persistent along the strike continuity. Though the rocks are weathered close to the surface, they are likely to be fresh and in excellent condition at the tunnel grade. Since the HRT portals on either side are located in this rock, they may render stability to the proposed portal structures. A visual estimation of RQD from the exposed rocks as well as the core boxes indicates values of 70–90%. The average RMR for the fairly fresh rocks is of the order of 60–80%. These values are likely to show improvement at depth at the tunnel grade.

Meta-siltstones

The HRT from the dam site end passes through dominantly meta-siltstone formations of different types. This zone extends for a considerable length of more than 18 km till the Panjal volcanics are encountered again on the southern end near the power house. The meta siltstones belong to Razdhan Formation, Hasthoji Formation, Halfkhalan Formation and the Tragbal Formation. Even though different geological Formations are present, the rock types are basically siltstones. The rocks are dark colored, basically grayish with different tinge of green and blue colors, hard, compact and well jointed and also show foliations which are generally parallel to the bedding. The rocks are also traversed by crisscross quartz veins within the rocks.

(a) Phyllite intercalated siltstones

After the volcanics, a zone of phyllite-dominated rocks was seen in the area. The typical characteristic of the phyllite, namely micaceous sheen, could be seen on the foliation

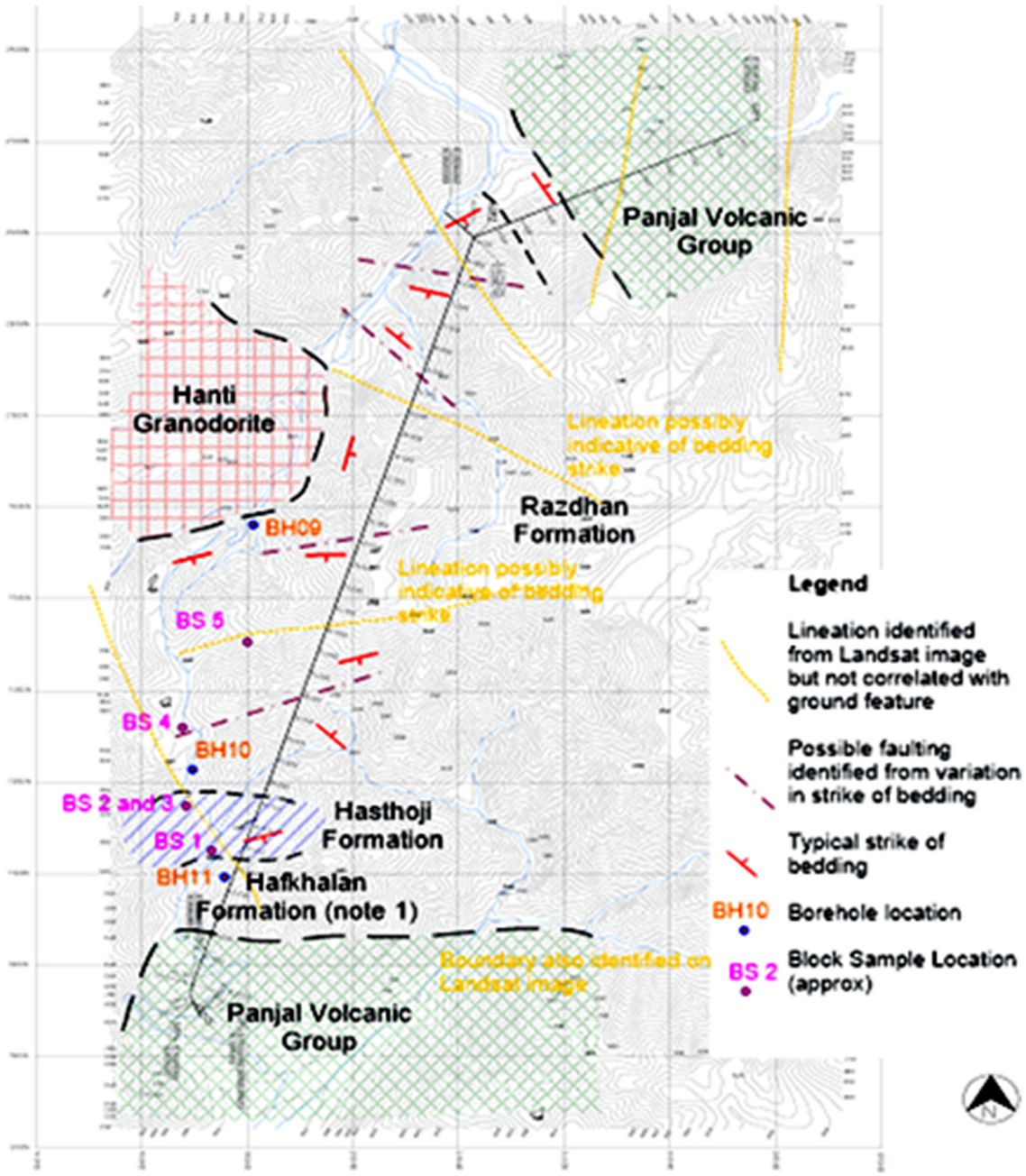

Fig. 36 Alignment of HRT along various geological formations [36]

surfaces. The phyllites, namely, phyllitic-quartzites and the quartzitic-phyllites are seen intercalated with meta siltstones. The rocks show well developed foliations and are well jointed. These rocks show well puckers and are tightly folded at places. The following geological discontinuities were observed in phyllite dominated area:

Foliation, F	Strike—N130°E	Dip—65–70°/towards N40°	
Bedding, B	Strike—N10°	Dip—15-20°/towards N180°	
Joint, J1	Strike—N300°	Dip—75°/towards N210°	Spacing > 20 cm
Joint, J2	Strike—N55°	Dip—45°/towards N325°	Spacing > 50 cm

As these rocks are exposed close to granodiorite, rocks are hard and well lithified with RQD possibly more than

Fig. 37 Panjal volcanics exposed at diversion tunnel outlet

80%. The joints are generally rough and undulating in nature.

Other meta-siltstones belonging to Razdhan and other Formations were broadly grouped into three categories: (1) moderately massive, (2) well jointed rocks and (3) thinly bedded rocks. This categorization is primarily based on the physical character.

(b) Moderately massive siltstone

These rocks are generally massive showing foliations and fairly wide joints which are rough and undulating in nature and show several crisscross quartz veins in between. The beddings are generally less developed as compared to foliations, but the foliations show merging effects along the strike continuity indicating effective bridges between the foliations. These rocks show RQD values ranging between 60–80% and RMR between 50–70 and even more at places. At tunnel grade, these values were expected to improve considerably. These rocks may constitute about 50–70% of the total rock mass of siltstone.

(c) Well jointed rocks

These siltstone rocks show similar type of foliations, but with more closely spaced joints. The RQD ranges from 40 to 60% with an average RMR of about 50. These rocks constitute about 20–40% of the total rock mass constituting the siltstone.

(d) Thinly bedded siltstone

Here, the bedding essentially remains parallel to the foliations. The bedding shows very less spacing of less than 50 mm. The joints are less developed as compared to the foliations. Even the joints seen in the area have less strike continuity. However, because of closely spaced beddings, they show very low RQD ranging between 20 and 40% with RMR values less than 40. However, these rocks are exposed in isolated stretches of short distance. Hence, they constitute about 10–20% of the total rock mass constituting the siltstone.

(e) General

Though the entire meta siltstone reach has been clubbed into one unit for the purpose of tunneling, geologically these rocks have been divided into different Formations. However, there are no sharp contacts between the Formations and hence can be called graded contacts. Due to the fact that siltstone is the dominant rock unit in all these Formations, these units are not distinctly identifiable. However, some of the important observable features on the ground are discussed below:

The Tragbal formation (Fig. 38) is generally dark grey to greenish grey colored with dominantly siltstone rocks. Because of their proximity to volcanics, the rocks are hardened and well lithified. This unit also has a number of crisscross quartz veins. The Halfkhalan formation (Fig. 39) also has meta siltstone as a dominant unit. The rocks are grey to dirty grey colored and highly weathered at the surface. The rocks are dense and massive at places. The rock quality may improve greatly with depth as weathering will not be present at deeper levels. The Hasthoji Formation (Fig. 40), which is sandwitched between Razdhan and Halfkhalan Formations, consists of dirty grey colored meta siltstones. Foliations are well developed and at places, thinly foliated. The beds show good color banding to indicate the bedding planes. The foliation and the beddings are nearly parallel in this stretch. The Razdhan Formation (Fig. 41) occupies major part of the siltstone stretch. Rocks are generally hard and massive even at the surface at many places.

Rocks are well lithified in most areas excepting in short stretches where it looks to be weak. Foliations, in general, are less developed. The bedding planes indicate ripple marks at many places. The color banding is well developed to indicate the bedding planes. The drill holes at relatively shallower depths of 80–100 m indicate very good core recovery with RQD ranging between 70 and 90%. Since these drill holes are shallow and close to the surface, at deeper levels of tunnel grade, RQD and the rock quality may improve significantly.

Granodiorite (Fig. 36)

It is an intrusive body penetrating within the siltstones, but not present along the proposed alignment on the surface. The contact of granodiorite with siltstone is present at least more than a kilometer on the western side of the alignment. The contact is generally concealed below the debris/alluvial soil. The contact of the northern and southern sides is concealed under the debris while on the other hand; the eastern contact is concealed below the stream bed flowing on the eastern side of granodiorite intrusion. Though this rock is exposed about a kilometer away on the surface, its depth-wise extension intercepting the tunnel alignment cannot be ruled out.

Prediction of Ground Condition during Tunnelling

The knowledge of ground condition plays an important role in the selection of the method of excavation and design of the support system for underground excavations. Experience suggests that tunneling through the squeezing ground condition is quite problematic and is a very slow process because the rock mass surrounding the excavations loses its inherent strength under the influence of in situ stresses. This may result in mobilization of high support pressure and tunnel closures. Tunneling in non-squeezing ground condition, on the other hand, is relatively safe and easy because the inherent strength of rock mass is not affected. Therefore, the primary step is to assess whether a tunnel, during excavation, would experience a squeezing ground condition or a non-squeezing ground condition. This decision governs the choice of the method of excavation and the supporting system. In the Indian context, squeezing ground conditions are quite common in the Lower Himalaya where the rock masses are weak, highly jointed, faulted, folded, fractured and tectonically disturbed and the overburden could also be quite high.

Phenomenon of squeezing is primarily dependent on four factors including size of excavation, B (m); depth of overburden, H (m); magnitude of in situ stresses; and rock mass quality, Q. Due to uncertainty in prediction of stress reduction factor, rock mass quality was replaced by rock mass number, N. Using this rock mass number, Goel [37], Goel et al. [38], Goel [39] and Singh and Goel [40] analyzed about 99 case studies of tunneling covering a wide variety of ground conditions varying from highly jointed and fractured rock masses to massive rock masses. It was also realized that the degree of squeezing can very well be represented by tunnel closure as: (a) mild squeezing- closure 1–3% of tunnel diameter; (b) moderate squeezing-closure 3–5% of tunnel diameter; and (c) High squeezing-closure $>$ 5% of tunnel diameter. Various ground conditions for tunneling were defined based on criteria presented in Table 16 given below. In addition to these criteria, an additional criterion that should be satisfied is regarding the ratio of the joint roughness number, J_r in relation to joint alteration number, J_a, which for the case of mild and moderate squeezing should be less than 0.5 and for the case of high squeezing, it should be less than 0.25. If the ratio, J_r/J_a exceeds 0.5, then there occurs a possibility of a mild rock burst. Computations were performed for predicting various ground conditions through which HRT was to be driven. These computations are presented in Table 17 for various chainages all along the length of HRT passing through different geological formations for a typical value of J_r/J_a less than 0.25. Table 17 suggests that high squeezing conditions can be expected during tunnelling in Hasthoji and Hafkhalan Formations whereas moderate squeezing can be expected in Razdhan formation between 10 to 12 and between 12.5 to 14.5 km. Mild squeezing can as well be expected in Razdhan formation from 6.5 to 7.5 km and at few more locations.

Fig. 38 Highly weathered meta-siltstones of Tragbal Formation, moderately massive and well foliated at places

Fig. 39 Meta-siltstones of Halfkhalan formation showing excessive weathering close to surface

Fig. 40 Thinly foliated meta siltstones of Hasthoji Formation showing high weathering close to surface

Fig. 41 Moderately massive siltstones rocks of Razdhan Formation

Geological and Material Characteristics Along HRT

Study of rock cores extracted during drilling and close observations of rock mass characteristics (number of joint sets, their dip and dip direction, spacing and condition of joint surfaces etc.) in the field helped in estimating the values of Bieniawski's RMR [41]. An attempt was also made to obtain the values of Geological Strength Index (*GSI*) using the approach presented by Hoek and Marinos [42]. The values of uni-axial compressive strength (UCS) and Hoek and Brown parameter, m_i of intact rock cores obtained for rock types in different geological formations were adopted from Palmer [43]. The values of Hoek and Brown parameters, m_r and S_r were obtained using the expressions:

$$m_r = m_i \cdot e^{\frac{RMR-100}{14}} \tag{25a}$$

$$S_r = e^{\frac{RMR-100}{6}} \tag{25b}$$

Similarly, values of UCS and modulus of deformation of jointed rock mass, $E_{d,mass}$ were calculated using the values of UCS and Hoek and Brown parameter, m_i of intact rock cores and also the GSI. The expressions used were given by Hoek and Brown [44] and Hoek and Marinos [42], which are as follows:

$$\sigma_{c,mass}(MPa) = \left(0.0034 \cdot m_i^{0.8}\right) \cdot \sigma_{ci} \cdot \left(1.029 + 0.025 \cdot e^{-0.1 \cdot m_i}\right)^{GSI} \tag{26}$$

$$E_{d,mass}\,(GPa) = \sqrt{\frac{\sigma_{ci}}{100}} \cdot 10^{\frac{GSI-10}{40}} \tag{27}$$

The values of all these parameters obtained for different geological formations through which the HRT was driven, are presented in Table 18 at different chainages along the length of HRT.

Computation of In Situ Stresses

In the absence of any data from hydro fracture tests, resort was taken to Palmer [45] for in situ stress estimates on basis of the review of the existing literature. Accordingly, the in-situ vertical stress has been computed as:

$$\sigma_v = \gamma \cdot H \tag{28a}$$

and

$$\sigma_h = 2.0 \cdot \sigma_v, \text{ for depth of overburden, } H \leq 600 \text{ m} \tag{28b}$$

$$= 0.5 \cdot \sigma_v, \text{for depth of overburden, } H > 600 \text{ m} \tag{28c}$$

In-situ stresses were therefore computed in various geological formations all along the stretch of HRT using Eq. (28a, b, c) and have been presented in Table 19. Table 19 also provides average values of the in-situ stresses at different chainages and these average values were used in subsequent computations as the hydrostatic stress acting at respective chainages.

Table 16 Prediction of ground condition using rock mass number, *N* [38, 40]

S. no.	Ground conditions	Correlations for predicting ground condition
1	Self-supporting	$H < 23.4\ N^{0.88} \cdot B^{-0.1}$ and $1000\ B^{-0.1}$ and $B < 2\ Q^{0.4}$
2	Non-squeezing	$23.4\ N^{0.88} \cdot B^{-0.1} < H < 275\ N^{0.33} \cdot B^{-0.1}$
3	Mild squeezing	$275\ N^{0.33} \cdot B^{-0.1} < H < 450\ N^{0.33} \cdot B^{-0.1}$ and $J_r/J_a < 0.5$
4	Moderate squeezing	$450\ N^{0.33} \cdot B^{-0.1} < H < 630\ N^{0.33} \cdot B^{-0.1}$ and $J_r/J_a < 0.5$
5	High squeezing	$H > 630\ N^{0.33} \cdot B^{-0.1}$ and $J_r/J_a < 0.25$

Prediction of Squeezing Potential for Excavation of HRT (in Absence of Supports)

Hoek [46] published details of analysis which showed that the ratio of uni-axial compressive strength, $\sigma_{c,mass}$ of rock mass to in-situ stress, p_o can be used as an indicator of potential tunnel squeezing problems. Following the suggestions of Sakurai [47], an analysis was carried out to determine the relationship between (σ_{cm}/p_o) on one hand and the percentage strain in the tunnel on the other. This percentage tunnel closure, ε is defined as,

$$e = (\text{tunnel closure} \ / \ \text{tunnel diameter}) \times 100 \tag{29}$$

This analysis by Hoek [46] can be extended to cover tunnels in which internal pressure is used to simulate the effect of support systems. Following equations were presented for predicting:

(1) size of the plastic zone (extent of the broken rock mass) developed around the periphery of the tunnel, and (2) deformation of tunnel in squeezing ground:

$$\frac{d_p}{d_o} = \left[1.25 - 0.625\,\frac{p_i}{p_O}\right]\left(\frac{\sigma_{cm}}{p_o}\right)^{\left(\frac{p_i}{p_o}-0.57\right)} \tag{30}$$

$$\frac{\delta_i}{d_o} = \left[0.002 - 0.0025\,\frac{p_i}{p_O}\right]\left(\frac{\sigma_{cm}}{p_o}\right)^{\left(2.4\frac{p_i}{p_o}-2\right)} \tag{31}$$

where, d_p is the diameter of plastic zone; p_i, the internal support pressure; d_o, the original tunnel diameter (m); p_o, the in-situ stress; δ_i, the tunnel sidewall deformation and σ_{cm}, represents the rock mass strength. However, the most critical condition occurs during construction in absence of any support system, i.e., when internal pressure, p_i is zero. In subsequent calculations therefore, value of p_i has been taken as zero. Using Eqs. (30) and (31), computations were done for predicting: (1) tunnel closure, (2) radius of plastic zone, developed around the periphery of the excavated tunnel, and (3) squeezing potential of rock mass surrounding the tunnel. These computations make use of Table 20 for deciding the degree of squeezing.

A summary of all these computations has been presented in Table 21. It may be noted that no squeezing is anticipated in HRT stretch passing through Panjal Volcanics towards the dam end or Panjal Volcanics and the Tragbal Formation towards the power house end. It also suggests that very high squeezing can occur in Hasthoji and Hafkhalan formations whereas moderate squeezing can occur between 10 to 11, and 13.5 to 14.5 km in Razdhan Formation, especially, in siltstone with bands of phyllites.

Prediction of Stand-Up Time

Verman [48] and Viladkar et al. [49, 50] obtained the expressions for stand-up time on basis of the regression analysis of Bieniawski's [51] data for underground openings with arch roof. Accordingly, the correlation developed for stand-up time, t_{arch} (h) is given by:

$$t_{arch} = 10^{\frac{RMR-20}{15}} \cdot B^{-(0.004\,H-0.21)} \tag{32}$$

It may be seen from Eq. (32) that stand-up time reduces with increase in size of opening. Further, the size effect depends upon the height of the overburden. The size effect is more pronounced in deeper openings than those located at shallow depths. Using Eq. (32), stand-up time has been calculated for the HRT. These computations are presented in Table 22 for different geological formations all along the stretch of the HRT. Table 22 also gives corresponding values of stand-up time from Bieniawski's [51] chart for the purpose. A close look at this table suggests that Bieniawski [50] approach predicts very high values of the stand-up time. For a typical size of the HRT (6.3 m), it has been found that the stand-up time significantly varies with depth of overburden. It can be seen that in Panjal Volcanics (meta basics), the stand-up time decreases from 11.77 months for an overburden of 75 m to as low as 1.53 weeks when the depth of overburden increases to 550 m. Similarly, in the Tragbal Formation (meta siltstones), the stand-up time reduces from 6.45 to 2.14 weeks as the depth of overburden increases from 250 to 400 m. In Razdhan Formation (Quartzitic Phyllites, Granite and Siltstones with bands of Phyllites), the stand-up time is as low as few hours. In Hasthoji and Halfkhalan Formations, the stand-up time is awfully low, as low as 0.01 h.

These computations therefore suggest that at all those stretches of HRT wherever the stand-up time is less than 36 h (the time required for installation of concrete liners and pumping in the p-gravel in the space between the liners and the excavated periphery), it is essential to undertake rigorously the pre-excavation grouting of rock mass ahead of the tunnel face.

Prediction for Possible Rock Burst

Rock burst is a phenomenon which involves instantaneous release of strain energy already stored in the rock mass and the event can be catastrophic if the energy is released in an un-controlled manner. Kumar [52] classified the mode of failures according to the values of joint roughness number, J_r and the joint alteration number, J_a. Accordingly, the possibility of rock burst exists when the ratio of maximum tangential stress, σ_θ at the periphery of tunnel to the bi-axial compressive strength of rock mass, i.e. ($\sigma_{\theta,max}/q'_{c,mass}$) lies in the range of 0.6–1.0. For the sake of simplification, in situ stress field has been assumed as hydrostatic (Table 19). The maximum tangential stress concentration

Table 17 Prediction of ground condition based on rock mass number (N) criterion during tunneling along HRT alignment ($J_r/J_a < 0.25$) Ch. 0 km at Dam axis; $RMR = 9.\ln(Q) + 44$; $SRF = 2.5$

Ch. (km)	Geological formation	Rock types	H (m)	RMR	Q_{lower}	$N_{lower} = Q.\ SRF$	Ground condition
0	Panjal	Meta basics	75	80	54.60	136.50	SSP
0.5	Volcanics		300	80	54.60	136.50	SSP
1			550	80	54.60	136.50	SSP
1.5			550	80	54.60	136.50	SSP
2			400	80	54.60	136.50	SSP
2.5	Razdhan	Phyllitic quartzite	400	60	5.92	14.79	NSQ
3			400	60	5.92	14.79	NSQ
3.5			400	60	5.92	14.79	NSQ
4			350	60	5.92	14.79	NSQ
4.5			350	60	5.92	14.79	NSQ
5			350	60	5.92	14.79	NSQ
5.5			550	60	5.92	14.79	NSQ
6			400	60	5.92	14.79	NSQ
6.5		Quartzitic phyllite	675	60	5.92	14.79	MSQ
7			800	60	5.92	14.79	MSQ
7.5			650	60	5.92	14.79	MSQ
8			475	60	5.92	14.79	NSQ
8.5			450	60	5.92	14.79	NSQ
9			550	60	5.92	14.79	NSQ
9.5		Granite	700	60	5.92	14.79	MSQ
10			1000	60	5.92	14.79	MODSQ
10.5			1150	60	5.92	14.79	MODSQ
11			1050	60	5.92	14.79	MODSQ
11.5			1200	60	5.92	14.79	MODSQ
12			1225	60	5.92	14.79	MODSQ
12.5		Siltstone with bands of phyllite	1400	60	5.92	14.79	HISQ
13			1300	60	5.92	14.79	HISQ
13.5			1100	60	5.92	14.79	MODSQ
14			1100	60	5.92	14.79	MODSQ
14.5			1000	60	5.92	14.79	MODSQ
15			800	60	5.92	14.79	MSQ
15.5			550	60	5.92	14.79	NSQ
16			425	60	5.92	14.79	NSQ
16.5			600	60	5.92	14.79	MSQ
17			450	60	5.92	14.79	NSQ
17.5			350	60	5.92	14.79	NSQ
18			650	60	5.92	14.79	MSQ
18.5	Hasthoji	Meta siltstone (70%) + phyllite (30%)	850	30	0.21	0.53	HISQ
19			925	30	0.21	0.53	HISQ
19.5	Hafkhalan	Thinly bedded meta siltstone	650	40	0.64	0.53	HISQ
20			450	40	0.64	1.60	MODSQ
20.5	Tragbal	Meta siltstone	400	75	31.33	78.31	SSP
21			250	75	31.33	78.31	SSP
21.5			350	75	31.33	78.31	SSP
22	Panjal Volcanics	Meta basics	450	80	54.60	136.50	SSP
22.5			350	80	54.60	136.50	SSP
23.067			50	80	54.60	136.50	SSP

SSP self-supporting, *NSQ* non-squeezing, *MSQ* mild squeezing, *MODSQ* moderate squeezing, *HISQ* high squeezing, *VHISQ* very high squeezing, *MRB* mild rock burst

Table 18 Section wise geological and mechanical properties along HRT

S. no.	Ch. (km)	Geology	*RQD*	*RMR*	*GSI*	UCS (MPa)	m_i	m_r	S_r	$\sigma_{c,mass}$ (MPa)	$E_{d,mass}$ (GPa)
1	21.40–23.10	Panjal Volcanics (meta basics)	80–90	80	75	160	20	4.793	0.0357	65.238	53.341
2	2.70–18.50	Razdhan (meta Siltstone)	70–90	60	55	50	10	1.173	0.0067	9.273	9.890
3	18.50–19.70	Hasthoji (meta Siltstone)	30–50	30	25	35	06	0.0578	0.00002	1.42	1.403
4	19.70–20.80	Hafkhalan (thinly bedded meta siltstone)	40–70	40	30	40	07	0.197	0.00024	2.18	2.00
5	20.80–21.40	Tragbal (meta siltstone)	80–90	75	70	100	13	2.180	0.0155	31.07	31.623
6	21.40–23.07	Panjal Volcanics	80–90	80	75	160	20	4.793	0.037	65.24	53.341

has therefore been considered as two times the hydrostatic stress as,

$$\sigma_{\theta,\max} = 2 \cdot \sigma_v = 2 \cdot \gamma \cdot H \tag{33}$$

The bi-axial compressive strength of rock mass was obtained by using the approach given by Singh and Goel [40].

According to rock mass classification system proposed by Barton et al. [53], the value of J_r, on basis of the nature of joint surfaces observed from surface exposures, wherever possible, along the stretch of HRT, was assigned as 3.0 for the case of rough or irregular and undulating rock joints and the value of J_a, for the case of slightly altered joint walls with non-softening mineral coatings, sandy particles and clay free disintegrated rock etc., was assigned as 2.0. The ratio J_r/J_a, therefore works out to be 1.5. However, at the tunnel grade level, it was anticipated that small faults as well as shear zones would intersect the tunnel cross-section and therefore the value of J_r/J_a would be a reduced value. Attempt was therefore made to explore the possibility of occurrence of rock burst during excavation all along the stretch of HRT at different chainages and geological formations. These computations are presented in Table 23 for the ratio $J_r/J_a = 1.5$ as stated above. It was found that possibility of mild rock burst (MRB) exists only in Razdhan formation and that too only where the rock type is either granite or siltstone with bands of phyllites, in the stretch between chainage 10.0 and 15.0 km (Granite/Siltstone with bands of Phyllite). But for this stretch, tunneling will be quite safe. It was therefore suggested that pre-excavation drilling be undertaken in the face of advance during tunneling in the stretch from 10 km–15 km. These drill holes should be charged and detonated in the form of controlled mild blasts. Such a process introduces fractures in rock mass surrounding the tunnel, thereby releasing the strain energy stored in the rock mass and mitigating the possibility of any rock burst.

Prediction of Tunnel Closure and Support Pressure After Installation of Combined Support System

Sequence of Support Installation

As per the sequence of construction decided, concrete liners were to be installed within 8 h after the excavation of tunnel. As the diameter of excavated tunnel is usually more than the finished diameter, there would be a gap between concrete liners and the excavated periphery and hence there will be no transfer of surrounding rock pressure to the concrete liners unless a contact between the two is established. The concrete liners would therefore come into action only after this gap between the liners and the excavated periphery is filled up with the help of p-gravels within 28 h after installation of concrete liners. It was therefore proposed to carry out primary grouting of p-gravels within 6 h after the p-gravels were placed in position. In order to reduce the convergence of rock mass surrounding the supported HRT, it was also proposed to undertake secondary radial grouting of rock mass which was to be completed within 20 days after the primary grouting.

Computation of Support Stiffness

The stiffness of segmental concrete liners was evaluated by using the expression given by Hoek and Brown [44] as

Table 19 Computation of in situ stresses

Ch. (km)	Geological Formation	Rock type	H (m)	γ (t/m^3)	Vertical in situ stress, σ_v (MPa)	Horizontal in situ stress, σ_h (MPa)	Average in situ stress, p_o (MPa)
0	Panjal	Meta basics	75	2.5	1.875	3.75	2.8125
0.5	Volcanics		300	2.5	7.5	15	11.25
1			550	2.5	13.75	27.5	20.625
1.5			550	2.5	13.75	27.5	20.625
2			400	2.5	10	20	15
2.5	Razdhan	Phyllitic quartzite	400	2.3	9.2	18.4	13.8
3			400	2.3	9.2	18.4	13.8
3.5			400	2.3	9.2	18.4	13.8
4			350	2.3	8.05	16.1	12.075
4.5			350	2.3	8.05	16.1	12.075
5			350	2.3	8.05	16.1	12.075
5.5			550	2.3	12.65	25.3	18.975
6			400	2.3	9.2	18.4	13.8
6.5		Quartzitic phyllite	675	2.3	15.525	7.763	11.64375
7			800	2.3	18.4	9.2	13.8
7.5			650	2.3	14.95	7.475	11.2125
8			475	2.3	10.925	21.85	16.3875
8.5			450	2.3	10.35	20.7	15.525
9			550	2.3	12.65	25.3	18.975
9.5		Granite	700	2.3	16.1	8.05	12.075
10			1000	2.3	23	11.5	17.25
10.5			1150	2.3	26.45	13.225	19.8375
11			1050	2.3	24.15	12.075	18.1125
11.5			1200	2.3	27.6	13.8	20.7
12			1225	2.3	28.175	14.088	21.13125
12.5		Siltstone with bands of phyllite	1400	2.3	32.2	16.1	24.15
13			1300	2.3	29.9	14.95	22.425
13.5			1100	2.3	25.3	12.65	18.975
14			1100	2.3	25.3	12.65	18.975
14.5			1000	2.3	23	11.5	17.25
15			800	2.3	18.4	9.2	13.8
15.5			550	2.3	12.65	25.3	18.975
16			425	2.3	9.775	19.55	14.6625
16.5			600	2.3	13.8	27.6	20.7
17			450	2.3	10.35	20.7	15.525
17.5			350	2.3	8.05	16.1	12.075
18			650	2.3	14.95	7.475	11.2125
18.5	Hasthoji	Meta siltstone (70%) + phyllite (30%)	850	2.2	18.7	9.35	14.025
19			925	2.2	20.35	10.175	15.2625
19.5	Hafkhalan	Thinly bedded meta siltstone	650	2.2	14.3	7.15	10.725
20			450	2.2	9.9	19.8	14.85
20.5	Tragbal	Meta siltstone	400	2.3	9.2	18.4	13.8
21			250	2.3	5.75	11.5	8.625
21.5			350	2.3	8.05	16.1	12.075
22	Panjal	Meta basics	450	2.5	11.25	22.5	16.875
22.5	Volcanics		350	2.5	8.75	17.5	13.125
23.067			50	2.5	1.25	2.5	1.875

Table 20 Strain levels associated with various degrees of squeezing [38, 40]

S. no.	Degree of squeezing	Normalized tunnel closure (%)
1.	Very mild squeezing	1–2
2.	Mild squeezing	2–3
3.	Mild to moderate squeezing	3–4
4.	Moderate squeezing	4–5
5.	High squeezing	5–7
6.	Very high squeezing	> 7

2360 MPa. The thickness of p-gravel backfill was 200 mm. Consequently, a 200 mm thick grout ring would come into play to establish a direct contact between concrete liners and the surrounding rock mass. The stiffness of this grouted p-gravel ring was also obtained using the equation for concrete liners as 1428 MPa. The stiffness of the combined support system was therefore 3788 MPa.

Correlations for Tunnel Closure

On the basis of analysis of data obtained from field instrumentation and monitoring of more than 60 tunnel sections, Goel [39] and Singh and Goel [40] presented correlations for prediction of radial tunnel closure in percent as a function of overburden depth, rock mass number and the combined stiffness of the support system. These correlations were presented both for non-squeezing and squeezing ground conditions and were used to predict tunnel closure at various chainages.

Correlations for Support Pressure

The correlations used here for prediction of support pressure are based on the measured support pressures and the other related parameters from several Indian tunnels. Two sets of empirical correlations for estimating the support pressure for tunnel sections under non-squeezing and squeezing ground conditions were developed by Goel et al. [38, 39], Singh and Goel [40] and were used to obtain values of support pressure.

Tunnel Closure and Support Pressure

Computations were therefore performed for prediction of tunnel closure (%) and support pressure (MPa) after installation of the combined support system, i.e. at the end of 42 h after excavation of the HRT. These values are presented in Tables 24 all along the length of HRT for $J_r/J_a < 0.25$. It was found that both tunnel closure and support pressures reduce with increase in RMR. However, for a given value of RMR, estimated values of tunnel closure and support pressures were found to be independent of the value of J_r/J_a. A close look at Table 24 shows that maximum value of tunnel closure occurs in Hasthoji Formation (Ch. 19.0 km) and is 0.2038%. However, it can also be observed from Table 24 that corresponding value of support pressure is 2.1634 MPa and hence more than the design pressure of 1 MPa. For chainage 18.0–18.5 km (transition between Razdhan and Hasthoji Formations), the support pressure is anticipated to be 1.7956 MPa.

In view of these excess support pressures, it was therefore recommended that secondary radial grouting of rock mass surrounding the tunnel be carried out in all those stretches of HRT wherever moderate and high squeezing ground conditions were expected. The secondary grouting be carried out up to a radial distance equal to the maximum value of the radius of plastic or broken rock mass zone. In general, it should extend to a radial distance of about 15–20 m.

Prediction of Tunnel Closure and Support Pressure After Secondary Radial Grouting of Rock Mass

The proposed secondary grouting would help in sealing all rock mass joints in the grouted region resulting in enhanced values of RQD or RMR. Moreover, the stiffness of the ring formed by such secondary grouting around the tunnel would play a major role in controlling the subsequent values of both tunnel closures and the support pressures. In view of this, in order to account for the effect of secondary grouting, RMR values all along the stretch of HRT in Hasthoji and Hafkhalan formations were enhanced by 10 and the improved values of Barton's rock mass quality, Q and rock mass number, N were re-computed. Correspondingly, tunnel closures and support pressures were also predicted in these formations and these values are presented in Table 25 which shows that in Hasthoji Formation, the ground condition has improved from high squeezing ground to moderate squeezing ground condition. The maximum tunnel closure has reduced to 0.0886% corresponding to a maximum support pressure of 0.2255 MPa which is far less than 1 MPa, the design pressure of segmental concrete liners or the shield of TBM and hence the support system could be treated as safe.

Concluding Remarks

For almost a 24 km long HRT passing through different geological formations and with varying depth of overburden, Hasthoji and the Hafkhalan Formations were found to be most critical. However, following the procedure of pre-excavation grouting and post excavation secondary grouting helped in bringing the support pressures and hence the

Table 21 Summary of squeezing potential prediction

Ch. (km)	Geological formation	Rock types	H (m)	m_i	σ_{ci} (MPa)	RMR	GSI	σ_{cm} (MPa)	E_d (GPa)	p_o (MPa) (Table 19)	Plastic zone Dia. (m)	Strain (%)	Squeezing potential
0	Panjal	Meta basics	75	20	160	80	75	65.24	53.34	2.81	1.312	0.0023	NSQ
0.5	Volcanics		300	20	160	80	75	65.24	53.34	11.25	2.892	0.0375	NSQ
1			550	20	160	80	75	65.24	53.34	20.63	4.085	0.126	NSQ
1.5			550	20	160	80	75	65.24	53.34	20.63	4.085	0.126	NSQ
2			400	20	160	80	75	65.24	53.34	15.0	3.41	0.067	NSQ
2.5	Razdhan	Meta siltstones meta siltstones	400	10	55	60	55	9.27	9.89	13.8	9.40	2.345	MSQ
3			400	10	55	60	55	9.27	9.89	13.8	9.40	2.345	MSQ
3.5			400	10	55	60	55	9.27	9.89	13.8	9.40	2.345	MSQ
4			350	10	55	60	55	9.27	9.89	12.07	8.71	1.795	VMSQ
4.5			350	10	55	60	55	9.27	9.89	12.07	8.71	1.795	VMSQ
5			350	10	55	60	55	9.27	9.89	12.07	8.71	1.795	VMSQ
5.5			550	10	55	60	55	9.27	9.89	18.99	11.27	4.433	MODSQ
6			400	10	55	60	55	9.27	9.89	13.80	9.40	2.345	MSQ
6.5			675	10	55	60	55	9.27	9.89	11.64	8.53	1.669	VMSQ
7			800	10	55	60	55	9.27	9.89	13.80	9.40	2.345	MSQ
7.5			650	10	55	60	55	9.27	9.89	11.21	8.35	1.548	VMSQ
8			475	10	55	60	55	9.27	9.89	16.38	10.36	3.306	MODSQ
8.5			450	10	55	60	55	9.27	9.89	15.52	10.05	2.967	MSQ
9			550	10	55	60	55	9.27	9.89	18.97	11.27	4.433	MODSQ
9.5			700	10	55	60	55	9.27	9.89	12.07	8.71	1.795	VMSQ
10			1000	10	55	60	55	9.27	9.89	17.25	10.67	3.663	MODSQ
10.5			1150	10	55	60	55	9.27	9.89	19.84	11.56	4.845	MODSQ
11			1050	10	55	60	55	9.27	9.89	18.11	10.97	4.039	MODSQ
11.5			1200	10	55	60	55	9.27	9.89	20.70	11.84	5.275	HISQ
12			1225	10	55	60	55	9.27	9.89	21.13	11.98	5.498	HISQ
12.5			1400	10	55	60	55	9.273	9.890	24.10	12.932	7.180	VHISQ
13			1300	10	55	60	55	9.27	9.89	22.42	12.39	6.192	HISQ
13.5			1100	10	55	60	55	9.27	9.89	18.97	11.27	4.433	MODSQ
14			1100	10	55	60	55	9.27	9.89	18.97	11.27	4.433	MODSQ
14.5			1000	10	55	60	55	9.27	9.89	17.25	10.66	3.664	MODSQ
15			800	10	55	60	55	9.27	9.89	13.80	9.40	2.345	MSQ
15.5			550	10	55	60	55	9.27	9.89	18.97	11.27	4.433	MODSQ
16			425	10	55	60	55	9.27	9.89	14.66	9.73	2.647	MSQ
16.5			600	10	55	60	55	9.27	9.89	20.70	11.84	5.276	HISQ
17			450	10	55	60	55	9.27	9.89	15.52	10.05	2.967	MSQ
17.5			350	10	55	60	55	9.27	9.89	12.07	8.71	1.795	VMSQ
18			650	10	55	60	55	9.27	9.89	11.21	8.35	1.548	VMSQ
18.5	Hasthoji		850	6	35	30	25	1.42	1.40	14.02	29.05	122.92	VHISQ
19			925	6	35	30	25	1.42	1.40	15.26	30.48	145.58	VHISQ
19.5	Hafkhalan		650	7	40	40	30	2.18	2.00	10.72	19.53	30.515	VHISQ
20			450	7	40	40	30	2.18	2.00	14.85	23.51	58.502	VHISQ
20.5	Tragbal		400	13	100	75	70	31.07	31.62	13.80	4.96	0.248	NSQ
21			250	13	100	75	70	31.07	31.62	8.63	3.79	0.097	NSQ
21.5			350	13	100	75	70	31.07	31.62	12.08	4.59	0.190	NSQ
22	Panjal Volcanics	Meta basics	450	20	160	80	75	65.24	53.34	16.88	3.64	0.084	NSQ
22.5			350	20	160	80	75	65.24	53.34	13.13	3.16	0.051	NSQ
23.7			50	20	160	80	75	65.24	53.34	1.87	1.04	0.001	NSQ

Table 22 Prediction of stand-up time as a function of RMR, size of HRT (= 6.3 m) and depth of overburden

Chainage (km)	Geological formation	Rock type	Overburden, H (m)	*RMR_lower*	Stand-up time Viladkar et al. [48, 49]	Average stand-up time Bieniawski [50]
0	Panjal	Meta basics	75		11.77	20 years
	Volcanics				months	
0.5			300		9.62 weeks	
1			550		1.53 weeks	
1.5			550		1.53 weeks	
2			400		4.61 weeks	
2.5	Razdhan	Phyllitic quartzite	400	60	1.50 days	12 weeks
3			400	60	1.50 days	
3.5			400	60	1.50 days	
4			350	60	2.16 days	
4.5			350	60	2.16 days	
5			350	60	2.16 days	
5.5			550	60	11.91 h	
6			400	60	1.50 days	
6.5		Quartzitic phyllite	675	60	4.75 h	
7			800	60	1.89 h	
7.5			650	60	5.70 h	
8			475	60	20.69 h	
8.5			450	60	1.04 days	
9			550	60	11.91 h	
9.5		Granite	700	60	3.95 h	
10			1000	60	0.43 h	
10.5			1150	60	0.14 h	
11			1050	60	0.30 h	
11.5			1200	60	0.10 h	
12			1225	60	0.08 h	
12.5		Siltstone with bands of phyllite	1400	60	0.02 h	
13			1300	60	0.05 h	
13.5			1100	60	0.21 h	
14			1100	60	0.21 h	
14.5			1000	60	0.43 h	
15			800	60	1.89 h	
15.5			550	60	11.91 h	
16			425	60	1.25 days	
16.5			600	60	8.24 h	
17			450	60	1.04 days	
17.5			350	60	2.16 days	
18			650	60	5.70 h	
18.5	Hasthoji	Meta siltstone	850	30	0.01 h	2 h
19			925	30	0.01 h	
19.5	Halfkhalan	Thinly bedded meta siltstone	650	40	0.26 h	10 h
20			450	40	1.15 h	
20.5	Tragbal	Meta siltstone	400	75	2.14 weeks	6.2 years
21			250	75	6.45 weeks	
21.5			350	75	3.09 weeks	
22	Panjal	Meta basics	450	80	3.19 weeks	20 years
22.5	Volcanics		350	80	6.66 weeks	
23.067			50	80	1.16 years	

Table 23 Probability of occurrence of rock burst during excavation of HRT tunnel size, $B = 6.3$ m; $SRF = 2.5$; unit weight, $\gamma = 2.5$ t/m^3; $J_r/J_a = 1.5$

Ch. (km)	Geological formation	Rock types	H (m)	RMR	Q_{lower}	$N_{lower} = Q.SRF$	Ground condition [36]	UCS (MPa)	$q_{c,mass}$ (MPa)	$q'_{c,mass}$ (MPa)	$\sigma_{\theta,\max}$ (MPa)	Ratio $= \sigma_{\theta,max}/q'_{c,mass}$	Ground condition [51]
10	Razdhan	Granite	1000	60	5.92	14.79	MRB	55	31.65	76.64	50	0.652	MRB
10.5			1150	60	5.92	14.79	MRB	55	31.65	83.39	57.5	0.690	
11			1050	60	5.92	14.79	MRB	55	31.65	78.89	52.5	0.666	
11.5			1200	60	5.92	14.79	MRB	55	31.65	85.64	60	0.701	
12			1225	60	5.92	14.79	MRB	55	31.65	86.76	61.25	0.706	
12.5		Siltstone with bands of Phyllite	1400	60	5.92	14.79	MRB	55	31.65	94.63	70	0.740	
13			1300	60	5.92	14.79	MRB	55	31.65	90.13	65	0.721	
13.5			1100	60	5.92	14.79	MRB	55	31.65	81.14	55	0.678	
14			1100	60	5.92	14.79	MRB	55	31.65	81.14	55	0.678	
14.5			1000	60	5.92	14.79	MRB	55	31.65	76.64	50	0.652	
15			800	60	5.92	14.79	NSQ	55	31.65	67.64	40	0.591	

pressure on TBM shield to within the permissible values. The construction of this HRT was completed on schedule.

Some Other Geomechanical Challenges

Past and Present Scenario

The application of Geotechnology is typically comprised of four stages: (1) site characterization, (2) design, (3) construction, and (4) assessment of performance during and post construction. Site characterization includes both field exploration and laboratory testing. Design involves interpretation and evaluation of site data; and development and application of theories of ground mass behavior, ground-structure interaction, ground water flow etc. Construction technology consists of adjusting the design and construction methods to accommodate actual ground conditions. Performance assessment is basically to account for the great variability of the natural ground. Validation of design by measurement and evaluation of field performance of structures with geotechnical components during construction and in the post construction period is frequently required. Before I pose some of the new challenging problems which have already emerged and which the young geotechnical engineers will have to face in the near future, I think it is proper to take a review of what happened in the previous century.

As stated earlier, the earliest contributions in Soil Mechanics came from Coulomb in 1776 and Rankine in 1857. Subsequently, major contributions appeared in the first half of the twentieth century when the scope of soil mechanics and foundation engineering consisted of a relatively limited range of topics which formed the contents of the classical text by Taylor [54], which included: (1) soil classification; (2) capillarity, permeability and seepage; (3) stress analysis by elasticity; (4) consolidation and settlement analysis; (5) shear strength of sands and cohesive soils; (6) slope stability; (7) lateral pressures and retaining walls; and (8) bearing capacity: shallow and deep foundations.

However, the developments brought about in the second half of the twentieth century have been just great and by the mid 1970's, the scope of the field had broadened greatly; new sub-disciplines had emerged, and the area of Soil Mechanics and Foundation Engineering came to be known as geotechnical engineering. These developments during the period from 1950 till the beginning of this century [55] included:

1950–1960: Soil fabric and structure, compacted clay properties, pavement design, soil stabilization, slope stability, shear strength, transient loading;

1960–1970: Rock mechanics, computer applications, finite element analyses, soil–structure interaction, soil dynamics, liquefaction, earth and rock fill dams, pore pressure, effective stress analysis, offshore;

1970–1980: Expansive soils, constitutive modeling of soils and rocks, in situ testing methods, soil dynamics, centrifuge testing, partly saturated soils, geotechnical earthquake engineering, underground construction;

1980–1990: Groundwater and geo-hydrology, environmental geotechnics, ground improvement techniques, risk and reliability;

1990–2000: Land reclamation, waste containment, site remediation, seismic risk mitigation, geophysical applications, geographic information systems (GIS);

Table 24 Tunnel closure and support pressure after installation of combined support system ($J_r/J_a < 0.25$)

Ch. (km)	Geological formation	Rock types	H (m)	Lower RMR	Q_{lower}	N_{lower}	Ground condition [36]	Anticipated Tunnel closure (%)	Anticipated support pressure (MPa)
0	Panjal	Meta basics	75	80	54.60	136.50	SSP	0.0037	0.0021
0.5	Volcanics		300	80	54.60	136.50	SSP	0.0086	0.0081
1			550	80	54.60	136.50	SSP	0.0123	0.0110
1.5			550	80	54.60	136.50	SSP	0.0123	0.0110
2			400	80	54.60	136.50	SSP	0.0102	0.0095
2.5	Razdhan	Phyllitic quartzite	400	70	5.92	14.79	NSQ	0.0248	0.0608
3			400	70	5.92	14.79	NSQ	0.0248	0.0608
3.5			400	70	5.92	14.79	NSQ	0.0248	0.0608
4			350	70	5.92	14.79	NSQ	0.0228	0.0595
4.5			350	70	5.92	14.79	NSQ	0.0228	0.0595
5			350	70	5.92	14.79	NSQ	0.0228	0.0595
5.5			550	70	5.92	14.79	NSQ	0.0300	0.0640
6			400	70	5.92	14.79	NSQ	0.0248	0.0608
6.5		Quartzitic phyllite	675	70	5.92	14.79	MSQ	0.0583	0.1412
7			800	70	5.92	14.79	MSQ	0.0667	0.1578
7.5			650	70	5.92	14.79	MSQ	0.0565	0.1379
8			475	70	5.92	14.79	NSQ	0.0274	0.0625
8.5			450	70	5.92	14.79	NSQ	0.0266	0.0620
9			550	70	5.92	14.79	NSQ	0.0300	0.0640
9.5		Granite	700	70	5.92	14.79	MSQ	0.0600	0.1445
10			1000	70	5.92	14.79	MODSQ	0.0798	0.1861
10.5			1150	70	5.92	14.79	MODSQ	0.0892	0.2087
11			1050	70	5.92	14.79	MODSQ	0.0830	0.1935
11.5			1200	70	5.92	14.79	MODSQ	0.0923	0.2166
12			1225	70	5.92	14.79	MODSQ	0.0939	0.2206
12.5		Siltstone with bands of phyllite	1400	70	5.92	14.79	HISQ	0.1044	0.2497
13			1300	70	5.92	14.79	HISQ	0.0984	0.2328
13.5			1100	70	5.92	14.79	MODSQ	0.0861	0.2010
14			1100	70	5.92	14.79	MODSQ	0.0861	0.2010
14.5			1000	70	5.92	14.79	MODSQ	0.0798	0.1861
15			800	70	5.92	14.79	MSQ	0.0667	0.1578
15.5			550	70	5.92	14.79	NSQ	0.0300	0.0640
16			425	70	5.92	14.79	NSQ	0.0257	0.0614
16.5			600	70	5.92	14.79	MSQ	0.0530	0.1315
17			450	70	5.92	14.79	NSQ	0.0266	0.0620
17.5			350	70	5.92	14.79	NSQ	0.0228	0.0595
18			650	70	5.92	14.79	MSQ	0.0565	0.1379
18.5	Hasthoji	Meta siltstone	850	35	0.21	0.53	HISQ	0.1904	1.7956
19			925	35	0.21	0.53	HISQ	0.2038	2.1634
19.5	Halfkhalan	Thinly bedded meta siltstone	650	50	0.64	0.53	HISQ	0.1101	0.4136
20			450	50	0.64	1.60	MODSQ	0.0820	0.2722
20.5	Tragbal	Meta siltstone	400	75	31.33	78.31	SSP	0.0127	0.0190
21			250	75	31.33	78.31	SSP	0.0096	0.0164
21.5			350	75	31.33	78.31	SSP	0.0117	0.0182
22	Panjal	Meta basics	450	80	54.60	136.50	SSP	0.0109	0.0100
22.5	Volcanics		350	80	54.60	136.50	SSP	0.0094	0.0088
23.067			50	80	54.60	136.50	SSP	0.0029	0.0005

Table 25 Computation of tunnel closure and support pressure after installation of combined support system and secondary grouting

Ch. (km)	Geological formation	Rock types	*H* (m)	Improved RMR	*Q_improved*	*N_improved*	Ground condition [37]	Anticipated Tunnel closure (%) [40]	Anticipated support Pressure (MPa) [40]
18.5	Hasthoji	Meta siltstone (70%) + phyllite (30%)	850	55	3.39	8.49	MODSQ	0.0828	0.2093
19			925	55	3.39	8.49	MODSQ	0.0886	0.2255
19.5	Halfkhalan	Thinly bedded meta siltstone	650	60	5.92	14.79	MODSQ	0.0565	0.1379
20			450	60	5.92	14.79	MODSQ	0.0266	0.0620

2000–2010: Information technology applications, sustainability, improved ground treatment methods, sensors and actuators, data mining, automated monitoring, enhanced and extended applications of the observational method.

The scope of geotechnical engineering has now broadened to the point where Geo-technology or Geo-engineering at present draws on several related disciplines which include: engineering geology and hydro-geology, seismology and geophysics, rock mechanics and rock engineering, civil engineering, off shore and deep shore engineering, mining engineering, and also the upstream areas of petroleum engineering. Considering the ground situation in the construction industry, geotechnical engineering and infra-structure construction in India are these days strongly influenced by various factors such as:

1. Public–private partnership (PPP) mode of execution of all major infra-structure projects including: (a) design and build (DB) mode, (b) build-own-operate (BOO) mode, (c) design-build-finance-operate (DBFO) mode, (d) build-own-operate-transfer (BOPT) mode, and (e) build-lease-operate-transfer (BLOT) mode, etc.;
2. Regulatory authorities and legal mechanisms, which now have significant impact on construction practices, e.g. the role of National Green Tribunal (NGT);
3. Health and safety issues, which also have now become very important;
4. Decisions are often made using the results of risk, reliability, and decision analyses;
5. Information technology is stimulating new approaches to interactive design and construction procedures, and
6. Quality Assurance (QA) and Quality Control (QC) monitoring and long term evaluation of performance and condition i.e. a digital age application of the observational method.

Therefore, with such widening of the scope of *geotechnical engineering*, many new and more challenging problems are coming forth and which will now be discussed briefly.

Challenges in Energy Sector

Resource Discovery and Recovery

The development and conservation of natural resources is vital to economic development and national security. Some of the energy resources include oil and gas, coal, hydropower, underground pumped hydropower, nuclear energy, and geo-thermal energy, etc. With increasing growth of population, industrialization, and urbanization, demand for most natural resources has increased steadily. Continued discovery and recovery of natural resources is therefore a national need. Resource recovery becomes more challenging as the readily accessible supplies of raw materials are recovered. Enhancement of the practical recoverability of the difficult-to-explore energy reserves and development of technologies to exploit them require sophisticated geotechnical expertise.

1. Methane Hydrates as a source of fuel

Geotechnical inputs are crucial to locating, developing, and extracting fossil fuels. Offshore and deep shore methane hydrate deposits are a major potential source of energy for the millennium ahead. The total estimated source from natural gas hydrates in India has been estimated as 1894 trillion m^3 [56]. In 1997, Govt. of India formed National Gas Hydrates Program (NGHP) to explore and develop country's gas hydrate resources. During the first NGHP expedition in 2006, an attempt was made to explore four areas of Indian Ocean, namely, Krishna-Godavari basin, Mahanadi basin, Andaman islands, and Kerala-Konkan region. The primary goal of NGHP expedition-01 was to conduct scientific ocean drilling, coring, logging and analytical activities to assess geological occurrence, regional context and characteristics of gas hydrate deposits along the continental margins of India. The expedition assessed data from 39 boreholes in four different regions and samples from Krishna-Godavari basin region were found to contain one of the richest marine gas hydrate accumulations. At a site offshore the Andaman Islands, gas

hydrate bearing volcanic ash layers were encountered as far as 600 m below the sea floor.

Sain et al. [57] found that at low temperature and under high pressure, methane hydrate is a crystalline solid. However, at higher temperature and lower pressure, the crystalline form of methane hydrate becomes unstable, and the recovery procedure becomes highly complicated. Safe and economical recovery of methane hydrates from the relatively deep and unstable underwater environment in which they are found is a major geo-engineering challenge.

2. Hydrogen as an alternative fuel

The recent focus on hydrogen as a fuel is based on the fact that burning hydrogen emits no carbon dioxide. Possible hydrogen sources include mining of methane clathrates, also referred to as methane hydrate having a large amount of methane trapped within the crystal structure of water, forming a solid similar to ice. Methane clathrates are common constituents in deep sedimentary structures and form outcrops on the ocean floor [58]. These are formed by migration of gas along deep geological faults, followed by precipitation or crystallization on contact of the rising gas stream with cold sea water. The problems to be solved to develop hydrogen as a viable energy alternative include: (a) finding sources for hydrogen, (b) storage of hydrogen, and (c) developing low-cost reliable hydrogen fuel cells. Finding sources for hydrogen will involve the role of geo-engineers.

3. Geothermal energy

Increasing attention is also being focused on sources of energy that are renewable and generate no emissions. Geothermal energy taps the heat sources of Earth, either directly for heating and cooling, or to make electricity. Geothermal reservoirs can be characterized and managed using geo-engineering. Various methods of generating electricity using geothermal energy include—(a) dry-steam power stations, (b) flash steam power stations, and (c) binary cycle power stations.

Well Bore Stability During Drilling for Oil and Gas

In all problems discussed in "Resource Discovery and Recovery" section above, maintaining deep well bore stability during drilling and afterwards, is a very important issue in oil and gas industry. During the process of drilling, economic losses caused by wellbore instability are prohibitively high and lead to very high non-productive time period. When an oil well is drilled, the geological formation around the wellbore has to withstand the resulting stress concentration around the well bore. If the strength of the formation is not adequate, material failure occurs around the well bore. This well bore stability is not only a problem of rock mechanics but also a problem of multi-phase physics and multi-mechanics, and involves coupled interaction of drilling fluid with shale. Various other causes of deep well bore instability [59] could be: (1) naturally fractured or faulted formations, (2) tectonically stressed formations and high in situ stresses, (3) mobile formations, (4) unconsolidated formations, (5) naturally over-pressured shale collapse, and (6) induced over-pressured shale collapse. In order to study this aspect in detail, it requires

(a) Geomechanical modelling of an oil field strata

In order to undertake the above studies, it requires geomechanical modelling of the oil field which consists of:

1. 3D Modelling of spatial domain: variation of geological strata with depth; geological fault mapping and its implication on stress regime,
2. Modelling of loading conditions: 3-D in situ stress field including the magnitude and orientation of stresses; prediction of pore (water + gas) pressure distribution with depth; prediction of bottom-hole pressure;
3. Constitutive modelling: anisotropic in situ formation properties in different strata; and borehole failure criteria, etc.

(b) Geomechanical analysis and related issues

The well bore stability analysis is basically a coupled chemical–mechanical analysis which is influenced by various factors like [59–62]: drilling fluid-shale interaction effect; flow induced stress effect; and temperature alteration effect; etc. Apart from these, emphasis also needs to be given to issues like: hydration of shale as affected by high pressure and temperature conditions, diffusion of free water from drilling fluid into shale formations; adjustment of density of drilling fluid with time so as to avoid the collapse of the well bore; etc.

Challenges Associated with Mineral Resources

Metals and industrial minerals are essential for sustaining our present day standards of living. In addition to conventional geo-mechanical issues associated with economical extraction of mineral resources, geo-engineering has to deal with issues related to mining with due consideration to environmental problems.

Challenges Due to Submarine Landslides

Causes

Research workers have specified many possible causes for the initiation of submarine landslides including: (1) over steepening, (2) seismic loading, (3) storm-wave loading, (4) rapid accumulation and under consolidation, (5) gas

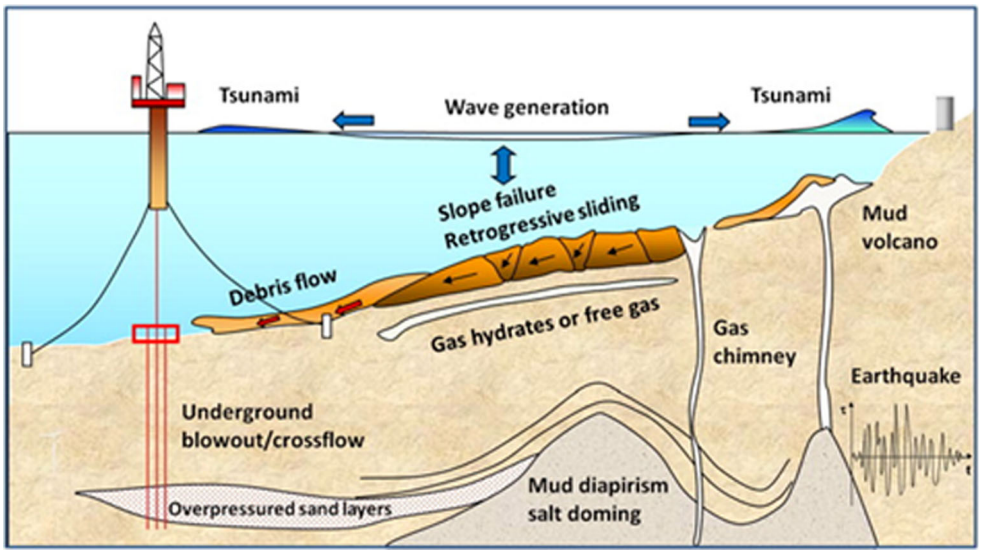

Fig. 42 Case of sub-marine slope failure [63, 64]

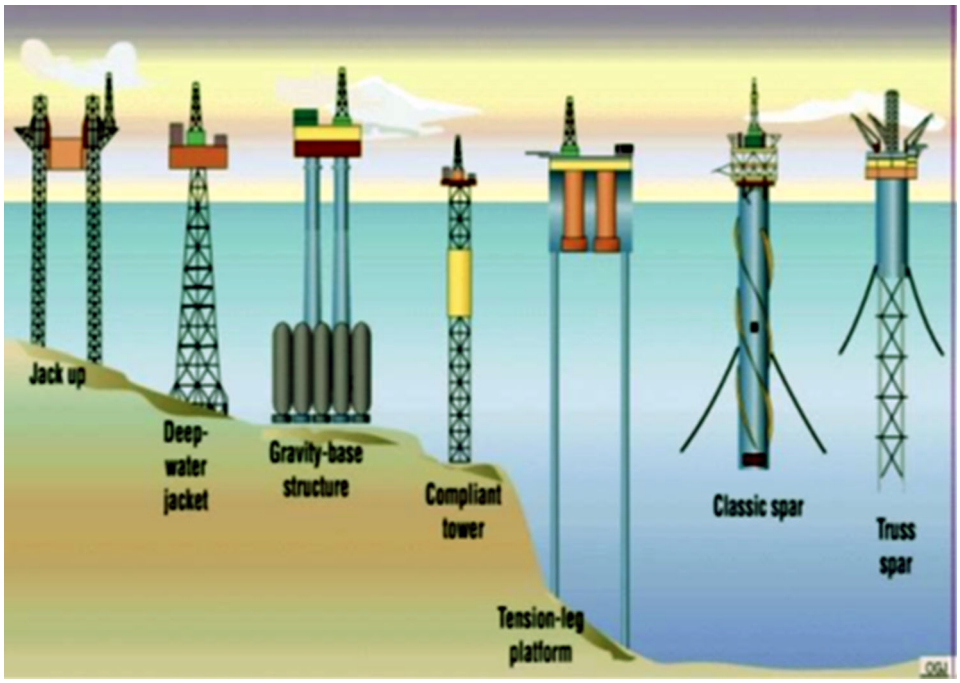

Fig. 43 Various foundation types for different situations [65, 66]

charging, (6) gas hydrate disassociation, (7) low tides, (8) seepage (9) glacial loading and (10) volcanic island processes [63, 64]. The geomechanical challenge here is that if such a failure occurs in the vicinity of the foundation of any deep shore exploration vessel, it can prove to be catastrophic. Moreover, a major submarine landslide can itself become a cause for triggering a tsunami (Fig. 42).

Investigations Required

A typical investigation into submarine landslides should include:

1. Understanding the sediment; its physical and mechanical properties; and elastic properties of slip planes,
2. Understanding the dynamics of failure of seafloor through 3-D imaging of sediment formation and geometry of failures surfaces; post-failure behavior of debris and mud flows,
3. Determination of the presence of gas hydrate and its significance for slope stability,
4. Modelling of forces and mechanical processes that control the initiation of slope instabilities; flow dynamics; and initiation of tsunamis, and

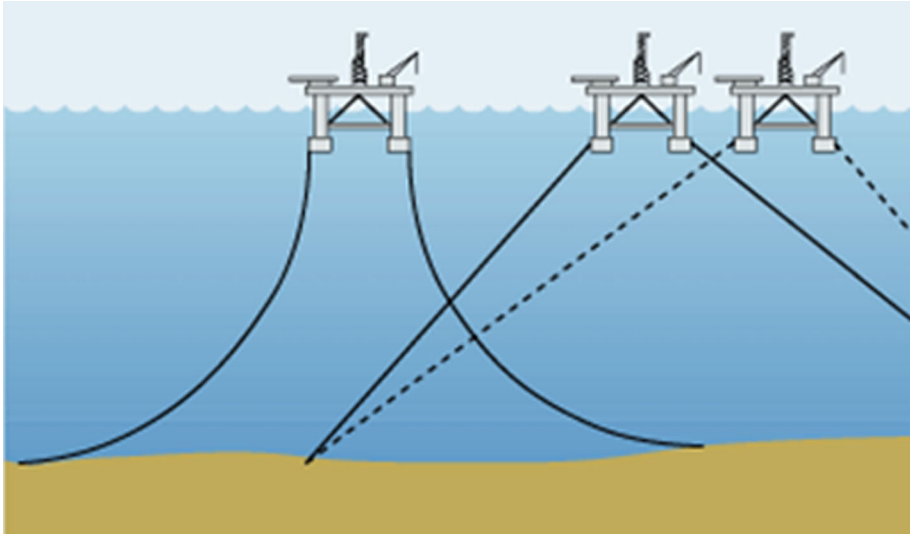

Fig. 44 Catenary and taut leg mooring system [67]

5. Assessment of hazard; associated risk; frequency and extent of hazard.

Numerical Modelling of Landslide Dynamics

Submarine landslides may have huge dimensions and long run-out distances. Modelling the entire three-dimensional problem is a huge computational task, and usually has to be reduced to a two-dimensional problem through depth averaging or through restriction to cross sections to save computational resources. However, even a two-dimensional simulation is a non-trivial task for large landslides. If it is known that the lateral spreading of the flowing mass is weak or limited, the flow evolution in the transverse direction may be neglected and one-dimension models may be applied. The stability analysis should account for: (1) the multi-layer structure of a submarine landslide with a dense debris flow at the bottom and a dilute suspension flow above; (2) vertical density variations and the associated variation of mechanical properties in the form of clay rheology in view of the flow dynamics. Clay slurries exhibit yield strength threshold behavior and viscosity, not only for shear flows, but also in extensional flows. In the modelling of failure and rupture, the separation of two material volumes that were originally adjacent poses specific problems. It is essential to predict the emergence of possible shear bands at the correct places.

Challenges in Deep Shore Foundations

Foundation Types

The Govt. of India has already undertaken program of deep shore exploration of oil and gas. For deep shore structures,

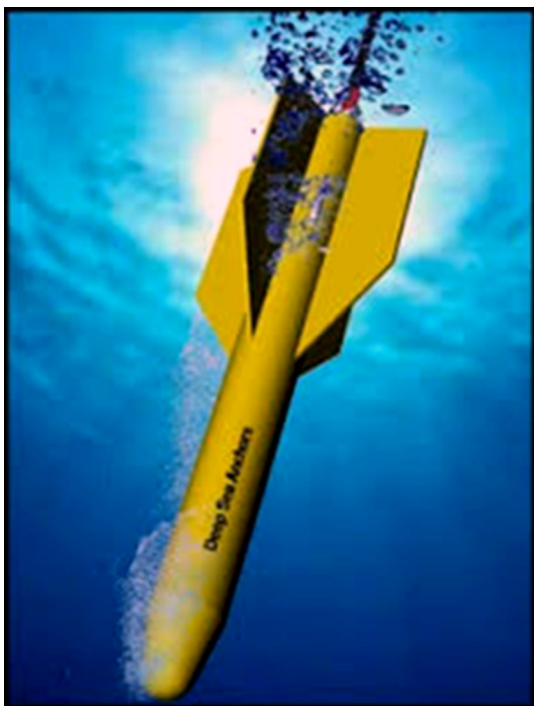

Fig. 45 Schematic of a Torpedo anchor [68]

application of in situ data and design principles of traditional offshore foundations have to be adjusted for new types of foundations regarding the geometry, applied load, geo-hazards and should be used cautiously. New foundation types could be either a compliant tower (depth of water—1500′–3000′) or tension leg platform (1500′–7000′) or mooring system like classic SPAR or Truss SPAR floating system (2000′–10,000′) (Fig. 43).

Mooring Systems

An offshore mooring system for deep shore foundations is basically comprised of three parts: an anchor system, a mooring line and a specific mooring layout. The mooring system layout depends on the local environmental conditions and the purpose of the offshore unit. Three types of mooring systems are in practice as stated below:

(a) Tension leg mooring system

This system is comprised of tubular steel legs (Fig. 43) which consist of multiple tubular steel members called as tendons. Tensioning the steel legs is done by buoyancy in the floating offshore unit. The high tension in the tension legs limits horizontal offsets to a small percentage of the water depth. Due to the high axial stiffness of the tendons, the heave, roll and pitch motions are negligible.

(b) Catenary and taut leg mooring system

The catenary system is the most common type of mooring system employed in shallow waters. It provides restoring forces through the suspended weight of the mooring lines and its change in configuration arising from vessel motion. By catenary system, the mooring line terminates horizontally at the sea bed (Fig. 44), the anchor point is only subjected to horizontal forces at the seabed. With the increase of water depth, the weight and the length of the mooring lines start to increase rapidly. In deep water, the weight of the mooring lines becomes excessive and the mooring lines tend to hang directly down from the rig. The excessive weight diminishes the working payload of the vessel of floating offshore structure. To overcome this problem synthetic ropes are used in the mooring line.

In taut leg system, the mooring lines are pre-tensioned until they are taut. The mooring line terminates at an angle at the seabed. (30°–45°) i.e. the anchor points are loaded by horizontal and vertical forces. The taut leg system has a much more linear stiffness than the catenary system which gives the advantage that the offsets under mean load can be better controlled and the total mooring line tensions are smaller. The disadvantage of the taut-leg system is that the mooring line must have sufficient elasticity to absorb the vessel wave motions without overloading.

(c) SPAR or truss SPAR system

A SPAR is a type of floating oil platforms typically used in very deep waters (Fig. 43) that are moored in place vertically. A spar platform consists of a large-diameter, single vertical cylinder supporting a deck. The cylinder is weighted at the bottom by a chamber filled with a material that is denser than water in order to lower the C.G. of the platform and provide stability. Moreover, the spar hull is encircled by helical strakes to mitigate the effects of vortex-induced motion. Spars are permanently anchored to the seabed by way of a spread mooring system composed of either a chain-wire-chain or chain-polyester-chain configuration.

Torpedo Anchors

Torpedo anchors are used as foundations for mooring deep-water offshore facilities, including risers floating structures (Fig. 45). They are cone-tipped cylindrical steel pipes ballasted with concrete and scrap metal and penetrate the seabed by the kinetic energy they acquire during free fall through the water. A mooring line is usually connected at the top of the anchor. The design of such anchors involves estimation of the embedment depth as well as short-term and long-term pullout capacities. The advantages of providing this anchor are: (1) it can be used in ultra-deep waters, (2) shorter time of installation, (3) no hammering involved during installation, (4) largely independent of water depth, (5) easily installed for riser flow line restraint, (6) large holding capacity, and (7) cost effectiveness and low cost of fabrication. The only disadvantage is that it may go out of target during installation due to horizontal drift.

The problem here is how to define its holding capacity as a function of its impact velocity, drag coefficient, penetration angle and depth of penetration into the sea bed. Real challenge in numerical simulation of such anchors is to develop a fully coupled dynamic consolidation of submarine sea bed under impact and penetration loading of torpedo anchor taking into account inertia effects, large deformations, finite strains of sea bed, and the flow of pore water through the soil [62, 69].

Summary and Conclusions

An attempt has been made here to identify the way in which the scope of current status of geotechnical engineering can be widened in view of some of the more challenging problems which are multi-disciplinary in nature. On basis of the work carried out by the author and the

state-of-art in other related disciplines, the following inferences can be drawn:

1. In view of the current global scenario, considerable work needs to be done in the area of extreme loading conditions, like for e.g. blast loading. The most important issue in this area is how to predict the blast load exerted on structures having different geometry and orientation with respect to blast, and whether the structure is an above ground structure, an underground structure or a semi-buried structure. This therefore becomes basically a problem of blast wave propagation either through air or through the ground and the consequent pressure distribution exerted on the structures. More importantly, the strain rates mobilized in different materials during the blast are very high and it is essential to understand the stress–strain behavior of geo-materials under such very high strain rates. The blast phenomenon also involves material fragmentation, numerical simulation of which poses many problems.
2. In case of tall structures like cooling towers and chimneys etc., the effects of nonlinearity and time dependency of the soil strata has not been considered. However, the influence of these parameters on the overall response need to be further investigated.
3. Majority of the hydro power projects are coming up in the Himalayan or sub-Himalayan regions where the problems posed by squeezing ground condition during tunneling or during large size excavations for caverns etc. are quite acute. It is essential that the project authorities pay more attention to collection of field data with respect to tunnel closure and support pressures. These data can be further analyzed to arrive at more reliable relationships for predicting the response of underground excavations.
4. Energy sector has already assumed considerable importance in view of the fast depletion of the conventional energy reserves and the importance Govt. of India has attached to it. Young geotechnical engineers therefore will have to deal with many related challenging problems of deep shore engineering, foundations for deep shore structures, sub-marine landslides and exploration of mineral resources from large depth.

It is therefore essential for young geotechnical engineers to widen the scope of their work into more inter-disciplinary and multi-disciplinary areas involving multi-scale, multi-physics, and multi-mechanics problems. The author feels that Geotechnical engineering must further evolve into a more general field of Geo-Engineering and encompass within itself areas like engineering geology and hydro-geology, seismology and geophysics, rock mechanics and rock engineering, civil engineering, off shore and deep shore engineering, mining engineering, and also some of the upstream areas of petroleum engineering.

Acknowledgements At the outset, I must greatly appreciate this honour of being invited by the Indian Geotechnical Society to deliver the 39th IGS Annual Lecture 2017 during IGC 2017. I am therefore extremely thankful to the IGS for giving me this opportunity to address the august gathering of geotechnical engineers from within India and abroad. The overall atmosphere in the erstwhile University of Roorkee and now IIT Roorkee has been quite serene and tranquil and extremely conducive for research right since the early sixties. I remain ever grateful to this institution for providing me ample opportunities for my professional nourishment. I personally treat this invitation as more of a tribute to all my Professors from whom I learnt a lot. I am also extremely thankful to my past and present colleagues, especially from geotechnical and structural engineering groups with whom I had a chance to closely work and interact. I shall ever remain extremely thankful to all of them. This invitation is also a tribute to all my doctoral students including RP Sharma, (Late) Jamaloddin Noorzaei, Karisiddappa, Manoj Verman, Sanjeev Garg, NK Samadhiya, SK Saran, Diganta Goswami, Adnan Jayed Zedan, AKMS Al-Assaddi, Moataz Al-Obaydi, Prashant Nagrale, T. Sahu, PKR Gautam, RD Dwivedi, Sujata Parida, Sumedha, Manendra Singh, Dipaloke Majumder and Vijay Kumar who have tirelessly worked with me. I am extremely thankful and indebted to all of them. The research work reported here could not have been carried out without the financial support from several public and private sponsoring agencies. Dr. Priti Maheshwari is one who helped me in setting the complete draft of this lecture in proper format. I must very much appreciate her meticulousness and also the patience she displayed while doing this job. I am also extremely thankful to the Organisers of IGC 2017, especially Prof. A Murali Krishna and his entire team from IIT Guwahati, and the IGS, Guwahati Chapter, for inviting me and giving me this unique and wonderful opportunity. Thanks are also due to my wife, Dr. Sushama for her patience, understanding and moral support to all my academic pursuits.

References

1. Viladkar MN, Bhargava P, Singh B, Iqbal MA (2012) Analysis of an under ground technical facility subjected to impact and blast loading. A report submitted to DRDO, New Delhi, India
2. ABAQUS/Explicit user's manual. Version 6.7, Vol. III & IV
3. Haaverstad TA (1994) Structural response to accidental explosions and fires on offshore process installations. J Loss Prev Process Ind 7(4):310–316

4. Lubliner J, Oliver J, Oller S, Oñate E (1989) A plastic-damage model for concrete. Int J Solids Struct 25(3):299–326
5. Hillerborg A, Modéer M, Peterson P-E (1976) Analysis of crack formation and crack growth in concrete by means of fracture mechanics and finite elements. Cem Concr Res 6:773–782
6. Sinha BP, Gerstle Kurt H, Tuli Leonard G (1964) Stress–strain relations for concrete under cyclic loading. J Am Concr Inst 6:195–212
7. Johnson GR, Cook WH (1983) A constitutive model and data for metals subjected to large strains, high strain rates and high temperatures. In: Proceedings of 7th international symposium on ballistics, The Hague, pp 541–547
8. Johnson GR, Cook WH (1985) Fracture characteristics of three metals subjected to various strains, strain rates, temperatures and pressures. Eng Fract Mech 21(1):31–48
9. TM 5-855-1 (1986) Fundamentals of protective design for conventional weapons. Department of the Army, Washington
10. http://www.jsw.in/steel/kakrapar-atomic-power-station. Accessed 19 Sept 2017
11. http://www.bbc.com/news/uk-england-leeds-35927009. Accessed 19 Sept 2017
12. Lu W, Lin B, Lu R (1986) Effect of unequal settlement of foundations on the stress resultants of hyperbolic cooling towers and the unequal settlement tolerance limit. Eng Struct 8:39–45
13. Kato S, Yoshinao C (1986) Stochastic stress analysis of cooling tower shells due to differential settlement. In: Proceedings of IASS symposium on shells, membranes and space frames, vol 1, pp 121–128
14. Kato S, Shori T, Gould PL (1986) A modified thin-layered far field soil element for soil–structure interaction of axisymmetric structures. Comput Geotech 2(3):167–184
15. Kato S, Hirota M, Gould PL (1986) Analysis of cooling towers on a soft soil layer subjected to horizontal incident earthquake motions from base back. Eng Struct 8(3):208–212
16. Kato S, Cheong MC, Tanaka K (1989) Stochastic evaluation of stresses in cooling tower shell due to uneven settlements. In: Proceedings of 3rd international symposium on natural draught cooling towers. IASS, Paris, pp 623–632
17. Tilak MM, Verma USP, Raghavan N (1990) Design aspects for a large natural draft cooling tower for a nuclear power project. In: Proceedings of the national seminar on cooling towers, New Delhi, TS IV/25–TS IV/29
18. Kato S, Han KJ, Cheong M-C (1991) Stress evaluation of cooling towers subjected to uneven settlements with stochastic characteristics. Eng Struct 13(4):329–344
19. Cheong MC (1991) Stress analysis of cooling tower shell considering up-lift of foundation by no tension method. In: Proceedings of IASS symposium on spatial structures, Copenhegen, Denmark, vol 3, pp 51–57
20. Horr AM, Safi M (2002) Full dynamic analysis of large concrete cooling towers: soil–structure interaction. Int J Space Struct 17(4):301–312
21. Viladkar MN, Karisidappa Bhargava P, Godbole PN (2006) Static soil–structure interaction response of hyperbolic cooling towers to symmetrical wind loads. Eng Struct 28(9):1236–1251
22. Shu W, Wenda L (1991) Gust factors for hyperbolic cooling towers on soils. Eng Struct 13(1):21–26
23. Bieniawski ZT (1975) Case studies: prediction of rock mass behaviour by the Geomechanical classification. In: Proceedings of 2nd Australia–New Zealand conference on geomechanics, Brisbane, Australia, pp 36–41
24. IS: 11504 (1985) Criteria for structural design of reinforced concrete natural draught cooling towers. Bureau of Indian Standards, New Delhi
25. BS 4485: Part-4 (1975) Specifications for water cooling towers. British Standard Institution, London
26. Krishna P, Pande PK, Godbole PN, Kumar K, Asawa GL, Ahuja AK (1989) Wind tunnel tests on rigid models of cooling towers for Kakrapar nuclear power station. Wind engineering studies Technical report, University of Roorkee, Roorkee, India
27. ACI-ASCE Committee 334 (1984) Reinforced concrete cooling tower shell-practice and commentary. J Am Concr Inst 81:623–631
28. Karisiddappa (1993) Finite element analysis of hyperbolic cooling towers under wind loads. Ph.D. Thesis, University of Roorkee, Roorkee, India
29. IS: 875 (Part-3) (1987) Code of practice for design loads (other than earthquake) for buildings and structures: part 3 wind loads. Bureau of Indian Standards, New Delhi
30. IS: 875 (Part-4) (1987) Code of practice for design loads (other than earthquake) for buildings and structures: part 3 snow loads. Bureau of Indian Standards, New Delhi
31. Irons BM (1976) The semi Loof shell elements. In: Ashwell DG, Gallagher RG (eds) Finite elements for thin shells and curved members. Wiley, London, pp 197–222
32. Irons BM, Ahmad S (1986) Techniques of finite elements. Ellis Horwood, Chichester
33. Karisiddappa Viladkar MN, Godbole PN, Krishna P (1998) Finite element analysis of column supported hyperbolic cooling towers using semi-loof shell and beam elements. Eng Struct 20(1–2):75–85
34. Noorzaei J (1991) Non-linear soil–structure interaction in framed structures. Ph.D. Thesis, University of Roorkee, Roorkee, India
35. Godbole PN, Viladkar MN, Noorzaei J (1991) Modified frontal solver with multi-element and variable degrees of freedom features. Comput Struct 39(5):525–534
36. Viladkar MN, Anbalagan R (2010) Geological and geotechnical review of HRT for Kishanganga Hydro Electric Project (J&K). A report based on technical note of M/s Halcrow Group Ltd. (UK), submitted to Hindustan Construction Company Ltd., Mumbai, India
37. Goel RK (1994) Correlations for predicting support pressures and closures in tunnels. Ph.D. Thesis, Nagpur University, Nagpur, India
38. Goel RK, Jethwa JL, Paithankar AG (1995) Indian experiences with Q and RMR systems. Tunn Undergr Space Technol 10(1):97–109
39. Goel RK (1995) Tunnelling in squeezing ground conditions. Riv Ital Di Geotec 1:35–40
40. Singh B, Goel RK (2006) Tunneling in weak rock (Elsevier geoengineering book series; v. 5). Elsevier, Oxford
41. Bieniawski ZT (1979) The geomechanics classification in rock engineering application. In: Reprinted from: Proceedings of the 4th congress of the international society for rock mechanics, A.A. Balkema, Rotterdam
42. Hoek E, Marinos P (2000) Predicting tunnel squeezing problems in weak heterogeneous rock masses. Tunn Tunn Int Part 1 32:1–20
43. Palmer M (2009) Technical note (WHKGHE/MJP/03, dated July 07, 2009) on Review of Geology and Rock Mass Properties for the TBM Section of the Headrace Tunnel
44. Hoek E, Brown ET (1980) Underground excavations in rock. Institution of Mining and Metallurgy, London
45. Palmer M (2009) Technical note (WHKGHE/MJP/02, dated April 29, 2009) on In Situ Stress Estimates
46. Hoek E (1999) Support for very weak rock associated with faults and shear zones. In: Villaescusa E, Windsor CR, Thompson AG (eds) Rock support and reinforcement practice in mining. Balkema, Rotterdam, pp 19–32
47. Sakurai S (1983) Displacement measurements associated with the design of underground openings. In: Proceedings of the

international symposium field measurements in geomechanics, Zurich, vol 2, pp 1163–1178
48. Verman M (1993) Rock mass—tunnel support interaction analysis. Ph.D. Thesis, University of Roorkee, Roorkee, India
49. Viladkar MN, Verman M, Singh B, Jethwa JL (2008) Rock mass–tunnel support interaction analysis: part-I—ground response curves. J Rock Mech Tunn Technol 14(2):103–126
50. Viladkar MN, Verman M, Singh B, Jethwa JL (2008) Rock mass–tunnel support interaction analysis: part-II—support reaction curves. J Rock Mech Tunn Technol 14(2):127–148
51. Bieniawski ZT (1989) Engineering rock mass classifications. Wiley, New York
52. Kumar N (2002) Rock mass characterization and evaluation of supports for tunnels in Himalaya. Ph.D. Thesis, I.I.T. Roorkee, Roorkee, India
53. Barton N, Lien R, Lunde J (1974) Engineering classification of rock masses for the design of tunnel support. Rock Mech 6:189–236
54. Taylor DW (1948) Fundamentals of soil mechanics. Wiley, New York
55. Mitchell JK (2006) New frontiers in geotechnical engineering. ASCE geotechnical special publication, no. 149, pp 1–5
56. Directorate General of Hydrocarbons (2007–2008) Gas hydrates: R&D advances in India. Report by Govt. of India
57. Sain K, Rajesh V, Satyavani N, Subbarao KV, Subrahmanyam C (2011) Gas-hydrate stability thickness map along the Indian continental margin. Mar Pet Geol 28(10):1779–1786
58. https://en.wikipedia.org/wiki/Methaneclathrate. Accessed 19 Sept 2017
59. Pašić B, Medimurec NG, Matanović D (2007) Well bore stability: causes and consequences. In: Proceedings of Rudarsko-geološko-naftni zbornik, Zagreb, Croatia, vol 19, pp 87–98
60. Chee PT, Brian GR (1998) Integrated rock mechanics and drilling fluid design approach to manage shale instability. SPE/ISRM Rock Mechanics in Petroleum Engineering
61. Yan C, Deng J, Yu B (2013) Wellbore stability in oil and gas drilling with chemical-mechanical coupling. Sci World J. Art. ID 720271:1-9
62. Sabetamal H, Carter JP, Nazem M, Sloan SW (2016) Coupled analysis of dynamically penetrating anchors. Comput Geotech 77:26–44
63. Locat J, Lee HJ (2000) Submarine landslides: advances and challenges. In: Proceedings of 8th international symposium on landslides, Cardiff, UK, pp 01–30
64. Maarten V, Sultan N, Garziglia S, Forsberg CF, L'Heureux JS (2014) Seafloor instabilities and sediment deformation processes: the need for integrated, multi-disciplinary investigations. Mar Geol 352:183–214
65. Lunne T (2012) The fourth James K. Mitchell Lecture: the CPT in offshore soil investigations—a historic perspective. Geomech Geoeng 7(2):75–101
66. Sheshpari M, Khalilzad S (2016) New frontiers in the offshore geotechnics and foundation design. Electron J Geotech Eng 21:1–59
67. Sefton SL, Firth K, Hallam S (1998) Installation and handling of steel permanent mooring cables. Offshore digital magazine. http://images.pennwellnet.com/ogj/images/off2/1198moor1.gif. Accessed 19 Sept 2017
68. http://coolarcticmoorings.weebly.com/uploads/1/0/3/4/10343992/298554512.jpg. Accessed 19 Sept 2017
69. Kim YH, Hossain MS, Wang D, Randolf MF (2015) Numerical investigation of dynamic installation of torpedo anchors in clay. Ocean Eng 108:820–832

Prof. M. N. Viladkar joined erstwhile University of Roorkee as Lecturer in Civil Engineering in 1978 and obtained Ph.D. from the same university in 1984. He became Professor of Geotechnical Engineering in 1996 and is presently working as an Emeritus Fellow in IIT Roorkee. His research interests are: Static & Dynamic Structure–Foundation Interaction, Rock Mechanics & Rock Engineering, Numerical Methods in Geo-mechanics and Computational Nonlinear Mechanics. He has so far guided 17 Ph.D. theses and about 73 Master's dissertations. He has to his credit about 120 research papers published in refereed national & international journals and conferences. He is also currently guiding three Ph.D. students and 2 Master's students. He has worked as a UNESCO in Italy, as a Visiting Professor in University of Wales, Swansea, UK and Technical University, Budapest, Hungary and also as a Visiting Scholar in the Department of Mechanical Engineering, The Hongkong University of Science & Technology, Hongkong. He has been a PI of research projects sponsored by DST, UGC, INCRMTT, and AICTE. Prof. Viladkar has rendered consultancy services for establishment of various cement and paper & Pulp industries, hydro-power projects, and for developmental and rehabilitation projects various hill states. He has also provided consultancy services to Oil refineries in UP, Gujarat & Tamilnadu and to some projects related to defense services. Prof. Viladkar has been a Member of the Research Council of Central Building Research Institute, Roorkee (2007-2010), and Member of Standing Advisory Committee of Central Soils & Materials Research Station, Ministry of Water Resources, New Delhi (2008–2011). He has been the Chairman of CED56 committee of BIS, and a Member of the Committee on Selection and Development of Sites for Buildings in Hilly. He is presently the Chairman of CED48 Committee on Rock Mechanics and is a member of the committee on Underground Openings and Field Monitoring. Prof. Viladkar is a Fellow of ISET, Life Member of IGS, INCRMTT, ISSMGE, & ISRM and Indian Society for Wind Engineering. He has received best research paper awards of IGS in 1979 & 1991, of ISET in 1985, and of ISRMTT in 1999, 2008, & 2011. Of the various Ph.D. theses he supervised in the area of Rock Mechanics, two Ph.D. theses were awarded with Prof. Leonard's Prize of IGS. In Recognition of his remarkable contributions to Rock Mechanics and Rock Engineering, ISRMTT, New Delhi also honored him with Outstanding Contribution to Rock Mechanics Award in the year 2013.